

Advancing the BRAMS wildfire–atmosphere modelling system: application to an extreme wildfire event

Isilda Cunha Menezes¹, Luiz Flávio Rodrigues², Karla M. Longo³, Mateus Ferreira e Freitas⁴, Saulo R. Freitas³, Rodrigo Braz², Valter Ferreira de Oliveira⁵, Sílvia Coelho¹, and Ana Isabel Miranda¹

¹Centre for Environmental and Marine Studies (CESAM) and Department of Environment and Planning, University of Aveiro, Campus Universitário de Santiago, Aveiro, Portugal

²Center for Weather Forecasting and Climate Studies (CPTEC), National Institute for Space Research, Cachoeira Paulista, SP, Brazil

³National Institute for Space Research (INPE), São José dos Campos, SP, Brazil

⁴Multiuser Laboratory of High Performance Computing (LaMCAD), UFG Innovation Agency, Federal University of Goiás (UFG), Samambaia Campus, Goiânia, GO, Brazil

⁵National Institute for Space Research (INPE), Cachoeira Paulista, SP, Brazil

Correspondence: Isilda Cunha Menezes (isildacm@ua.pt) and Saulo R. Freitas (saulo.freitas@inpe.br)

Received: 28 May 2025 – Discussion started: 10 July 2025

Revised: 24 February 2026 – Accepted: 25 March 2026 – Published:

Abstract. Wildfire smoke significantly perturbs atmospheric composition and radiative balance, with implications for air quality, weather, and climate. Accurately simulating smoke–radiation–convection interactions remains a scientific challenge, particularly at meso- to local scales. This study presents developments in the BRAMS v6.0 modelling system, including the integration of crown fire spread into SFIRE and dynamic coupling of fire-emitted smoke fluxes. These enhancements enable physically consistent simulations of wildfire behaviour, smoke emissions, and their radiative impacts.

Fire spread and heat release are used to compute Fire Radiative Power, which drives smoke emissions in real time. These emissions are fully integrated with aerosol–radiation interactions and atmospheric dynamics. The system was applied to the 15 October 2017 wildfire in central Portugal using high-resolution simulations.

Model performance was evaluated by comparing a diagnostic Smoke Optical Depth (SOD), computed offline from BRAMS-simulated PM_{2.5} using a Mie-based framework, with MERRA-2 Aerosol Optical Depth (AOD).

Statistical comparison shows that SOD and MERRA-2 AOD share a coherent spatiotemporal structure, with correspondence maximised during the active fire phase. Peak extinction reached $\sim 67 \text{ m}^{-1}$ at 400 nm and absorption ap-

proached $\sim 5 \text{ m}^{-1}$ at 550 nm in the near-source plume core, consistent with an OC-dominated scattering regime and localized BC-driven shortwave absorption. The resulting radiative heating contributed to the upward displacement of the CIN layer ($\approx 100\text{--}200 \text{ m}$) and to the partial erosion of low-level inversions, producing transient stability modifications.

Although the model occasionally produces very high near-source PM_{2.5} and optical-depth values confined to a small number of grid cells, additional diagnostics show that plume-integrated mass and optical properties remain physically consistent and are not dominated by boundary effects. These results demonstrate that the enhanced BRAMS system captures the coupled fire–atmosphere–radiation feedbacks of intense wildfires, improving the interpretation and prediction of smoke-induced thermodynamic and radiative perturbations.

1 Introduction

Understanding wildfire emissions is essential for accurately predicting air quality (Fernandes et al., 2022) and radiative impacts, particularly in complex terrains where local meteorological dynamics strongly influence smoke dispersion. Recent European case studies have shown severe urban air-

quality degradation during major wildfire episodes, including the August 2021 Athens fires (Osswald et al., 2023) and the October 2017 wildfires in north-central Portugal (Lopes et al., 2024). Wildfires release large quantities of trace gases and aerosols that interact with atmospheric chemistry (Andreae and Merlet, 2001; Jaffe et al., 2008; Monks et al., 2012), modulate radiative transfer (Clinton et al., 2006; Menezes et al., 2024), reduce visibility (Valente et al., 2007), and severely affect human health (Apte et al., 2018; Lopes et al., 2024; Miranda et al., 2010). These impacts further highlight the growing importance of high-resolution, community-based air-quality monitoring and citizen engagement initiatives (Relvas et al., 2025), which complement modelling and satellite approaches by improving local understanding and response capacity during wildfire events. These challenges are especially difficult to quantify under the rapidly changing conditions typical of wildfire episodes, requiring dynamic models capable of resolving fire–atmosphere feedback at high spatial and temporal resolutions.

Traditional approaches for estimating biomass-burning emissions in operational air-quality and climate models often rely on semi-empirical methods, including precompiled inventories such as the Global Fire Emissions Database (GFED) and satellite-derived Fire Radiative Power (FRP) products assimilated in systems like the Copernicus Atmosphere Monitoring Service, Global Fire Assimilation System (CAMS-GFAS) (CAMS, 2015). While these frameworks provide valuable large-scale emission estimates, their relatively coarse spatial resolution and simplified fire parameterizations limit their ability to capture the rapid evolution and spatial heterogeneity of active wildfires. This limitation is particularly critical in forested regions, where intense crown fires coexist with patchy surface burning and smouldering phases. As demonstrated by Oliveira et al. (2025), coarse FRP retrievals often miss or underestimate localized high-intensity combustion in complex terrain, introducing systematic biases in both the magnitude and timing of smoke emissions. While computationally efficient, these methods do not simulate fire spread or associated heat release, limiting their capacity to resolve the dynamic feedbacks that modulate local atmospheric stability and pollutant dispersion. The Brazilian Biomass Burning Emission Model (3BEM) (Freitas et al., 2009; Longo et al., 2010) coupled to BRAMS (Brazilian Regional Atmospheric Modeling System) follows this approach, estimating smoke emissions based on FRP, surface type, and meteorology, but without explicit coupling to fire dynamics. This framework is suitable for regional or long-term assessments but lacks physical consistency under rapidly evolving fire conditions.

Wildland fire behaviour models developed historically within the forestry community have been primarily designed to predict two-dimensional surface fire spread rates and heat release under prescribed fuel types, slope conditions, and wind fields, with a primary focus on fire danger assessment and surface fire behaviour. These operationally oriented

semi-empirical models are not intended to resolve highly dynamic or plume-driven fire behaviour, nor the onset of extreme fire development beyond the incipient stage.

Fully coupled atmosphere–surface fire models, such as AIRFIRE (Miranda, 2004), WRF-SFIRE (Mandel et al., 2011), CAWFE (Clark et al., 1996; Coen, 2005), or BRAMS-SFIRE (Menezes et al., 2021) and ForeFire/Meso-NH (Filippi et al., 2013), integrate a mesoscale non-hydrostatic, large-eddy numerical weather prediction core with a semi-empirical fire surface spread module (typically based on Rothermel, 1972 and McArthur, 1967). In such systems, the fire and atmosphere evolve as a single dynamically coupled entity, allowing simulation of small-scale fire–atmosphere interactions, vorticity-driven dynamics, fire-induced buoyancy, and turbulence feedback. These models explicitly represent fire-generated kinetic and potential energy via resolved sensible and latent heat fluxes, and predict fire perimeter evolution, fuel consumption, fireline intensities, and rate of spread. Model initialization requires fuel load and fuel moisture content, fuel burn rate, combustion heat release, and treatment of canopy ignition when heat flux exceeds a critical threshold, in addition to terrain and local wind forcing. In addition to the large variability in fire intensity and fuel structure, the chemical and physical characteristics of smoke particles evolve rapidly as they are transported away from the source, altering their optical behaviour and radiative impacts in ways that are not captured by simplified bulk-emission schemes.

Forest fires, during their propagation, consume the available biomass as characterized by the different NFFL fire behaviour fuel models (Anderson, 1982), which represent the landscape, and release high concentrations of particles and trace gases into the atmosphere. Primary aerosols are emitted throughout combustion, during both the flaming and smouldering phases, while secondary aerosols form in the atmosphere through chemical reactions involving precursor gases. However, primary particles can serve as condensation nuclei or “seeds” for secondary particle formation through aging processes, resulting in internally mixed aerosols with complex and evolving chemical compositions as they are transported within the smoke plume.

Primary particles include soot, predominantly composed of elemental carbon (BC), along with ash and mineral components derived from the burned biomass. These materials may exist as distinct particles or aggregate into larger mixed particles during combustion. Depending on their composition and surface properties, these aerosols can be hydrophilic (attracting water, enhancing growth in humid conditions) or hydrophobic (repelling water), affecting their interaction with radiation and their ability to act as cloud condensation nuclei (CCN).

As these particles are transported within the smoke plume, they undergo ageing processes that alter their physical and chemical properties. These include: (1) Coagulation – collisions and merging with other particles, leading to increased

size and complexity; (2) Surface reactions – interactions with atmospheric gases such as SO_2 , NO_x , and volatile organic compounds (VOCs), including terpenes and isoprenes (emitted by vegetation during natural biological processes) and aromatic compounds (from biomass combustion). These reactions lead to the formation of sulfates, nitrates, and organic coatings; (3) Oxidation, particularly of BC, resulting in the acquisition of oxygen-containing functional groups that modify its optical properties and enhance hydrophilicity.

In parallel, VOCs are oxidized in the atmosphere to produce oxygenated organic compounds, such as carboxylic acids (e.g., formic acid, acetic acid) and aldehydes (e.g., formaldehyde), which contribute to the formation and growth of secondary organic aerosols (SOA). These compounds can condense onto primary particles, forming coatings that significantly modify their optical and hygroscopic properties.

Moreover, photochemical reactions involving VOCs and oxidants such as ozone (O_3) and hydroxyl radicals (OH) also lead to secondary particle formation. Not all secondary aerosols are of local fire origin; VOCs and precursor gases transported from urban pollution sources or natural vegetation in other regions may also contribute further to increasing the complexity of the smoke plume and its optical properties.

Both primary and secondary aerosols interact with solar radiation through scattering and absorption of shortwave (visible and near-infrared) radiation, reducing direct sunlight at the surface while enhancing diffuse radiation (Yamasoe et al., 2006). These particles also absorb and re-emit long-wave (thermal infrared) radiation. While BC strongly contributes to absorption, sulfates and organic aerosols primarily enhance scattering, collectively influencing the atmospheric radiative energy balance (Yamasoe et al., 2006). The net result often includes local atmospheric heating, particularly in layers rich in BC.

These radiative interactions are governed by Mie theory, as most smoke particle sizes fall within the Mie regime (approximately 0.1 to 1 μm), where the particle diameter is comparable to the wavelength of incident radiation. Smaller particles ($\ll 0.1 \mu\text{m}$) scatter more efficiently at shorter wavelengths (e.g., blue light) and are better described by Rayleigh theory, which assumes particle sizes much smaller than the radiation wavelength. In contrast, larger particles exhibit non-selective scattering and remain within the Mie regime, with their radiative behaviour less dependent on wavelength.

As these primary and secondary aerosols interact with radiation through wavelength-dependent scattering and absorption, their evolving size distribution, mixing state and refractive index directly determine the radiative forcing exerted by the plume. This motivates the need for models capable of explicitly representing both fire behaviour and the microphysical processes that govern smoke optical properties.

Smoke aerosols strongly perturb the atmospheric energy balance through wavelength-dependent scattering and absorption, governed by their size distribution, complex refractive index, mixing state, and ageing (Pueschel et al., 1988;

Reid et al, 2005). These properties determine aerosol optical depth (AOD), single-scattering albedo, and vertical extinction structure, thereby influencing surface heating, atmospheric stability, and fire–atmosphere feedback. Curci et al. (2015) showed that neglecting aerosol mixing state can alter simulated AOD by more than a factor of two for identical aerosol mass, emphasising the need for physically based optical treatments in coupled fire–atmosphere systems. Regional studies have documented wide variability in smoke optical behaviour. Procopio et al. (2003) analysed AERONET observations over Brazil using Mie theory and validated a radiative forcing model across multiple optical thickness regimes and wavelengths. Reid and Hobbs (1998) found that Brazilian smoke exhibits about 15 % lower scattering coefficients and reduced single-scattering albedo relative to North American fires, attributed to combustion efficiency differences. Reid et al. (1999) further reported pronounced temporal variability in AOD over diurnal and multi-day cycles. Yumimoto et al. (2018) demonstrated that assimilating Himawari-8 aerosol observations improves the representation of Siberian smoke transport, correcting emission underestimations and capturing the distinctive C-shaped dispersion pattern over Japan. Finally, Ferrare et al. (1990), using NOAA-7 AVHRR data, characterized large-scale smoke transport from Canadian forest fires, with optical thickness ranging from < 0.1 to > 3.7 , particle radii of 0.3–0.9 μm , and lifetimes of 15–20 d, evidence of persistent, long-range smoke layers influencing regional radiative forcing. Makar et al. (2021) additionally demonstrated that wildfire smoke can cool the surface and stabilise the lower troposphere, altering plume dynamics and atmospheric circulation.

Recent advances in operational smoke forecasting systems, such as the HRRR-Smoke model (Ahmadov et al., 2017; Ye et al., 2021), have improved the coupling between fire activity, emissions, and atmospheric transport. Similar developments in regional and global frameworks (Anderson et al., 2024; Kochanski et al., 2021; Kochanski et al., 2015) have enhanced the representation of plume rise, aerosol–radiation interactions, and smoke dispersion. However, these systems generally rely on semi-empirical plume-injection schemes and parameterized fire emissions, without resolving crown fire propagation or the thermodynamic feedbacks associated with combustion heat release. Fully physically coupled fire–atmosphere models capable of simultaneously representing fuel consumption, surface- and canopy-fire spread, heat fluxes, and the resulting smoke optical effects remain rare in European wildfire contexts, particularly in complex mountainous terrain.

Addressing this gap, the present study employs a BRAMS–SFIRE configuration that explicitly resolves both surface and crown fire propagation and dynamically couples sensible and latent heat release to plume rise and vertical smoke transport. The main objective of this paper is to describe the improvements implemented in the BRAMS–SFIRE modelling system (Freitas et al., 2017; Menezes et

al., 2021; Menezes, 2015), aimed at enhancing the physical realism of wildfire representation beyond surface–fire-only approaches, through the inclusion of an explicit crown–fire propagation scheme. This explicit treatment is expected to produce a more physically consistent representation of smoke plume evolution, particularly under high-intensity fire conditions. By resolving fire–atmosphere interactions at fine spatial scales, the model improves the realism of smoke injection height, plume structure, and downwind dispersion, bringing them closer to observed plume behaviour. In addition, this system enables simulations that explicitly resolve both surface and canopy fire spread, fuel consumption, and the associated release of heat and smoke over heterogeneous terrain. Fire Radiative Power (FRP) is not prescribed but internally computed from model-resolved sensible heat fluxes, allowing smoke emissions to evolve dynamically with fire intensity and meteorological conditions. The two-way coupling further supports feedbacks between combustion processes and local thermodynamics, which are essential for accurately representing vertical smoke transport and smoke–radiation–convection interactions.

Section 2 describes the modelling developments and experimental design, including the treatment of crown fire initiation and vertical injection of emissions. Section 3 presents the simulated fire-spread behaviour, plume injection heights, PM_{2.5} loadings, and the resulting radiative and thermodynamic impacts, highlighting the value of fully two-way fire–atmosphere coupling for advancing understanding of wildfire-induced air-quality degradation and atmospheric feedback processes.

2 Methodology

This section details the advancements made in the BRAMS-SFIRE modelling system, including the integration of a crown fire spread behaviour model and the implementation of FRP calculations in SFIRE. The processes for assimilating National Fuel Fire Laboratory (NFFL) fuel behaviour models and high-resolution terrain elevation data are also described, ensuring accurate nesting of the SFIRE grid within the BRAMS grid for two-way coupling of wildfire fluxes and emissions. Furthermore, the methodology used to characterize particulate matter with an equivalent diameter less than 2.5 μm (PM_{2.5}) released during the Sertão wildfire episode on 15 October 2017, as simulated by BRAMS, is thoroughly explained. This includes the validation and interaction of smoke with atmospheric radiation, as well as the specification of surface conditions required by the SFIRE simulation. For a better understanding of the improvements that have been made, the section starts with a description of the original BRAMS-SFIRE modelling system.

2.1 The BRAMS-SFIRE modelling system

2.1.1 The BRAMS model

The BRAMS is based on the Regional Atmospheric Modeling System (RAMS) developed at Colorado State University (CSU/USA). It is free software (CC-GPL), maintained by the Centre for Weather Forecasting and Climate Studies from the National Institute for Space Research (CPTEC/INPE), the University of São Paulo (USP), and other institutions in Brazil and abroad. BRAMS and RAMS are versatile numerical weather prediction models, capable of simulating atmospheric circulations across a wide range of scales, from hemispheric to large eddy simulations (LES) of the planetary boundary layer. Significant improvements have been made to BRAMS to better represent key physical processes in tropical and subtropical regions, alongside integrated atmospheric chemistry and aerosol processes. It also includes a state-of-the-art model for simulating the exchange of water, energy, momentum, and biogeochemical tracers between the atmosphere and the surface (Freitas et al., 2017). BRAMS solves the compressible, non-hydrostatic atmospheric equations described by Tripoli and Cotton (1982). It uses a one-way nesting scheme to perform downscaling on computational grids with increasing spatial resolution (Freitas et al., 2017). Additionally, BRAMS incorporates a real-time assimilation method for the CCATT, focusing on the assimilation of trace gas and aerosol emissions from biomass burning, using FRP data derived from MODIS and GOES satellite products (Pereira et al., 2022; Pereira, 2013). Although the model typically underestimates emissions by up to 25 %, it successfully captures around 90 % of biomass burning activity, demonstrating high potential for near real-time monitoring of gases and aerosols emitted during biomass combustion. The FRP-based method improves emission estimations by 25 % compared to traditional methods, accurately capturing regional and local burning of biomass patterns (Pereira, 2013).

BRAMS has been extensively applied in South America; it remains a versatile model capable of simulating atmospheric processes across a wide range of latitudes, from tropical to mid-latitude conditions, in both hemispheres. To better evaluate its behaviour in complex topography and dynamically evolving mountain–valley breezes, estimated burned area values for the wildfire episode in Sertão, as simulated by BRAMS-SFIRE and WRF-SFIRE, were compared. The WRF-SFIRE and the BRAMS-SFIRE systems share a similar physical coupling architecture for simulating surface fire–atmosphere interactions.

2.1.2 The surface fire model (SFIRE)

A detailed description of the SFIRE surface fire module, including its ignition strategy, level-set front propagation, fuel-consumption algorithms, and coupling to atmospheric

forcing, was originally documented in Annex C of Menezes (Menezes, 2015). For completeness and clarity, we provide a concise summary of the key elements relevant to the present study below.

Ignition and initial conditions

SFIRE initializes combustion from a user-specified point or line ignition. To avoid singular behaviour at time $t = t_0$ and to seed a finite front, the code creates an initial burned kernel (small disc/segment) around the ignition locus. The advancing fireline is represented by a level-set function $\psi(x, t)$, with $\psi < 0$ inside the burning region, $\psi = 0$ at the fireline, and $\psi > 0$ outside.

Front kinematics via level sets

The fireline evolves according to a Hamilton–Jacobi equation:

$$\frac{\partial \psi}{\partial t} + R(x, t) \|\nabla \psi\| = 0 \quad (1)$$

where R is the local rate of spread (ROS, m s^{-1}) evaluated along the outward normal to the front. Time stepping uses a two-stage Heun (second-order Runge–Kutta) scheme. Spatial derivatives are computed with upwind-consistent reconstructions (standard upwind, Godunov, ENO, or Sethian formulations), which preserve the correct upwind direction and suppress spurious oscillations. Standard reinitialization keeps ψ close to a signed-distance function, stabilizing $\|\nabla \psi\|$. At the grid scale, a cell transitions to burning when ψ changes sign within the cell; hence, propagation between cells is governed by the zero-crossing of ψ , not by explicit geometric “jumps”.

Rate of spread and directional dependence

In the default configuration, the no-wind/no-slope ROS comes from the semi-empirical Rothermel (1972) formulation. Directional amplification by wind and slope is applied via multiplicative factors projected on the front normal. The model framework allows the user to select alternative spread formulations when appropriate for the dominant fuel type or regional fire regime. Available parameterizations include the McArthur (1966, 1967) law, commonly used for Australian forest fuels, and the Clark et al. (2004) spread formulation for chaparral and shrubland ecosystems. These options are user-defined in the configuration namelist.

Atmospheric forcing and topographic effects

The horizontal wind from the host atmosphere model is horizontally interpolated to the fire grid and vertically adjusted to mid-flame height using a logarithmic profile. Optionally, a mid-flame wind reduction factor (Baughman and Albini, 1980) is applied, conditioned on the fuel category, to represent drag within the fuelbed. Slope enters through the local

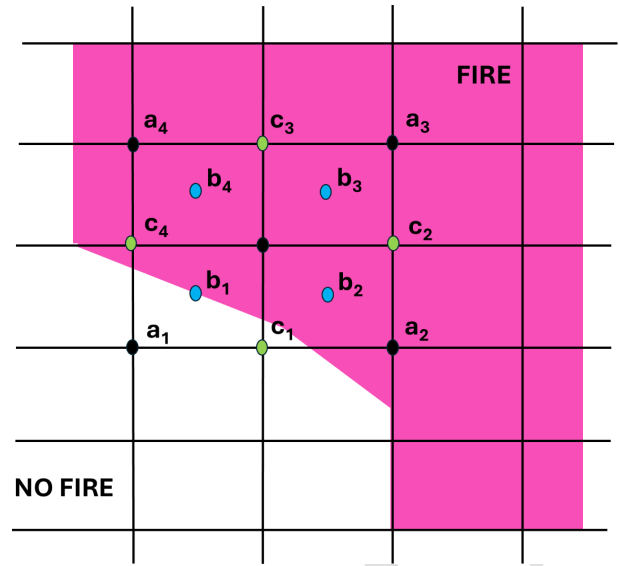


Figure 1. Schematic of fire-front propagation on the fire mesh. Black markers denote the high-resolution fire grid where the level-set function ψ and the burn time τ are advanced. Blue markers indicate bilinear interpolation of ψ and τ to the cell-center vertices using a four-point stencil. Green markers indicate bilinear interpolation of ψ and τ to the midpoints of each cell edge using a 1-D edge stencil. These interpolated values drive the fuel-consumption update (remaining-fuel calculation) at sub-cell locations. The magenta area marks cells classified as FIRE, while the white area corresponds to NO FIRE.

terrain gradient projected onto the propagation direction, providing the Rothermel (1972) slope factor.

Fuel consumption and heat release

Each fire-grid cell carries a non-dimensional available-fuel fraction $F \in [0, 1]$ that decays after ignition according to the cell’s flame residence time and fuel moisture. Two consistent algorithms compute within-cell fuel loss using bilinear interpolation of ψ and ignition time at cell vertices/edges: (i) a fast algebraic approximation and (ii) a more accurate quadrature/least-squares method for partially burning cells (Fig. 1). Sensible and latent heat fluxes (W m^{-2}) are then diagnosed from the burning rate and fuel properties and coupled back to the atmosphere.

Fuel-moisture diagnosis

Fuel moisture responds to ambient humidity, temperature, and precipitation using established wetting/drying laws (after Van Wagner and successors), with appropriate lags for different timelag classes. Atmospheric scalars are interpolated from the host grid to the fire grid with distance-weighted schemes; precipitation and relative humidity modulate both consumption and diagnosed heat fluxes.

Fire-grid stability and definition of overpropagation

Let Δx be the fire-grid spacing and Δt the integration step used for the level-set update. The distance a front element advances in one step is $d \approx R\Delta t$. If d becomes comparable to or exceeds Δx anywhere on the mesh, the front can traverse multiple cells in a single update, producing a numerically accelerated spread that is not physically warranted by the resolved fields. We refer to this violation of the fire-CFL condition: $R\Delta t \lesssim c\Delta x$ ($0 < c \leq 1$) as overpropagation. The risk increases (i) when a coarse Δx is advanced with too large a Δt (e.g., if fire is stepped only at the atmospheric time step), and (ii) locally where R spikes due to strong winds are projected at mid-flame height or steep terrain slopes (especially if wind reduction or terrain resolution are not consistent with the fire grid).

Numerical and physical controls to avoid overpropagation

SFIRE employs several safeguards:

- *Temporal subcycling of the fire solver.* Within each atmospheric step, the level-set is advanced with one or more fire substeps Δt_{fire} chosen to satisfy $R\Delta t_{\text{fire}} \leq c\Delta x$ across the grid.
- *Physically plausible ROS caps.* Upper bounds on R per fuel type and environmental state prevent unrealistically large local advances (e.g., under transient gusts or extreme slopes).
- *Level-set reinitialization.* Periodic signed-distance reinitialization stabilizes $\|\nabla\psi\|$ and the speed function.
- *Consistent forcing.* Application of mid-flame wind reduction factors and the use of terrain data at a resolution commensurate with the fire grid mitigate artificial inflation of the wind and slope multipliers.
- *Realistic ignition seeding.* A finite initial burned kernel aligned with observed perimeters avoids spuriously rapid early-time expansion from a point-like ignition on coarse meshes.

Together, these measures keep front advancement physically consistent across grid sizes and explain why resolution-aware tuning (choice of subcycling, ROS caps, and forcing options) is necessary and justified.

2.1.3 BRAMS-SFIRE interface integration

BRAMS was coupled with the SFIRE model to simulate atmosphere and fire interactions (Menezes et al., 2021). The communication between the BRAMS model and the SFIRE model is facilitated through an interface program. In this process, variables from BRAMS related to the basic state of the atmosphere are assimilated through this interface with

SFIRE. These variables include surface pressure, air moisture at 2 m, air temperature at 2 m, zonal and meridional wind components at the lowest vertical model levels, geopotential height, air density, microphysics, vegetation cover (including roughness and vegetation type), and heat fluxes.

When SFIRE is called at the first time step, the driver initializes the SFIRE model by reading SFIRE's parameters from a namelist, configuring flags, and setting the grid spacing. The high-resolution SFIRE domain is then integrated into the BRAMS model domain by creating a grid centred on the ignition points, with a radius that encompasses the area predicted to be burned by the fire. Detailed input on fuel behaviour models and terrain height at high resolution must be provided, which are then read and interpolated onto the SFIRE grid domain. After the ignition time, SFIRE injects sensible and latent heat fluxes, along with FRP, into BRAMS, explicitly forcing the atmospheric energy and thermodynamic fields and driving the production and transport of smoke-related aerosol mass. These heat fluxes are directly coupled to the BRAMS turbulence and boundary-layer parameterizations, ensuring dynamic consistency in the representation of fire-induced buoyancy and energy transfer within the atmospheric column.

The BRAMS model offers two approaches for simulating smoke emissions: (1) the dispersion of smoke particulate matter derived from FRP, simulated by SFIRE and used as a passive tracer for atmospheric transport; and (2) a chemistry-coupled approach that integrates smoke particulate matter from SFIRE with emissions from the Biomass Burning Emission Model (3BEM), anthropogenic and biogenic inventories, and analysis data from the Copernicus Atmosphere Monitoring Service (CAMS). This latter approach is implemented through the CCATT module of BRAMS, enabling more comprehensive simulations of atmospheric composition, pollutant transport, and concentration patterns. These dual methodologies enhance the model's capability to accurately represent the complex interactions between fire emissions and atmospheric chemistry.

2.1.4 Plume-rise and vertical injection of fire emissions in BRAMS

In BRAMS, fire-emitted aerosols and gases are not injected solely at the surface. Instead, the model employs an online, physically based plume-rise scheme implemented within the CCATT-BRAMS chemistry and aerosol module (Freitas et al., 2006, 2007, 2010). At each timestep, the sensible heat flux released by the fire provides the buoyant energy that drives vertical transport of the plume, which determines the plume-top height dynamically by applying a 1-D time-dependent cloud model. The diagnosed injection height is then projected onto the model's σ -coordinate system, and the emitted mass is vertically distributed across multiple layers, rather than being confined to a single surface level.

Accordingly, BRAMS follows a surface emission plus dynamic plume-rise approach, in which the vertical distribution of smoke is determined interactively at runtime by the evolving fire heat release (Q), atmospheric stability, and convective turbulence, rather than by any fixed or user-defined injection layer. This ensures that the injection height and profile evolve consistently with the meteorological state and the fire intensity.

The BRAMS-SFIRE modelling system was evaluated through its application to the extreme Sertão wildfire that occurred on 15 October 2017 in central Portugal (Menezes et al., 2024). This event unfolded over complex mountainous terrain dominated by strong valley-mountain circulations, providing a demanding testbed for assessing plume-dynamics realism. Figure 2 shows the simulated smoke column for this case, with PM_{2.5} lofted several hundred metres above the surface. This vertical structure arises directly from the SFIRE-resolved heat fluxes and the associated FRP-derived emissions. The plume-rise diagnosis, after which the smoke is advected, mixed and transformed by the model's dynamical, turbulent and chemistry–aerosol processes is described in the following sections.

2.1.5 New improvements on BRAMS-SFIRE

Several enhancements were made to this coupled BRAMS-SFIRE system. Figure 3 schematically shows these improvements.

Further details on the improvements and the new subroutines integrated in the modelling system are provided in the following sections.

Implementation of the Crown Fire Behaviour Model

The SFIRE model (Mandel et al., 2011; Mandel et al., 2009), coupled with BRAMS (Freitas et al., 2017) by Menezes et al. (2021) and Menezes (2015), enables the analysis of surface fire behaviour, accounting for fuel bed type along with its thermal, mineral, and dendrometric characteristics, moisture content, topography, and atmospheric wind conditions. Significant improvements were made to this coupled model based on the work of Scott and Reinhardt (2001) by integrating a numerical model that predicts the spread and intensity of crown fires. This enhancement was incorporated into the SFIRE surface fire spread subroutines, as is illustrated in the scheme shown in Fig. 3. The new subroutines were developed to improve the prediction of fire spread and intensity in tree canopies and to perform the interpolation of NFFL fuel behaviour models and terrain elevation onto the SFIRE grid.

In the “set_fire_crown_params” subroutine, the quasi-steady rate of spread is calculated for fuel behaviour model 10, which is a standardized vegetation fuel description. This model defines the physical and chemical properties of the fuel that are essential for computing fire spread rate, intensity, and overall fire behaviour. In the “consume_crown” sub-

routine, the rate of active crown fire spread and the fraction of the canopy fuels consumed are computed. To determine these parameters, the subroutine calculates the equivalent rate of spread $R_{\text{initialization}}$ (Eq. 2, concepts in Forestry Canada Fire Danger Group, 1992 and Van Wagner, 1977), which depends on the critical (minimum) fireline intensity $I_{\text{initialization}}$ of the surface fire, and the heat yield of fuel release per unit area H . It is important to note that SFIRE is implemented using the International System of Units (SI).

$$R_{\text{initialization}} = \frac{60I_{\text{initialization}}}{H} \quad (2)$$

Where 60 is a conversion factor so that the units for I reduce from $\text{kJ m}^{-1} \text{min}^{-1}$ to kW m^{-1} , and H Andrews and Rothermel, 1982):

$$H = I_{r10} t_r \text{ (in } \text{kJ m}^{-2} \text{)} \quad (3)$$

The symbol I_{r10} represents the reaction intensity for NFFL fuel behaviour model 10, while t_r (Eq. 4) represents the residence time for the same model (in minutes). The latter variable is a function of the surface-area-to-volume ratio (σ_{10}), as described below,

$$t_r = \frac{12.595}{\sigma_{10}} \quad (4)$$

The rate of active crown fire spread R_{active} (Eq. 5), set to 40 % of the observed 6.1 m windspeed at midflame height (Rothermel, 1991), i.e., the average height within the flaming combustion zone where wind directly influences fire behaviour. This height is commonly used in fire behaviour modelling for standardization, particularly in the context of surface and crown fire interactions. Active crown fire spread varies with wind speed, but is also influenced by slope and foliar moisture content (FMC, measured in percent), through the foliar moisture effect (FME) as defined by Van Wagner (Van Wagner, 1974, 1977, 1989),

$$R_{\text{active}} = 3.34 \left(\frac{\text{FME}}{\text{FME}_0} \right) (R_{10})_{40\%} \text{ (in } \text{m s}^{-1} \text{)} \quad (5)$$

with,

$$\text{FME} = \frac{(1.5 - 0.00275\text{FMC})^4}{460 + 25.9\text{FMC}} \quad (6)$$

considering the ratio of FME to a reference value $\text{FME}_0 = 0.0007383$, established for a foliar moisture content (FMC) of 100 % (Scott and Reinhardt, 2001).

Building upon the transition function concept proposed by Van Wagner (1989) that provides a scaling mechanism between surface and crown fire spread predictions, the model accounts for this process using Eq. (7).

$$R_{\text{surface}} \geq R_{\text{initialization}} + 32.8084 \text{ (in } \text{m s}^{-1} \text{)} \quad (7)$$

2017-10-15 15:00 UTC

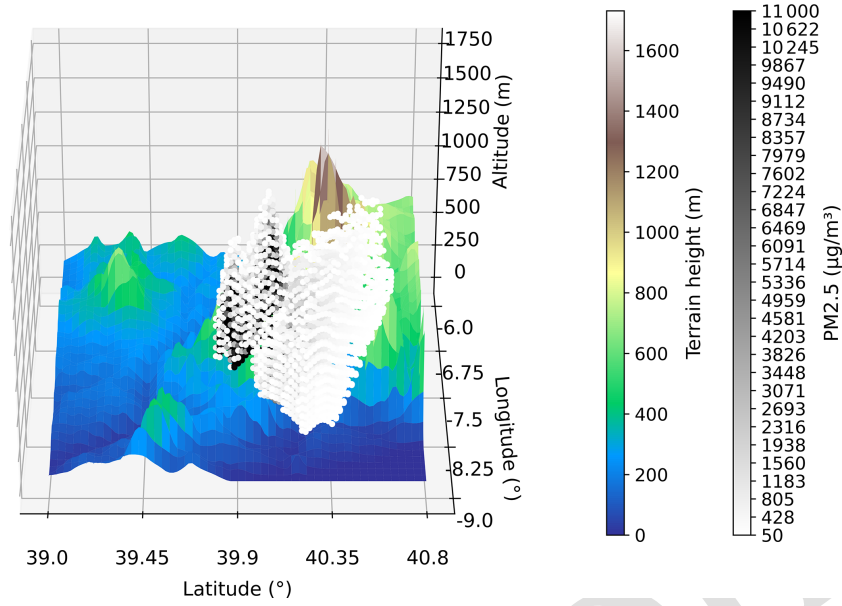


Figure 2. 3-D view of BRAMS–SFIRE smoke injection on 15 October 2017 (15:00 UTC); plume-top height and vertical allocation are computed online from SFIRE heat release/FRP using the CCATT-BRAMS plume-rise scheme.

CFB (Eq. 8) is a transition function known as the crown fraction burned, representing the fraction of available canopy fuels consumed during a fire. It is used to estimate the degree of crowning (Van Wagner, 1989) and to predict the resulting spread rate in fire behaviour simulations. CFB values range from 0 for a surface fire to 1 for a fully active crown fire.

$$\text{CFB} = 1 - e^{-0.23(R_{\text{surface}} - R_{\text{initialization}})} \quad (8)$$

The “fire_ros” subroutine applies criteria to determine the initiation and sustained spread of crown fires, classifying a fire as either surface fire or crown fire, without differentiating between passive and active crown fire. The approach is based on a threshold criterion (Eq. 9) involving the fireline intensity required to sustain crown fire behaviour (Classification based on Van Wagner, 1977 and Alexander, 1988, as described in Fig. 6 of Scott and Reinhardt, 2001),

$$I_{\text{surface}} > I_{\text{initialization}} \quad (9)$$

with I_{surface} representing the Byram fireline intensity, which is the rate of heat release per unit length of fire front (kW m^{-1}), and $I_{\text{initialization}}$ (Van Wagner, 1977) calculated within the fire_supplementary_intensity subroutine, as defined in Eq. (10).

$$I_{\text{initialization}} = \frac{\text{CBH}(460 + 25.9\text{FMC})^{3/2}}{100} \quad (\text{in } \text{W m}^{-1}) \quad (10)$$

where CBH represents the canopy base height. R_{10} refers to the surface fire spread rate for fuel behaviour model 10

(Mandel et al., 2011; Rothermel, 1972), with its components calculated within the “fire_ros_cawfe_crown” subroutine, as defined in Eq. (11).

$$R_{10} = R_{\text{back}_{10}} + R_{\text{wind}_{10}} + R_{\text{slope}_{10}} \quad (\text{in } \text{m s}^{-1}) \quad (11)$$

By substituting Eq. (11) into Eq. (5) from the “consume_crown” subroutine and incorporating Eq. (8) for crown fraction burned (CFB) from the same subroutine, Eq. (12) can be derived to calculate the total fire spread following Van Wagner (1989, 1993) and the Forestry Canada Fire Danger Group (1992), considering Eq. (9).

$$R_{\text{final}} = \begin{cases} R_{\text{surface}} + \text{CFB}(R_{\text{active}} - R_{\text{surface}}) & \text{with crown spread} \\ R_{\text{surface}} & \text{otherwise} \end{cases} \quad (\text{in } \text{m s}^{-1}) \quad (12)$$

The fire_total_intensity subroutine calculates the fire energy flux (ϕ) (W m^{-2} , Mandel et al., 2011) originating from the combustion of dried fuel, as defined in Eq. (13),

$$\phi = \frac{W_{\text{surface}}}{dt} R_{\text{final}} \left(1 - \frac{\text{FMC}}{1 - \text{FMC}} \right) H_{\text{Low}} \quad (13)$$

where W_{surface} represents the initial total mass of surface fuel (kg m^{-2}), and H_{Low} denotes the lower heat content of the fuel. This calculation, defined in Eq. (14), is performed to predict the fire intensity, I_{final} (Scott and Reinhardt, 2001), accounting for the integration between the shrub/herbaceous layer and the tree canopy.

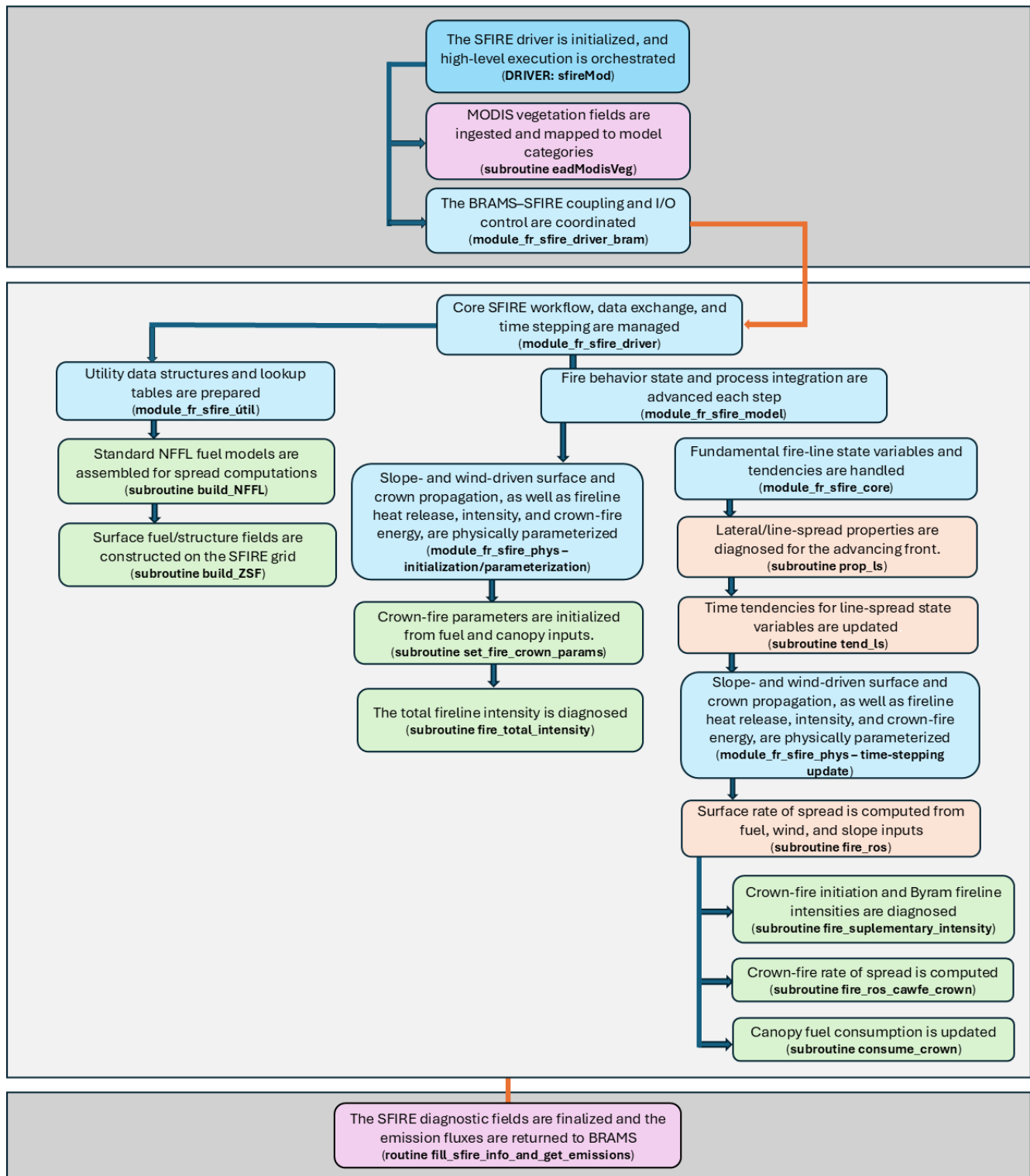


Figure 3. Diagram illustrating the structure of the SFIRE model, with newly integrated subroutines denoted in light green boxes and called within the subroutines highlighted in light orange. The light blue boxes indicate the modules where these subroutines are implemented. The light pink boxes represent the subroutines responsible for integrating the BRAMS and SFIRE models in the context of wildfire emissions.

$$I_{\text{final}} = \frac{(H + \phi \cdot \text{CFB}) R_{\text{final}}}{60} \text{ (in W m}^{-1}\text{)} \quad (14)$$

Implementation of FRP in SFIRE

The following equations, implemented in module_fr_fire_model, are used to estimate the radiative power emitted from a burning area A , based on the Stefan-Boltzmann law and the sensible-heat (calorimetry) relation. The radiative power P (Eq. 15) is proportional to the emissivity ϵ , the Stefan-Boltzmann constant σ , the burnt area A , and the fourth power of the temperature T (K).

Alternatively, the equation can also be expressed in terms of the sensible heat flux Q_s (W m^{-2}), the mass of the burned material m , and the specific heat capacity c of dry wood, as shown in Eq. (16).

$$P = 10^{-6} (\epsilon \cdot \sigma \cdot A \cdot T^4) \text{ (in MW)} \quad (15)$$

$$P = 10^{-6} \left(\epsilon \cdot \sigma \cdot A \cdot \left(\frac{Q_s}{m \cdot c} \right)^4 \right) \text{ (in MW)} \quad (16)$$

The parameters used in this study are as follows: an emissivity value of 0.85 (Àgueda et al., 2010; Riggan et al., 2004), a specific heat capacity for dry wood estimated as $c = 1500 \text{ J (kg K)}^{-1}$ (Radmanović et al., 2014), and the Stefan-Boltzmann constant as $\sigma = 5.67 \times 10^{-8} \text{ W (m}^2 \text{K}^4\text{)}^{-1}$.

Fuel Models and Terrain Data Assimilation Subroutine Implementation

The build_NFFL and build_ZSF subroutines are responsible, respectively, for the integration of NFFL fuel behaviour models and high-resolution terrain elevation data into the SFIRE computational domain. This process is carried out following the procedure detailed below:

- *Data Input and Configuration*: The subroutines read user-provided input files, generated in accordance with the methodology described by Menezes et al. (2021) and Menezes (2015). One file contains categorical information on NFFL fuel models, while the other provides terrain elevation data. During this step, key parameters such as grid resolution, initial coordinates, geospatial constants, and the dimensions of both datasets are defined.
- *Coordinate Calculation*: Geodetic coordinates (latitude and longitude) corresponding to the input data grids are calculated based on the predefined cell size.
- *Data Interpolation*: The input fuel and terrain data are interpolated onto the SFIRE grid by identifying the nearest neighbouring grid nodes. This interpolation employs the Haversine formula to calculate geodesic distances, ensuring that the curvature of the Earth is properly accounted for in the spatial mapping.

- *Result Storage*: The resulting interpolated datasets are saved in binary format for efficient access and subsequent use during the simulation workflow.

Coupling SFIRE Outputs with the BRAMS Framework for Wildfire Emissions Simulation

The fill_sfire_info_and_get_emissions subroutine integrates the FRP generated by the SFIRE domain simulation into the coarse-resolution grid of the BRAMS model, enabling the calculation of wildfire emissions. It performs the following key tasks:

- *Aggregated radiative power*: The FRP, calculated from the SFIRE grid-cell sensible heat flux, is spatially aggregated (summed) into the corresponding BRAMS atmospheric grid cells.
- *Stores fire data*: For each valid fire point, the corresponding information is stored in an array, indexed by geographic coordinates.
- Calls the subroutine “get_emission_in_global_brams_grid”, which:
 - BRAMS grid cells exhibiting positive FRP, burned area, and finite burn duration are identified and classified as active fire points.
 - Associates each fire point with a vegetation type based on MODIS land cover data within the BRAMS grid.
 - Calculates burned biomass and emissions of various particulate matter species (e.g., PM_{10} , $\text{PM}_{2.5}$), using emission factors and the flaming fraction, which distinguishes between flaming and smoldering phases.
- *Performs statistical calculations*: Computes emission statistics, such as the mean and standard deviation of FRP and burned area for each BRAMS grid cell.

This workflow ensures a seamless integration between fire dynamics modelled by SFIRE and the atmospheric process represented in BRAMS, enabling accurate simulation of wildfire emissions and their atmospheric impacts. In this study, only BRAMS passive tracer dispersion capabilities are used, focusing on the transport and dispersion of tracers without engaging the full atmospheric chemistry module. This approach allows for detailed analysis of pollutant transport patterns while minimizing computational costs.

Fire Mesh Refinement and Coupling Strategy within the SFIRE–BRAMS Framework

In SFIRE–BRAMS, the fire module does not operate on an independent or arbitrary domain but rather on a refined computational mesh dynamically generated around the ignition

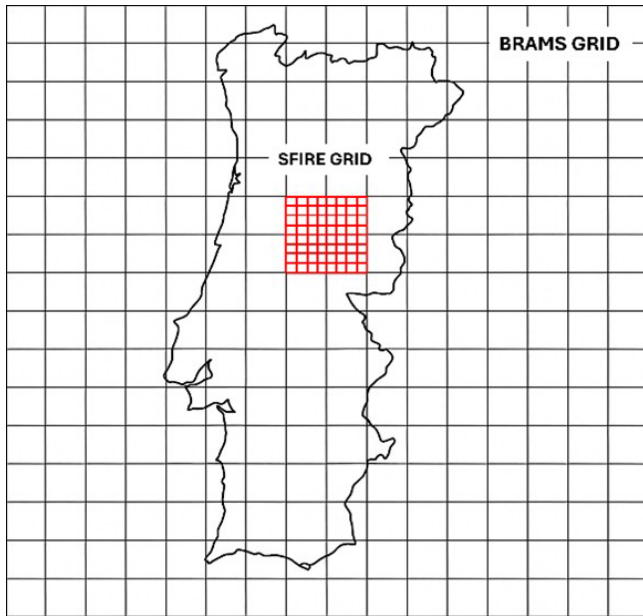


Figure 4. Schematic representation of the SFIRE–BRAMS grid nesting approach. Only for illustration, a regular 14×14 coarse-resolution BRAMS grid is superimposed on the outline of mainland Portugal, showing the atmospheric model domain onto which the finer-resolution SFIRE fire grid can be dynamically embedded.

point(s) specified by the user (Fig. 4). The horizontal extent of this refined mesh is defined in degrees of latitude and longitude and determines the size of the nested fire grid within the parent BRAMS domain. The atmospheric grid resolution (typically 2–1 km down to 200 m) and an integer refinement factor (even-valued) jointly control the local fire-grid spacing, which usually ranges from 200 to 10 m depending on the user-specified refinement factor.

Within this refined sub-domain, SFIRE resolves ignition, flame propagation, and perimeter evolution using the level-set method coupled with the Rothermel (1972) spread-rate formulation. The refinement must, however, remain physically consistent with the expected fire behaviour: excessively coarse fire meshes tend to smooth the flaming front and underestimate fire radiative power (FRP) and burned area, whereas overly fine meshes may become computationally prohibitive without a commensurate gain in accuracy.

Thus, the FRP/active-area/perimeter dynamics are not “scaled” but explicitly resolved at the SFIRE resolution inside the BRAMS parent cell. In this study, we selected the refinement factor by balancing physical realism with the maximum computational user capacity allowed on the available HPC infrastructure (memory per node and MPI task limits), ensuring that SFIRE could explicitly resolve fire-front geometry while maintaining BRAMS time-step stability and tractable wall-clock cost.

The simulation domains used in this study are shown in Fig. 5. The coarser domain, corresponding to the BRAMS

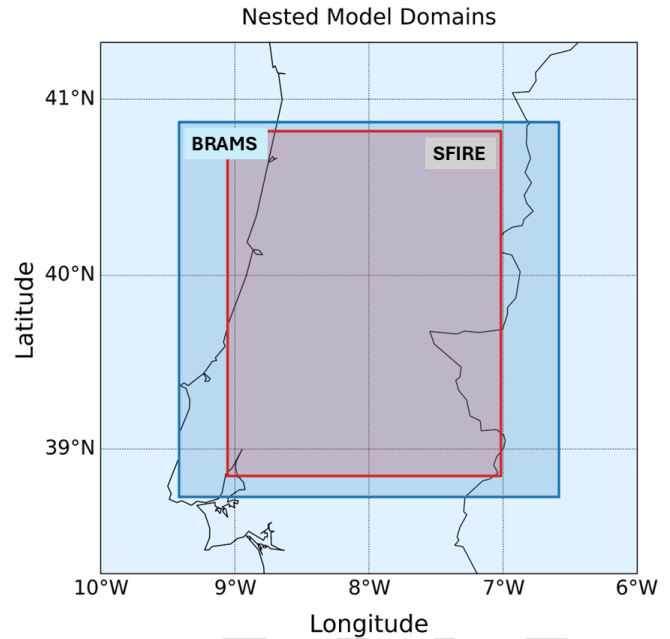


Figure 5. Nested simulation domains over central–northern Portugal. The dark-blue region represents the coarse BRAMS domain (2 km resolution), while the red–cyan region corresponds to the inner high-resolution SFIRE domain (200 m resolution).

grid, was configured with a 2 km resolution, while the inner SFIRE domain was nested at a finer resolution of 200 m.

Representation of Aerosol–Radiation Interactions in BRAMS for Iberian Applications

Having established the mesh-refinement configuration and the two-way fire–atmosphere coupling, the representation of aerosol–radiation interactions in BRAMS, which shapes wildfire-driven thermodynamic responses over the Iberian Peninsula, is described. The incorporation of regionally tuned Aerosol Spectral Optical Properties (ASOP) models into the BRAMS radiative framework is first outlined, followed by the diagnostic derivation of spectrally resolved smoke optical properties from BRAMS–SFIRE prognostic $PM_{2.5}$ fields. This enables a physically consistent evaluation of wildfire smoke optical behaviour and its radiative feedbacks on the lower troposphere.

Improvement of Regional Aerosol Spectral Optical Properties into BRAMS

Given the limited spatial-temporal coverage of satellite aerosol products (e.g., MODIS, VIIRS) and reanalysis datasets such as MERRA-2, particularly under cloudy or nighttime conditions, physically based models such as BRAMS offer both a complementary and, when required, a fully self-contained alternative. BRAMS can ingest satellite information for constraint and evolution, but it also runs in a

physically based, coupled fire–atmosphere mode that explicitly simulates fire spread from fuel properties and meteorological conditions, prognoses fire radiative power (FRP), and resolves smoke concentration fields alongside meteorological and thermodynamic variables.

Because the realism of these simulations depends critically on how the model represents aerosol optical behaviour, regional parametrisations tailored to Iberian aerosol regimes have become increasingly necessary. In this context, do Rosário et al. (2026) developed seasonal Aerosol Spectral Optical Properties (ASOP) models for Iberian aerosol mixtures to improve the representation of radiative and aerosol processes in BRAMS. These ASOP models were subsequently incorporated into BRAMS to enhance the optical characterisation of particulate matter emitted in wildfire simulations performed with the coupled BRAMS–SFIRE system. Based on a long-term (2003–2023) characterization of aerosol microphysical properties, optical parameters, such as spectral AOD, Angstrom Exponent (AE), SSA asymmetry parameter, and refractive indices, were derived using Mie theory applied to AERONET sun photometer data. The ASOP models represent typical regional aerosol scenarios, including smoke, dust, and background aerosol mixtures. Spatial representativeness was evaluated through monthly correlations between MERRA-2 and AERONET data, including AOD and SSA, enabling the identification of areas predominantly influenced by each model. This approach enhances aerosol–radiative transfer simulations in BRAMS over the Iberian Peninsula, improving predictions of thermodynamic profiles and surface temperatures, while reducing uncertainties in the representation of aerosol optical properties.

Diagnostic Derivation of Smoke Optical Properties from BRAMS–SFIRE Aerosol Field Output

Although BRAMS outputs do not directly provide aerosol optical properties, in this work they are diagnostically derived from the prognosed aerosol mass and thermodynamic fields (e.g., temperature and relative humidity). Using Mie theory and radiative-transfer formulations, spectrally and vertically resolved extinction, scattering, and absorption coefficients are obtained, from which integrated optical metrics such as aerosol optical depth (AOD), single-scattering albedo (SSA), and the asymmetry factor are computed. This physically consistent offline radiative post-processing enables the assessment of wildfire smoke induced modifications to radiative fluxes and lower-tropospheric thermodynamics (e.g., heating/cooling rates, static stability, boundary-layer evolution), while also facilitating robust comparison with satellite-retrieved AOD.

2.2 Data requirements

2.2.1 Surface data used as input in SFIRE

To simulate the spread of surface and crown fires using SFIRE, high-resolution Northern Forest Fire Laboratory (NFFL) fire behaviour fuel models and terrain elevation data on a regular grid are required. The NFFL fuel behaviour models are a set of 13 canonical fuel categories developed by the US Forest Service’s Northern Forest Fire Laboratory (Albini, 1976; Anderson, 1982) to parameterize surface fuel characteristics for operational fire spread modelling (Rothermel, 1972). Each model specifies representative fuel properties, such as fuel load partitioned by size class, surface-area-to-volume ratio, fuelbed depth, heat content, moisture-of-extinction, and live/dead fractions, that together determine the rate of spread, fireline intensity, and flame length under given wind and slope. The NFFL fuel behaviour models provide a standardised mapping between vegetation/fuel types and the inputs required by semi-empirical fire-spread equations; they are widely used for case studies, fire danger rating, and coupled fire–atmosphere applications. While subsequent schemes expanded and refined these categories (e.g. the 40 “standard” fuel models of Scott and Burgan, 2004), the original 13 NFFL models remain a common reference and are frequently denoted as NFFL 1–13. Among them, NFFL 10 (timber litter and understory) is particularly relevant because it represents dense surface fuels that readily support high-intensity surface fire, making it one of the canonical fuel types used to evaluate the potential for surface-to-crown fire transition.

In this study, NFFL fuel behaviour model data were derived from the Portuguese National Forest Inventory 6 (Menezes et al., 2021). Additional inputs are also needed for the “namelist.fire” file, including physical, thermal, chemical, and mineral specifications of surface vegetation (Menezes et al., 2021; Menezes, 2015), as well as of tree canopy fuel within the simulation domain (such as canopy base height (CBH) and crown foliar moisture content (FMC)) for the 13 NFFL fuel behaviour models.

CBH and FMC values were assigned using GIS methods by intersecting primary and secondary land data with five dominant forestry species (Table 1) and cross-referenced with the 13 NFFL fuel models. These data were part of 7964 field plots of the 2006 National Forest Inventory, provided by the Portuguese Institute for Nature Conservation and Forests (ICNF, 2015), and adopted from the work of Menezes (Menezes, 2015) based on measurements conducted in October 2010 in the Évora district, part of the Alentejo region in southern Portugal, characterized by agro-silvopastoral landscapes known as Montado.

Although FMC values from international literature were considered, they were ultimately excluded from this study, because they may not accurately represent the climatic, edaphic, and physiological conditions of Portuguese ecosys-

Table 1. Average crown foliar moisture content (in %) for the 13 NFFL fuel behaviour models based on field data from five dominant forestry species (Alentejo, Portugal; October 2010) (Menezes, 2015).

Tree species	FMC
<i>Pinus pinaster</i> Aiton	126.89
<i>Pinus pinea</i> L.	129.62
<i>Eucalipto globulus</i> Labill	118.51
<i>Quercus rotundifolia</i>	63.37
<i>Quercus suber</i> L.	72.32

Table 2. Average canopy base height (in meters) for the 13 NFFL fuel behaviour models based on field data from five dominant forestry species (Alentejo, Portugal; October 2010) (Menezes, 2015).

Fuel Models	CBH
NFFL 1	6.43
NFFL 2	8.28
NFFL 3	8.11
NFFL 4	8.02
NFFL 5	10.04
NFFL 6	8.94
NFFL 7	9.67
NFFL 8	7.36
NFFL 9	7.32
NFFL 10	7.60
NFFL 11	7.02
NFFL 12	3.02
NFFL 13	0.62

tems. The FMC values presented in Table 1 were therefore used to do this classification.

Following the same methodology, CBH was determined. CBH is influenced by factors such as forest management practices, stand density, tree age, and species composition. In Portugal, CBH values can vary significantly. The specific average ranges, calculated using only the same five tree species, for each of the 13 NFFL fuel models, are detailed in Table 2.

2.2.2 Surface and meteorological data used as input in BRAMS

Having detailed the surface datasets used to characterise the SFIRE grid, namely the high-resolution terrain, the land-cover classification, and the associated fuel models and their physical properties that govern fire spread and heat release, the description now turns to the surface and meteorological fields that provide the initial and boundary conditions for the BRAMS grid, thereby ensuring dynamical consistency between the fire module and the atmospheric environment in which it evolves.

To establish the initial atmospheric state, BRAMS incorporated several datasets, including land cover type, soil type, the Normalized Difference Vegetation Index (NDVI), weekly sea surface temperatures, daily soil moisture, and soil temperature. The NDVI was derived from 15-day MODIS composite images spanning 2001 to 2002 (Moreira et al., 2013), while weekly sea surface temperature data were obtained from datasets distributed by Reynolds et al. (2002). Daily soil moisture, an operational product of CPTEC/INPE based on rainfall estimated from TRMM (Gevaerd and Freitas, 2006), was also integrated. The initialization of soil temperature was based on air temperature values from the first level of the BRAMS atmospheric model.

Terrain elevation data with a spatial resolution of 30 arcsec (approximately 1 km) in latitude and longitude were sourced from the United States Geological Survey's Earth Resources Observation Systems data centre (Gesch et al., 1999) and assimilated during the model initialization.

The atmospheric fields, including zonal and meridional wind, air temperature, geopotential height, and relative humidity, used for both the initialization and boundary conditions, were obtained from the ECMWF Reanalysis v5 (ERA5, 2019). These data were available at 37 vertical pressure levels and 6 h intervals on a regular grid and were interpolated to the BRAMS grid to ensure consistency between the initial and boundary conditions.

2.2.3 Data used for model validation

Having outlined the initial and boundary conditions for the BRAMS grid, the following paragraphs describe the reanalysis datasets used for model validation, which provide an external benchmark for assessing the realism of the simulated fine particulate matter (PM_{2.5}) generated by fire smoke–atmosphere interactions.

Aerosol concentration, extinction coefficients, and AOD values were retrieved from the Modern-Era Retrospective analysis for Research and Applications, version 2 (MERRA-2, 2015) dataset. This dataset assimilates observations from a variety of instruments, including satellite-based radiometers, to provide global, long-term atmospheric reanalysis data.

MERRA-2 offers a spatial resolution of $0.5^\circ \times 0.625^\circ$ and includes 72 hybrid-eta vertical levels extending from the surface to 0.01 hPa (Gelaro et al., 2017). Its temporal resolution is 3 h, consistent across the various atmospheric and aerosol variables. The MERRA-2 collections used in this study were obtained from the Global Modeling and Assimilation Office (GMAO) (MERRA-2, 2015).

MERRA-2 uses the GEOS-5 model (~ 50 km horizontal resolution, 72 vertical levels) coupled to the GOCART aerosol module and a 3-hourly aerosol analysis system (GAAS). Column AOD at 550 nm is assimilated through three-dimensional variational data assimilation. The resulting AOD increments are mapped to three-dimensional aerosol mixing-ratio increments using analysis (Kalman)

gain matrix $\mathbf{K} = \mathbf{P}_f \mathbf{H}^T (\mathbf{H} \mathbf{P}_f \mathbf{H}^T)^{-1}$, where \mathbf{H} is the linearised observation operator relating model aerosol profiles to column AOD (i.e., $\mathbf{H}(x) = \text{AOD}$), and \mathbf{P}_f is the forecast-error covariance matrix. This gain distributes the AOD innovation vertically and across aerosol species according to their optical sensitivities and prescribed background-error correlations, yielding dynamically and optically consistent updates of black carbon (BC) and organic carbon (OC) by level and species. BC and OC are not directly observed; rather, they are inferred from the assimilated AOD constraint combined with modelled radiation, transport, and assumed aerosol optical and microphysical properties (externally mixed tracers; hygroscopic growth as a function of relative humidity (RH); OPAC optical properties and non-spherical dust treatment). Emissions for carbonaceous aerosols include QFED (Quick Fire Emissions Dataset, FRP-based) biomass-burning sources as well as fossil and biofuel emissions, while removal processes comprise dry and wet deposition and scavenging. Oxidant fields follow monthly climatological values. A background-state correction and averaging-kernel diagnostic are applied to ensure consistency between the 3 h AOD analyses and the 6 h meteorological assimilation cycle.

In summary, MERRA-2 BC and OC fields arise from AOD assimilation constrained by radiative transfer and transport, under fixed assumptions regarding particle size distribution, mixing state, vertical structure, and emissions (Buchard et al., 2015; Buchard et al., 2016; Darmanov and da Silva, 2015; Randles et al., 2017).

2.3 Comprehensive Study of SOD and Atmospheric Properties

This section describes the methodology used to derive the optical and microphysical properties of wildfire smoke from the BRAMS-simulated $\text{PM}_{2.5}$ fields. Although BRAMS-SFIRE internally represents aerosol–radiation interactions, the corresponding optical diagnostics are not available in the analysis output fields. For this reason, all radiative quantities examined in this study were obtained through offline post-processing. A set of microphysical assumptions, including particle size distribution, hygroscopic growth, refractive index, and ageing state, was adopted to translate $\text{PM}_{2.5}$ mass into wavelength-dependent extinction and absorption. These choices (summarised in Table 3 described in the Sect. 2.3.6) ensure physical consistency with observed biomass-burning aerosols and provide a coherent framework for the multi-stage optical analysis presented in Sect. 2.3.1–2.3.8.

To enable a consistent comparison between SOD and AOD, it is also necessary to clarify the spectral behaviour of smoke aerosols and the physical interpretation of column optical depth, both in the BRAMS framework and in the MERRA-2 reanalysis.

2.3.1 Spectral SOD analysis and validation

This section introduces the definition of smoke optical depth (SOD) and the methodology used to compute its spectral dependence from the BRAMS-simulated $\text{PM}_{2.5}$ field. It establishes the optical formulation, extinction, absorption, and scattering, that forms the basis for the microphysical refinements developed in the subsequent sections.

In this study, the SOD associated with the Sertão wildfire is quantified in terms of its magnitude, spectral dependence, and sensitivity to atmospheric conditions. SOD is defined as the vertical integral of the aerosol extinction coefficient, combining wavelength-dependent scattering and absorption (Seinfeld and Pandis, 2016). To compute SOD from the BRAMS $\text{PM}_{2.5}$ output, the aerosol population is represented using a lognormal dry-size distribution whose wet radius is modified through κ -Köhler hygroscopic growth, and optical efficiencies are evaluated using Mie theory. Meteorological variables such as temperature, relative humidity, and wind field, interact with the aerosol thermodynamic state and transport, conditioning hygroscopic growth and spatial redistribution, thereby influencing the computed spectral extinction. The aerosol population is assumed to follow a lognormal size distribution characterized by a geometric mean radius and geometric standard deviation, with size evolution constrained by effective radii reported in field studies of biomass burning smoke (Reid et al., 2005).

Hygroscopic growth is parameterized with the κ -Köhler approach (Petters and Kreidenweis, 2007), using κ values representative of fresh and mixed smoke conditions (Carrico et al., 2008; Engelhart et al., 2012). These parameterizations ensure consistency between modelled particle growth and observed microphysical properties reported in biomass burning studies. Under these assumptions, the extinction coefficient at wavelength λ and height z is given by Eq. (17), and the smoke optical depth follows as its vertical integral:

$$\beta_{\text{ext}}(z, \lambda) = \int_{r_{\min}}^{r_{\max}} Q_{\text{ext}}(m_{\text{eff}}(z, \lambda), r_{\text{wet}}, \lambda) \cdot \pi r_{\text{wet}}^2 n_{\text{dry}}(r_{\text{dry}}, z) dr_{\text{dry}} \quad (17)$$

$$\text{SOD}(\lambda) = \int_{z_0}^{z_t} \beta_{\text{ext}}(z, \lambda) dz \quad (18)$$

Where $r_{\text{wet}} = g(t, \text{RH}) r_{\text{dry}}$. Here, Q_{ext} is the Mie extinction efficiency (dimensionless), m_{eff} is the effective complex refractive index, r_{wet} is the physical (wet) particle radius “seen” by the light, and $n_{\text{dry}}(r_{\text{dry}}, z)$ is the differential number distribution with respect to dry radius [cm^{-4}] such that $\int n_{\text{dry}} dr_{\text{dry}} = N(z)$ [cm^{-3}]. Unit consistency is enforced internally (radii converted to a consistent length unit before evaluating πr^2). Because both Q_{ext} and πr^2 depend on the instantaneous particle size, all optical terms are evaluated with the wet radius r_{wet} .

2.3.2 Hygroscopic growth

Having established the optical formulation for SOD, the analysis turns to the hygroscopic growth of smoke particles, a key process that links ambient relative humidity to changes in particle size and refractive index. Because condensation and coagulation are not represented in the BRAMS–SFIRE output used in this research, hygroscopic growth is applied offline using the κ -Köhler framework, ensuring physically consistent wet-radius estimates for the extinction calculations.

Since condensation and coagulation are not explicitly modelled, hygroscopic growth is parameterized with the κ -Köhler approach (Petters and Kreidenweis, 2007):

$$g(t, \text{RH}) = \left(1 + \kappa \frac{\text{RH}}{1 - \text{RH}}\right)^{\frac{1}{3}} \quad (19)$$

where κ is the hygroscopicity parameter. Reported values in the literature suggest:

- fresh/organic-dominated smoke: $\kappa \approx 0.06\text{--}0.30$ (Carriço et al., 2008).
- mixed/transitioning smoke: $\kappa \approx 0.08\text{--}0.30$ centered ≈ 0.2 (Engelhart et al., 2012).

These ranges reflect the variability observed across biomass-burning aerosol types and combustion conditions. In this study, the specific κ values adopted for the diagnostic optical calculations are described in Sect. 2.4.5. Within each scenario (fresh or mixed), κ is treated as a composition-dependent physical parameter and is taken to be constant across the aerosol size distribution, following common practice in previous observational and modelling studies.

2.3.3 Size-distribution support and quadrature

After defining the hygroscopic growth treatment, this section describes how the underlying dry aerosol size distribution is represented for the subsequent Mie extinction and scattering calculations. The aerosol population is described by a lognormal distribution characterised by a geometric mean (modal) dry radius r_g and geometric standard deviation σ_g .

To ensure full numerical support of the distribution, the integration bounds for the dry radius are defined as:

$$r_{\text{dry}} \in [r_{\min}, r_{\max}] = [r_g \sigma_g^{-k}, r_g \sigma_g^k] \quad (20)$$

with $k \approx 3$. Values in the range $k \approx 3\text{--}4$ are commonly recommended (Hinds, 1999; Seinfeld and Pandis, 2016), as they capture virtually all number and mass contained in a lognormal mode. The chosen value ensures that the optical integration fully resolves the aerosol population relevant to biomass-burning smoke.

The radius interval is discretised logarithmically. Although 60–100 bins are traditionally advised for Mie calculations (Bohren and Huffman, 2008; Seinfeld and Pandis, 2016), a

grid-convergence test conducted here (30 vs. 80 bins) showed negligible differences in bulk and spectral moments (extinction, SSA, AOD). Therefore, $n = 30$ bins were adopted to reduce computational cost without compromising accuracy.

To evaluate the Mie integrals numerically, the continuous radius interval $[r_{\min}, r_{\max}]$ is discretised into n logarithmically spaced nodes, defined as:

$$r_j = r_{\min} \left(\frac{r_{\max}}{r_{\min}} \right)^{\frac{j-1}{n-1}}, \quad j = 1, \dots, n \quad (21)$$

2.3.4 Relating r_e to (r_g, σ_g)

Since most field observations report effective radii rather than lognormal parameters, this section links the observed effective radius r_e to the geometric mean radius r_g and geometric standard deviation σ_g , which are required for the size-distribution model. This conversion ensures consistency between observational constraints and the microphysical inputs used in the extinction calculations.

Most field studies provide the ambient effective radius r_e , not the pair (r_g, σ_g) . Because the single r_e does not uniquely identify both parameters: (i) the ambient r_e was converted to dry effective radius using the hygroscopic growth factor $g(\text{RH})$, and (ii) σ_g was prescribed within literature-based ranges for biomass-burning fine mode aerosols ($\sigma_g \approx 1.5\text{--}1.9$, typically narrowing with aging; Reid et al. (2005), see Sect. 2.4.5). The corresponding dry r_g then follows from the lognormal moment relation (Hinds, 1999; Seinfeld and Pandis, 2016):

$$\begin{aligned} \langle r^k \rangle &= r_g^k \exp\left(\frac{1}{2} k^2 \ln^2 \sigma_g\right), \\ r_e &= \frac{\langle r^3 \rangle}{\langle r^2 \rangle} = r_g \exp\left(\frac{5}{2} \ln^2 \sigma_g\right) \end{aligned} \quad (22)$$

Yielding,

$$r_g = \frac{r_e}{\exp\left(\frac{5}{2} \ln^2 \sigma_g\right)} \quad (23)$$

A sensitivity analysis across plausible σ_g values quantify the uncertainty in the retrieved r_g and in all subsequently derived optical properties.

2.3.5 Mass-consistent normalization and mass fractions

With the size-distribution framework established, the next step was the partition of the simulated $\text{PM}_{2.5}$ mass consistently across the discretised radius bins. This section introduces the mass-fraction formalism used to distribute dry mass, derive bin-resolved number concentrations, and construct internally consistent lognormal sub-populations for Mie calculations.

Let $\tilde{n}(r)$ denote the unnormalized lognormal shape (any proportional form is acceptable because the normalisation cancels in fractions). The mass fraction in bin j over $[r_j^-, r_j^+]$ is

$$f_j^{(M)} = \frac{\int_{r_j^-}^{r_j^+} r^3 \tilde{n}(r) dr}{\int_{r_{\min}}^{r_{\max}} r^3 \tilde{n}(r) dr} \quad (24)$$

Thus, $f_j^{(M)}$ is independent of the total number concentration N since the normalization cancels. Given the bulk dry $\text{PM}_{2.5}$ mass concentration $C_m(t)$ in a model layer, the -resolved masses follow $M_j = f_j^{(M)} C_m(t)$. If bin-wise number concentrations are required, they can be obtained from the third-moment closure of a lognormal distribution (Curci et al., 2015),

$$N_j = \frac{M_j}{\rho_j \frac{4}{3} \pi r_{g_j}^3 \exp\left(\frac{9}{2} \ln^2 \sigma_{g_j}\right)} \quad (25)$$

where ρ_j is the dry effective density associated with the aerosol composition in bin j .

The bin-resolved lognormal number distribution is then,

$$n_j(r) = \frac{N_j}{\sqrt{2\pi r \ln \sigma_{g_j}}} \exp\left[-\frac{\ln^2(r/r_{g_j})}{2 \ln^2 \sigma_{g_j}}\right] \quad (26)$$

This ensures that each bin possesses an internally consistent lognormal sub-population whose mass, number, and spectral moments match those used in the optical calculations.

2.3.6 Aging scenarios

To represent the temporal evolution of smoke microphysics during the fire, two plume-age scenarios were adopted, following established observational classifications. This section defines the “fresh” and “mixed” smoke regimes, specifies their associated microphysical properties, and links these to the simulation setups described later in Sect. 2.4.5.

Two plume-age scenarios were considered (Andreae and Rosenfeld, 2008; Reid et al., 2005), since the studied fire lasted ~ 11 h and did not reach plume ages representative of aged/scattering conditions:

$$t = \{t_1: \text{fresh/absorbing}; t_2: \text{mixed}\}$$

These scenarios are summarized in Table 3. The SOD was integrated hourly within each phase, with phase durations taken as ~ 6 h intervals.

The microphysical characteristics (κ) and bounds ($\sigma_{g, \text{dry}}$) defined for the t_1 and t_2 phases, used in the Baseline, Conservative, and Lower Envelope setups for all SOD, SSA, extinction, and absorption calculations, were selected from the hygroscopic growth definitions in Sect. 2.3.2 and from Table 3, and are formally presented in Sect. 2.4.5.

2.3.7 Derivation of MERRA-2 single-scattering albedo

Since modelled optical properties are compared against MERRA-2 reanalysis, this section describes how single-scattering albedo (SSA) is derived from the species-resolved extinction and scattering optical depths provided by MERRA-2. The same diagnostic formulation is then applied to the BRAMS–SFIRE output to ensure strict consistency in the comparison.

MERRA-2 provides column-integrated aerosol optical extinction and scattering optical depths (AOD) at 550 nm, resolved by process and by species (BC, OC, and total). The single-scattering albedo (SSA) is defined as the ratio of scattering to total extinction:

$$\text{SSA} = \frac{\tau_{\text{sca}}}{\tau_{\text{ext}}} \quad (27)$$

From the MERRA-2 fields and from the model outputs, species-specific SSA were computed as:

$$\text{SSA}_{\text{BC}} = \frac{\tau_{\text{sca}}^{\text{BC}}}{\tau_{\text{ext}}^{\text{BC}}}; \text{SSA}_{\text{OC}} = \frac{\tau_{\text{sca}}^{\text{OC}}}{\tau_{\text{ext}}^{\text{OC}}}; \text{SSA}_{\text{tot}} = \frac{\tau_{\text{sca}}^{\text{tot}}}{\tau_{\text{ext}}^{\text{tot}}} \quad (28)$$

A combined smoke SSA representative of the fine-mode carbonaceous fraction was also derived as:

$$\text{SSA}_{\text{BC+OC}} = \frac{\tau_{\text{sca}}^{\text{BC}} + \tau_{\text{sca}}^{\text{OC}}}{\tau_{\text{ext}}^{\text{BC}} + \tau_{\text{ext}}^{\text{OC}}} \quad (29)$$

This same formulation was applied to the BRAMS–SFIRE simulations to ensure consistency with the MERRA-2 diagnostic structure and to enable a direct comparison of modelled and reanalysis optical properties.

2.3.8 Optical properties and spectral dependence of smoke aerosols

Having defined the microphysical and radiative components of the smoke model, this section details the spectral behaviour of extinction and absorption across the visible wavelengths. It outlines the refractive-index parameterisation, motivates the selected wavelengths (400, 550, 700 nm), and presents the resulting spectral signatures relevant for the radiative impacts examined later.

The specific extinction efficiency was computed using Mie theory as a function of particle radius, wavelength, and complex refractive index. A wavelength-dependent refractive index was prescribed following observational and review studies on biomass-burning aerosols (Andreae and Gelencsér, 2006; Bond and Bergstrom, 2006; Kirchstetter and Novakov, 2004; Reid et al., 2005). In this parameterisation, the real part was held approximately constant at ~ 1.55 , consistent with values typically reported for smoke particles, while the imaginary part decreases with wavelength, reflecting the stronger absorption of chromophoric organics (brown carbon) in the near-UV and blue. Although the refractive-index formulation

Table 3. Classification of smoke-plume aging scenarios adopted in this study based in Reid et al. (2005).

Phase	Plume age	Classification	σ_g	GMD (μm)	$r_g = \frac{\text{GMD}}{2}$ (μm)	$[r_{\min}, r_{\max}]$ ($k = 3, \sigma_g = 17$) (μm)	Notes
t_1	0–6 h (Local time: 13:00–18:00)	Fresh/flaming (absorbing)	1.6–1.8 (typ. 1.7)	0.10–0.16 (centre ~ 0.13)	0.05–0.08 (typ. 0.065)	[0.013, 0.319] for ($r_g = 0.065$)	Fresh cores; very high number; rapid early growth observed.
t_2	6–12 h (Local time: 19:00–23:00)	Mixed/transition (incl. smouldering)	1.6–1.9 (typ. 1.7)	0.12–0.30 (most common ≈ 0.18)	0.06–0.15 (typ. 0.09)	[0.012, 0.442] for ($r_g = 0.09$)	Transition with smouldering + coagulation + some hygroscopic growth.

Note: For a strictly lognormal distribution, the Count Median Diameter (CMD) and the Geometric Mean Diameter (GMD) are equivalent.

adopted here reflects the dominant OC-rich composition of the plume, the wavelength-independent absorption behaviour of BC and its implications for radiative transfer are analysed separately in Sect. “Sensitivity to more absorbing BC-like refractive index”.

Refractive-index values used and justification

In this study, the complex refractive index was chosen to represent the plume-integrated optical properties of organic-dominated fine-mode smoke, consistent with the carbonaceous composition diagnosed for the Sertã plume. The imaginary component k was set to 0.01–0.03 across 400–700 nm, representing weak absorption characteristic of primary and secondary organic aerosol (Chakrabarty et al., 2016; Kirchstetter and Novakov, 2004). These values are substantially lower than those of fresh black carbon, for which k typically ranges from 0.44 to 0.71 in the visible spectrum (Bond and Bergstrom, 2006; Curci et al., 2015)

Rationale for Departing from BC-Like Optical Properties

BRAMS-SFIRE provides bulk $\text{PM}_{2.5}$ mass, not speciated BC/OC fields. Because BC constitutes only a small fraction of the simulated carbonaceous mass (see Fig. 9 described in Sect. 3.3) and is confined to a narrow region near the flaming core, prescribing a BC-like refractive index would artificially amplify absorption across the broader plume. The weaker k values therefore represent the plume-average optical behaviour, governed primarily by scattering from OC-rich aerosols, consistent with the MERRA-2 OC extinction fields (see Figs. 10–11 described in Sect. 3.3).

For transparency, the wavelength-specific values used in the optical solver were $1.55 + 0.04i$ at 400 nm, $1.55 + 0.02i$ at 550 nm, $1.55 + 0.01i$ at 700 nm. These parameters were used in the Mie computations to derive the wavelength-dependent extinction and scattering efficiencies.

Sensitivity to more absorbing BC-like refractive index

Sensitivity tests performed with a BC-like refractive index ($k \approx 0.4$) showed enhanced absorption only near the fire

front but minimal impact on domain-integrated SOD, SSA, or the SOD–AOD coupling. This behaviour is consistent with previous findings that BC strongly influences absorption in small source-proximal regions but contributes far less to plume-integrated optical depth when OC dominates the aerosol mass (Bond et al., 2013; Lack and Cappa, 2010).

Thus, the refractive-index values adopted here should be interpreted as plume-representative rather than BC-representative, while acknowledging that absorption by fresh BC is likely underrepresented, a structural limitation reflected in the optical diagnostics discussed in Sect. 3.3 and in the thermodynamic response analysed in Sect. 3.5.

Spectral dependence motivating the choice of wavelengths

Aerosols produced during flaming combustion are largely composed of OC and BC, both of which influence radiative transfer by reducing visibility and surface irradiance (Bond et al., 2004).

Black carbon, consisting of turbostratic graphitic aggregates (Biscoe and Warren, 1942), exhibits nearly wavelength-independent absorption across the visible range (Bond and Bergstrom, 2006).

Organic carbon, especially brown carbon, absorbs strongly at short wavelengths, with absorption efficiency decreasing rapidly from the near-UV/blue toward the red and near-infrared (Andreae and Gelencsér, 2006; Kirchstetter and Novakov, 2004).

These properties motivated the three wavelengths used:

- 400 nm: strong OC/BrC absorption, strong refractive-index contrast
- 550 nm: standard reference band used in satellite retrievals and aerosol studies
- 700 nm: absorption dominated by BC as OC becomes optically weak

Although the absolute absorption by BC decreases slowly with wavelength, its relative importance increases at longer wavelengths.

Diagnostic quantities

Smoke Optical Depth (SOD) was computed at each wavelength by vertically integrating the extinction and absorption coefficients along meridional and zonal cross-sections. In this study, SOD represents the column-integrated smoke burden produced by the BRAMS–SFIRE system and is therefore used both as a physically meaningful depiction of plume structure and as the primary variable for comparison with satellite- and MERRA-2-derived AOD. This comparison was performed at the same wavelength (550 nm) to ensure compatibility with satellite retrievals. Single-scattering albedo (SSA), diagnostically derived from the modelled extinction and scattering fields, was compared with MERRA-2 SSA for the BC, OC, and total aerosol channels. Although the MERRA-2 files label BC and OC variables as AOT, we refer to them as AOD for consistency with standard aerosol terminology. Additionally, SOD at 550 nm was compared with MERRA-2 BC and OC extinction AOD, and simulated PM_{2.5} concentrations were evaluated against MERRA-2 BC/OC mass concentrations.

In contrast, the diagnosis of smoke–radiation–stability interactions was based on the spectrally resolved extinction and absorption coefficients (SEC and SAC), which directly control radiative heating rates and thereby modulate the thermodynamic response of the lower troposphere. Whereas SOD assesses how the model reproduces the large-scale optical signature and spatial organisation of the plume, SEC and SAC quantify the local radiative forcing that drives changes in stability within the boundary layer.

2.4 Gridding, Background Correction, and Sensitivity Tests

The evaluation of SOD against MERRA-2 products requires three methodological components: (i) a spatial harmonisation procedure enabling point-to-point comparison; (ii) a background correction that isolates the fire-induced optical contribution; and (iii) sensitivity tests that quantify how microphysical uncertainties affect the optical diagnostics.

This section describes these three elements, highlighting their interconnections and significance. First, the regridding strategy used to place the BRAMS grid and the MERRA-2 reanalysis fields onto a common spatial framework is described. Next, the methodology adopted to remove the contribution from regional background aerosols present in MERRA-2, which is due to its representation of large-scale sources, but absent in the BRAMS–SFIRE simulation that only contains fire-emitted smoke, is defined. Finally, the diagnostic scenarios applied in the optical post-processing to assess the robustness of the results and their stability with respect to microphysical uncertainty, are outlined.

2.4.1 Apples-to-apples gridding

To enable a meaningful comparison between BRAMS–SFIRE and MERRA-2 aerosol fields, the MERRA-2 data were remapped onto the native BRAMS grid using a consistent interpolation framework. All analyses were conducted on the 2 km BRAMS–SFIRE outer-domain grid to ensure spatial representativeness and to minimize interpolation-induced artifacts. MERRA-2 aerosol variables were bilinearly interpolated onto the BRAMS latitude–longitude grid within the common sub-domain (with longitudes wrapped to $[-180, 180]$), providing a one-to-one spatial pairing between datasets. Diagnostics included Total Aerosol Extinction AOD ($AOD_{Total_{ext}}$) and Total Aerosol Scattering AOD ($AOD_{Total_{scat}}$) at 550 nm, from which the MERRA-2 single-scattering albedo was computed as:

$$SSA_{MERRA} = AOD_{Total_{scat}} / AOD_{Total_{ext}} \quad (30)$$

Where available, extinction and scattering contributions from BC and OC were also incorporated. Temporal matching used the nearest MERRA-2 timestamp corresponding to each BRAMS output time.

2.4.2 Upwind/background subtraction

Because MERRA-2 includes a regional aerosol load that is absent from the BRAMS fire-plume simulation, a background correction was applied to ensure that the comparison reflects only the fire-related contribution to AOD. The background field was estimated using an upwind method that identifies clean-air regions based on the inflow direction. This definition is physically consistent with the advection of background air entering the domain prior to interaction with the smoke plume. An upwind AOD field was computed on the BRAMS grid, and the plume-only optical depth was defined as:

$$AOD' = \max(AOD - AOD_{upwind}, 0) \quad (31)$$

Upwind boundaries were determined from near-surface winds (u_{10}, v_{10}) or, when unavailable, from the mean wind in the lowest five model layers. The upwind band spanned 18 % of the domain along the inflow edges (W if $u > 0$, E if $u < 0$; S if $v > 0$, N if $v < 0$). Within this region, AOD_{upwind} was defined as the median of the lower half of AOD values, providing a robust estimate of the clean-air background while minimising contamination from the plume.

2.4.3 Phase windows vs. diagnostic scenarios

The optical analysis distinguishes between physical plume-age phases (t_1 : 13:00–18:00 UTC “fresh”, t_2 : 19:00–24:00 UTC “mixed”) and diagnostic perturbation scenarios. The plume-age phases define the baseline microphysical parameters used in the optical calculations ($\sigma_g, \kappa, r_{g,dry}$). The diagnostic scenarios (BASE, ABSORBING, WIDE SIGMA,

SMALL RG, LARGE RG) are then applied within each phase as controlled perturbations to these baseline parameters, while keeping the aerosol mass fixed. For each phase and each diagnostic scenario, an independent set of statistical validation analyses is performed, as described in the following section.

2.4.4 Phase selection and scope

Since the fire plume evolves rapidly during daytime and becomes more spatially coherent after sunset, selecting an appropriate evaluation window is essential. This section provides the rationale for focusing the primary analysis on the mixed-phase period and explains how this choice improves statistical stability.

To reduce diurnal aliasing and ensure stable grid-point pairing, the main evaluation of this research focuses on the mixed phase period (19:00–24:00 local time), when the plume is more slowly evolving and spatial gradients are weaker. This choice minimizes sensitivity to sub-grid plume meandering and transient emission spikes that are more pronounced during early-afternoon hours, providing more stationary conditions for statistical comparison with the reanalysis. Domain-wide all-hours aggregates are also included for completeness.

2.4.5 Microphysical phase windows and simulation setups

In addition to temporal stratification, optical analysis requires specifying phase-dependent microphysical parameters. This section defines the microphysical configurations associated with fresh-smoke and mixed-smoke periods and describes how these parameters are used to define the diagnostic scenarios (BASE, ABSORBING, WIDE SIGMA, SMALL RG, LARGE RG) described in Sect. “Microphysical perturbation scenarios”, which are designed to bracket the Mie-based optical calculations.

To represent plausible within-plume microphysical evolution while preserving mass consistency, two temporal phase windows (t_1 and t_2) were considered. For each phase and scenario, a representative set of microphysical parameters was selected within the ranges defined in Table 3 (Sect. 2.3.6), based on physically plausible values of the lognormal size distribution and hygroscopicity. One-at-a-time sensitivity perturbations were then applied. These scenarios span conservative and lower-bound microphysical states:

– Baseline:

t_1 – fresh/absorbing: $\sigma_g = 1.70$, $\kappa = 0.12$, $r_{g,dry} = 0.065 \mu\text{m}$,

t_2 – mixed: $\sigma_g = 1.70$, $\kappa = 0.20$, $r_{g,dry} = 0.090 \mu\text{m}$

– Conservative (narrower/less hygroscopic):

t_1 – fresh/absorbing: $\sigma_g = 1.60$, $\kappa = 0.08$, $r_{g,dry} = 0.060 \mu\text{m}$

t_2 : mixed: $\sigma_g = 1.60$, $\kappa = 0.14$, $r_{g,dry} = 0.080 \mu\text{m}$

– Lower Envelope (most conservative bounds used):

t_1 – fresh/absorbing: $\sigma_g = 1.60$, $\kappa = 0.06$, $r_{g,dry} = 0.055 \mu\text{m}$

t_2 – mixed: $\sigma_g = 1.60$, $\kappa = 0.10$, $r_{g,dry} = 0.070 \mu\text{m}$

For all scenarios and wavelengths used in the SOD, SSA, and extinction/absorption calculations, the complex refractive index was prescribed as:

$$m(\lambda) = \{400 : 1.55 + 0.04i; 550 : 1.55 + 0.02i; 700 : 1.55 + 0.01i\} \quad (32)$$

No additional spectral perturbations were applied beyond these baseline values. Mie calculations were evaluated at 400, 550, and 700 nm wavelengths. The geometric integration bounds for the lognormal distribution were fixed at $k = 3$, ensuring consistent coverage ($\sim \pm 3\sigma$) radius coverage across all cases. Consequently, the sensitivity analysis isolates the effects of σ_g , κ and $r_{g,dry}$ without modifying the prescribed refractive indices $m(\lambda) = n(\lambda) + ik(\lambda)$. In particular, no additional increment of the imaginary refractive indices part (e.g., no +0.02 at 550 nm) and no changes to the spectral slope of $k(\lambda)$ were introduced.

All statistical metrics (correlation, bias, RMSE, etc.) were computed from the same Mie-derived optical fields, consistently evaluated at 550 nm using the wavelength-dependent refractive index $m(550) = 1.55 + 0.02i$.

2.4.6 Diagnostic post-processing experiments for optical sensitivity and background treatment

To assess how uncertainties in aerosol microphysics and background aerosol load affect the optical diagnostics, a suite of controlled post-processing sensitivity experiments was performed. These experiments modify only the microphysical parameters used by the Mie optical calculator and the background treatment applied to AOD, while the simulated aerosol mass fields ($\text{PM}_{2.5}$) remain unchanged. This design isolates the optical response to microphysical assumptions and background biases without altering the underlying BRAMS–SFIRE plume dynamics.

Microphysical perturbation scenarios

The microphysical configurations defined in Sect. 2.4.5 (Baseline, Conservative, and Lower Envelope states) serve as reference parameter sets for the optical calculations. The diagnostic perturbation scenarios described below (BASE, ABSORBING, WIDE SIGMA, SMALL RG, LARGE RG)

are applied to these reference states to assess the sensitivity of the optical properties to individual microphysical parameters.

Let σ_g , κ , and $r_{g,dry}$ denote the phase-dependent baseline parameters defined in Sect. 2.4.5. Each diagnostic scenario modifies these parameters through multiplicative scaling factors, such that σ_g , κ , and $r_{g,dry}$ are replaced by $s_g\sigma_g$, $s_\kappa\kappa$, and $s_r r_{g,dry}$, respectively, and/or an additive increment in the imaginary part of the refractive index $k(\lambda)$:

- *BASE*: reference optics for the active phase, using the unmodified microphysical parameters;
- *ABSORBING*: enhanced intrinsic absorption and reduced hygroscopicity ($k(\lambda) = +0.02$ at 550 nm; $\kappa \times 0.6$);
- *WIDE SIGMA*: broader size distribution ($\sigma_g \times 1.10$) with the lognormal grid discretised over $n = 30$ radius bins $[r_g\sigma_g^{-3}, r_g\sigma_g^3]$;
- *SMALL/LARGE RG*: reduced or increased dry geometric radius ($r_{g,dry} \times 0.80$ or 1.2), representing plausible bounds for each phase rather than arbitrary $\pm 20\%$ variations.

These perturbations are purely diagnostic and are applied independently to quantify how variations in σ_g , κ , $r_{g,dry}$, and $k(\lambda)$ influence extinction, scattering, absorption, SOD, and SSA.

Background-subtracted anomaly fields

Depending on the diagnostic objective, comparisons may be performed using either the raw optical depth fields or background-subtracted anomaly fields. A binary flag (TRUE/FALSE) indicates whether background removal is applied before computing the statistical metrics:

- FALSE – no background subtraction:
Statistics are computed from the raw fields, $X = \text{AOD}$, $Y = \text{SOD}$
- TRUE – with background subtraction:
A background level is diagnosed for each hourly field to isolate the smoke-related anomaly.

Background estimation

The background AOD (AOD_{bg}) is obtained using the upwind clean-air region identified according to Sect. 2.4.2. For each hour:

1. The inflow direction is determined from the near-surface winds (10 m) or, when unavailable, from the mean wind in the lowest five model layers.

2. An upwind band corresponding to 18 % of the domain width is extracted along the inflow boundary.
3. AOD_{bg} is defined as the median of the lower half of AOD values within this upwind band, a conservative estimator designed to minimize residual plume influence.

The same methodology is applied to obtain SOD_{bg} , although in practice BRAMS has negligible regional aerosol loading and $\text{AOD}_{bg} \approx 0$.

Anomaly fields are:

$$\text{AOD}' = \max(\text{AOD} - \text{AOD}_{bg}, 0)$$

$$\text{SOD}' = \max(\text{SOD} - \text{SOD}_{bg}, 0)$$

Statistical comparison is then computed using $X = \text{AOD}'$, $Y = \text{SOD}'$

This procedure removes the nearly constant regional aerosol offset present in MERRA-2 but absent from the simulated plume, typically reducing bias, lowering the regression intercept, and strengthening correlation and linearity in the SOD–AOD relationship.

Workflow of the diagnostic post-processing

The full statistical diagnostics for all microphysical sensitivity scenarios (BASE, ABSORBING, WIDE_SIGMA, SMALL_RG, LARGE_RG), spatial masks (ALL, P70, P80, P90), and background configurations (AOD vs. AOD') are computed using this post-processing workflow. These results are presented in Tables 5 and 6 of Sect. 3.3, with the full set of diagnostics provided in the Supplement (Tables S1–S3) and are further discussed in Sect. 3.2 and 3.3 of the Results and Discussion.

2.4.7 Evaluation metrics and visualization

A consistent set of statistical metrics is required to quantify differences between simulated and reanalysis optical properties. This section describes the evaluation framework used for the main BRAMS–MERRA-2 comparison, including the metrics, temporal pairing, and visualisation strategy.

Model–reanalysis pairs were formed on the native BRAMS grid after bilinear interpolation of MERRA-2 and nearest-hour temporal pairing. Statistics were computed both for the raw AOD and for the background-corrected field,

$$\text{AOD}' = \max(\text{AOD} - \text{AOD}_{upwind}, 0) \quad (33)$$

using all valid grid-point pairs over the common domain (i.e., no percentile-based plume masks were applied).

The diagnostic set comprised means of X and Y , bias ($X - Y$), mean absolute error (MAE), root-mean-square error (RMSE), Pearson correlation coefficient (r), and Spearman's rank correlation coefficient (ρ), and ordinary-least-squares (OLS) linear fit $Y = aX + b$ with coefficient of determination (R^2). The primary evaluation used $X = \text{SOD}_{550}$ and

$Y \in \{AOD_{550}, AOD'_{550}\}$. The same framework was applied to SOD vs. BC/OC extinction and to model-diagnosed SSA vs SSA from MERRA-2. Hourly diagnostics were subsequently aggregated into all-hours statistics.

Scatter plots were rendered as log-density hexbin diagrams to avoid overplotting. Each diagram was rendered as log-density hexbin plots, including the 1 : 1 reference line, the OLS regression, and annotated values of the key statistics (e.g., r , ρ , RMSE, bias and R^2) ensuring visual and quantitative consistency with the tabulated metrics.

All hourly statistical results derived from this evaluation framework, are presented in Table 4 and scatter plots in Fig. 8, discussed in Sect. 3.2, and scatter plots in Figs. 11 and 13, discussed in Sect. 3.3 of the Results and Discussion.

2.4.8 PM_{2.5} Quality Assurance and Plume-Evolution Diagnostics

In addition to the optical and microphysical diagnostics, a set of supplementary procedures was implemented to verify the physical consistency of the simulated aerosol fields and to examine their spatial and temporal evolution during the wildfire event. These quality-assurance analyses were performed independently from the optical post-processing and serve to document the behaviour of the PM_{2.5} mass field that underpins the SOD calculations.

Distribution checks and hourly histograms

To examine the spatial distribution of simulated surface PM_{2.5} concentrations, two complementary histogram-based diagnostics were used.

The first diagnostic, shown in Fig. 14 (Sect. 3.4), consists of hourly histograms constructed from all PM_{2.5} surface values at selected times. These histograms use a fixed number of concentration bins and a logarithmic frequency axis, providing an instantaneous view of the spatial distribution at those specific hours. They are intended to highlight features such as broad upper tails or isolated high-value spikes that may influence the interpretation of the optical fields.

The second diagnostic, illustrated in Fig. 15 (Sect. 3.4), is a histogram representative of a particular hour extracted from a continuous, hour-by-hour quality-assessment procedure applied throughout the simulation period. While the binning strategy is similar to that used in Fig. 14, this diagnostic serves a different purpose: it documents the distribution of PM_{2.5} at each hour as part of a systematic evaluation of numerical consistency, unit handling, and physical plausibility. The figure shown corresponds to one of these hourly distributions.

Together, these two diagnostics provide complementary perspectives, Fig. 14 focuses on selected hours relevant to the optical analysis, while Fig. 15 represents the broader quality assessment-oriented evaluation conducted across all simulation times.

Column-integrated PM_{2.5} evolution north of the fire line

A complementary plume-evolution diagnostic focused on the portion of the domain located north of a fixed latitude threshold (40.35° N). For each hourly output, the vertically integrated PM_{2.5} column mass was computed and summed over all grid cells north of this latitude. This metric serves as a bulk indicator of the amount of smoke crossing the latitude line and therefore provides insight into directional plume transport and the potential for dynamical trapping or stagnation.

The corresponding time series is presented in Fig. 22 and described in Sect. 3.6 of the Results and Discussion. This diagnostic allows interpretation of whether the plume is steadily advected, transiently confined near the source, or intermittently re-accumulated under weak-wind conditions, behaviour relevant for understanding plume–background interactions, residence times, and the temporal structure of the optical evaluation.

Local accumulation and meteorological co-variability

To characterize potential interactions between smoke loading and near-surface meteorology, PM_{2.5} column mass and sensible heat flux (H) were extracted at three representative locations along the plume pathway: a point near the fire origin, a midpoint within the valley corridor, and a downwind endpoint. For each site, hourly time series of column-integrated PM_{2.5} and sensible heat flux were constructed.

The PM_{2.5} series were accompanied by simple diagnostic indicators, namely the median, the p70–p90 range, and the hourly maximum, to highlight temporal fluctuations in column loading and to identify periods of enhanced local concentration. Sensible heat flux was co-plotted to document concurrent variations in surface forcing, enabling a qualitative assessment of the temporal co-variability between thermodynamic conditions and smoke loading.

This procedure provides an auxiliary, location-specific diagnostic framework used to contextualize plume behavior and near-surface meteorological conditions. The interpretation of these series is presented separately in Fig. 23 and in Sect. 3.6 of the Results and Discussion.

2.4.9 Quality control

Finally, to ensure reproducibility and physical consistency, all fields used in the analysis were subjected to systematic quality-control procedures. This section summarises the checks applied to meteorological, optical, and microphysical variables prior to statistical evaluation.

Relative humidity was clipped to the physically meaningful range [0, 0.999]. Heights were ingested directly in metres or, when stored as geopotential, converted using division by gravitational acceleration (g). Layer thicknesses were verified to remain within plausible atmospheric limits.

All configurable parameters, such as the upwind-band width, statistical options, and microphysical sensitivity factors, were explicitly documented to guarantee transparency and reproducibility of the diagnostic workflow.

2.5 Absorption of Solar Radiation by Smoke and Radiative Budget Impacts

Smoke aerosols modify the surface radiation budget through scattering and absorption of solar radiation. To quantify these effects, differences between simulations without and with fire emissions were evaluated using the accumulated surface downwelling shortwave (W m^{-2}) and longwave (W m^{-2}) radiative fluxes. This comparison provides a first-order estimate of how the presence of smoke alters the net radiative energy reaching the surface.

In addition to these broadband radiative diagnostics, the smoke-absorbed shortwave flux at 550 nm, $F_{\text{abs}}(550\text{ nm})$ (W m^{-2}), was estimated by relating the vertically integrated aerosol absorption to the heating potential of the plume. The column absorption optical depth at 550 nm is computed as:

$$\tau_{\text{abs}}(550) = \int_{z_0}^{z_t} \int Q_{\text{abs}}(m_{\text{eff}}(z, 550), g, r_{\text{dry}}, 550) \pi (g r_{\text{dry}})^2 n_{\text{dry}}(r_{\text{dry}}, z) \text{d}r_{\text{dry}} \text{d}z \quad (34)$$

where Q_{abs} is the Mie absorption efficiency for the effective refractive index m_{eff} , g is the hygroscopic growth factor, r_{dry} the dry particle radius, and n_{dry} the dry-number distribution.

A simplified diagnostic estimate of smoke-absorbed radiant energy is then obtained as:

$$F_{\text{abs}}(550\text{ nm}) = H_{\text{sen}} \tau_{\text{abs}}(550) \quad (35)$$

where H_{sen} is the surface sensible heat flux associated with fire. Although not a full radiative-transfer computation, this formulation provides a physically interpretable proxy linking absorption optical depth to the potential radiative heating within the plume.

2.6 Vertical Profiles of Aerosol Optical Properties and Atmospheric Stability

Building on the radiative impacts examined in Sect. 2.5, this section investigates how smoke-induced heating interacts with the vertical thermodynamic structure of the atmosphere. The analysis focuses on the coupling between aerosol optical properties, namely extinction and absorption and atmospheric stability in smoke-affected layers.

Atmospheric stability was evaluated using vertical profiles of potential temperature (θ) and relative humidity (RH), extracted along a longitudinal cross-section intersecting the plume. These profiles were displayed in paired panels, showing the differences between fire and no-fire conditions relative to the corresponding no-fire reference fields, thereby iso-

lating smoke-induced thermodynamic modifications. Thermal inversions were identified from layers where θ increases with height ($d\theta/dz > 0$), indicating inhibited vertical mixing. Although RH is not used as a formal inversion criterion, its vertical structure provides a supplementary indicator: sharp RH transitions or inflection points often coincide with inversion layers and therefore help delineate the vertical extent of stratified regions.

To relate thermodynamic modifications to aerosol–radiation interactions, vertical cross-sections of the smoke extinction coefficient (SEC) and smoke absorption coefficient (SAC) at 500 nm and 700 nm were analyzed together with CAPE and CIN diagnostics. CAPE and CIN were computed and displayed in paired panels for both the smoke and no-fire states. This layout provides a direct visual comparison between: (i) the underlying thermodynamic structure; (ii) the radiative perturbations induced by smoke (via SEC and SAC); and (iii) the corresponding stability response under convectively favorable (CAPE) or suppressed (CIN) conditions.

This combined framework, thermodynamic profiles, RH structure, and smoke optical properties, provides the basis for interpreting how absorption-driven heating may alter stratification and vertical mixing. The resulting cross-sections used in the analysis are presented in Figs. 17–21 of Sect. 3.5 (Results and Discussion), where their implications are examined in detail.

3 Results and discussion

This section first compares the burned area produced by the wildfire episode in Sertã as simulated by the BRAMS and WRF models, in order to evaluate fire-spread performance in a forested region with complex topography and dynamically evolving mountain–valley breezes. Second, the simulated Smoke Optical Depth (SOD) is evaluated against MERRA-2 AOD to assess spatial and temporal coherence over the region. Column-integrated extinction coefficients at 550 nm are also compared with extinction derived from MERRA-2 BC and OC aerosol components, to determine whether the simulated optical behaviour is consistent with the dominant aerosol types present during the event.

The simulated SSA is compared with MERRA-2 SSA, along with simulated and MERRA-2 aerosol mass concentrations, to validate whether the simulated aerosol composition, particularly the relative abundance of BC and OC, is consistent with observed radiative behaviour. This comparison also evaluates whether the simulated vertical mass profiles of BC, OC, and $\text{PM}_{2.5}$ are consistent with the resulting optical properties. Frequency distributions of surface $\text{PM}_{2.5}$ concentrations across the simulation domain are analysed to characterise the spatial variability of particulate loading and to identify the prevalence of low-, moderate-, and high-concentration regimes. In addition, the impact of smoke

absorption on surface downwelling shortwave and longwave radiation is assessed to determine how the simulated aerosol burden modifies the local radiative budget. The optical effects on atmospheric stability are investigated through the analysis of CAPE and CIN, which provide complementary measures of convective potential and suppression. Vertical profiles of extinction and absorption coefficients are further examined together with the development of thermal inversion layers, enabling an assessment of whether the model accurately reproduces the radiative signature of smoke and its influence on local thermodynamic structure.

3.1 BRAMS and WRF model differences in burned area representation and their implications

Significant differences in the simulated burned area for the same Sertã wildfire event, as depicted in Fig. 6, were observed between BRAMS-SFIRE and the WRF-SFIRE results previously reported by Menezes et al. (2024). BRAMS-SFIRE simulated a broader westward spread, while WRF-SFIRE produced a more confined footprint that extended further north. These discrepancies arise from differences in model configuration, fire propagation schemes, and spatial resolution.

First, although WRF-SFIRE resolves fire spread at a finer horizontal resolution (20 m) than BRAMS-SFIRE (200 m), BRAMS exhibits stronger sensitivity to terrain-induced effects due to its topographic assimilation and interaction with the atmospheric fields at coarser grid scales (2 km in diagnostics). This can amplify upslope spread, especially on west-facing slopes, where heating of unburned fuels by the flame front is intensified. Additionally, BRAMS employed a default rate of spread approximately ten times greater than that used in WRF, resulting in more aggressive lateral fire expansion, particularly in regions where wind-driven constraints are weaker.

Second, resolution differences in output diagnostics further influence the apparent burned area. WRF's higher resolution (20 m) output preserves more spatial detail, limiting the smoothing of the burned footprint. Conversely, the BRAMS burned area (200 m resolution) was accumulated and plotted in the BRAMS 2 km grid resolution, which introduces spatial averaging and may artificially enlarge the apparent extent of fire-affected regions.

Moreover, the delayed onset of burned area in BRAMS-SFIRE when using lower propagation rates is not solely due to ignition misalignment, but rather a result of the interaction between the fire spread rate and the coarser fire grid resolution (200 m). Unlike WRF-SFIRE, which operates at a much finer 20 m resolution for fire propagation, BRAMS requires the flame front to traverse larger grid cells to ignite neighbouring areas. This means that if the default rate of spread is reduced without compensating for grid size, the fire may fail to reach adjacent cells in a timely manner, leading to an underrepresentation of burned area in the early stages. There-

fore, a balanced calibration is needed between the fire spread rate and grid resolution in BRAMS to ensure that the ignition front progresses consistently with observed timelines. While finer resolution in WRF (20 m) inherently provides more accurate spatial detail in fire development (Menezes et al., 2024), BRAMS relies on a more approximate representation, making it sensitive to how rate-of-spread parameters are tuned relative to its mesh scale.

In summary, while WRF-SFIRE offers finer-scale detail in fire perimeter shape, BRAMS-SFIRE exhibits stronger coupling between fire dynamics, topography, and atmospheric feedbacks. For prognostic simulations of fire spread and smoke transport in complex terrain, BRAMS-SFIRE may provide enhanced physical realism, provided its rate of spread is properly calibrated to avoid over propagation, particularly in orographically enhanced directions.

3.2 Optical properties comparison between SOD and AOD from MERRA-2

Following the assessment of burned area estimates, the results for the optical properties of the smoke plume are presented and discussed, starting with a comparison between simulated SOD and MERRA-2 AOD.

Understanding the spectral behaviour of smoke aerosol optical properties is essential for interpreting optical depth measurements. In this context, both the simulated SOD at 550 nm and the MERRA-2 AOD at the same wavelength represent the column-integrated attenuation of solar radiation due to the presence of aerosols in the atmosphere. However, there are conceptual differences that affect their comparison. SOD corresponds specifically to the fraction of AOD attributed to smoke particles generated by wildfires and biomass burning, while MERRA-2 AOD includes all aerosol types present in the atmosphere, such as mineral dust, sulfates, nitrates, sea salt, and soot.

When $SOD \leq AOD$, only a fraction of the total aerosol burden can be attributed to smoke. When $SOD \approx AOD$, the aerosol population is dominated by biomass-burning particles, as expected during intense fire activity with minimal influence from other sources. In contrast, situations where $SOD \ll AOD$ indicate that non-smoke aerosol types, such as mineral dust, industrial sulfate pollution, or marine aerosols (e.g., Saharan intrusions), contribute substantially to the observed optical depth.

These physical considerations provide the basis for interpreting the spatial correspondence between simulated SOD and MERRA-2 AOD, shown in Fig. 7.

Figure 7 presents the spatial distribution of SOD under the Baseline configuration, for both dry and wet conditions, compared with MERRA-2 AOD at 550 nm at 18:00 UTC on 15 October 2017, during the t_1 -fresh phase. Four fixed base classes between 0 and 4 (unitless) were defined for AOD, as this range is most representative of intense fire plumes.

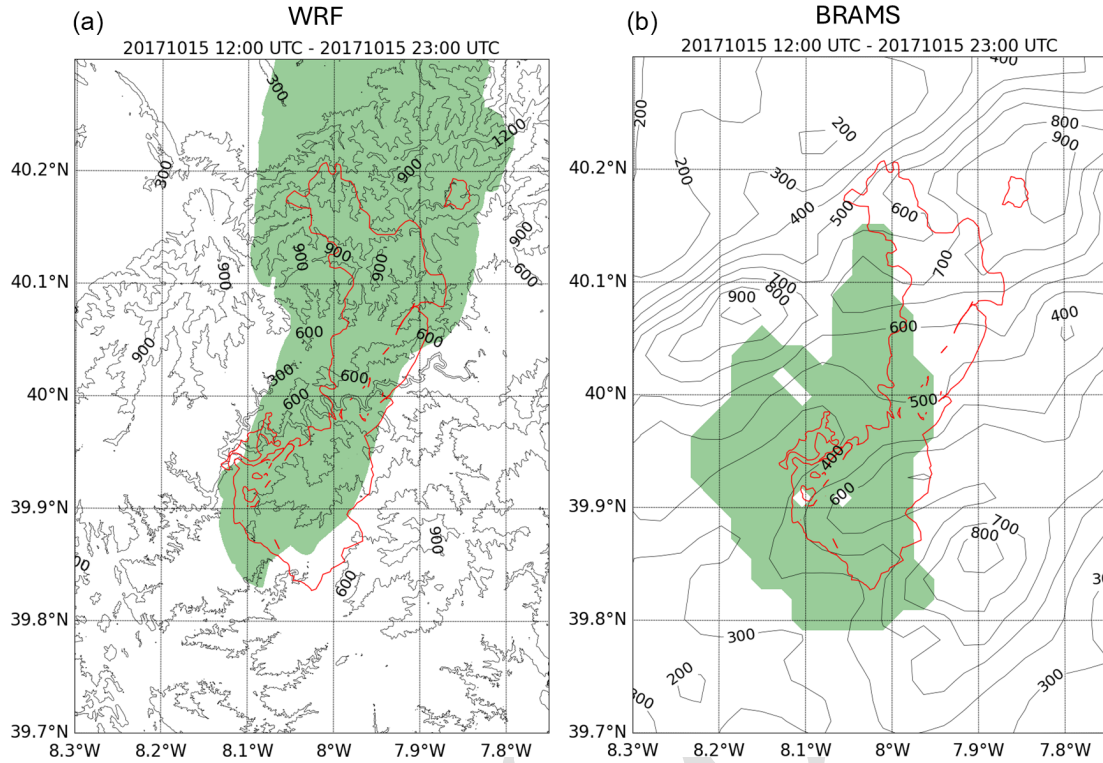


Figure 6. Comparison of simulated burned area over high-resolution topography from the (a) WRF-SFIRE and (b) BRAMS-SFIRE models for the wildfire event on 15 October 2017, accumulated between 12:00 and 23:00 UTC. Green-shaded regions represent the cumulative burned area, while red contours delineate the observed fire perimeter.

At this time, both SOD and AOD show a pronounced increase relative to earlier afternoon conditions, reflecting the intensification and vertical deepening of the smoke plume over central Portugal. The dry SOD contours highlight the plume core, whereas the wet SOD field extends further downwind and attains higher values, indicating enhanced optical thickness driven by hygroscopic growth under humid conditions. The overall spatial pattern compares well with MERRA-2 AOD, with the model capturing the main plume structure and gradients, albeit with a somewhat narrower extension compared to the reanalysis. These results reinforce the strong aerosol load and plume development characteristic of the t_1 -fresh phase. The highest SOD values fall within the expected range for intense wildfire plumes, although some amplification is likely due to plume retention within the limited model domain, which restricts northward dispersion.

Beyond the spatial structure at 18:00 UTC, the temporal evolution of SOD and AOD provides further insight into model–reanalysis consistency. In the Baseline configuration, the comparison between simulated SOD and MERRA-2 AOD from 13:00 to 17:00 UTC reveals a persistent mismatch in both magnitude and spatial organisation, despite the progressive strengthening of the modelled plume. At 13:00 UTC, SOD remains confined and weak, whereas MERRA-2 depicts a broader, already well-developed smoke

layer. This early underestimation reflects a timing offset, with the model delaying the onset of plume intensification relative to the reanalysis. From 14:00 to 16:00 UTC, both dry and wet SOD increase substantially, but the rate of increase is disproportionate relative to AOD. The simulated fields exhibit a much sharper spatial gradient and a narrower plume core, while MERRA-2 maintains a smoother, more diffused structure. This behaviour indicates that SOD responds primarily to the intense, locally concentrated core of the simulated plume, whereas MERRA-2 retains a broader regional aerosol contribution that is not present in BRAMS. Although an upwind background subtraction was applied to MERRA-2 AOD, it specifically removes only the inflow background and does not eliminate the wider regional AOD structure inherent to the reanalysis. As a result, MERRA-2 continues to exhibit a spatially smoother, regionally extensive optical depth, while SOD reflects only the fire-driven aerosol load. Consequently, the SOD–AOD relationship remains weakly constrained, with MERRA-2 showing elevated AOD even where SOD remains low or absent. By 17:00 UTC, SOD reaches its maximum values, particularly in the wet configuration, with magnitudes that fall within the physical range of dense wildfire smoke but exceed the AOD variability in the corresponding area. Part of this amplification is attributable to plume confinement within the limited model domain, which

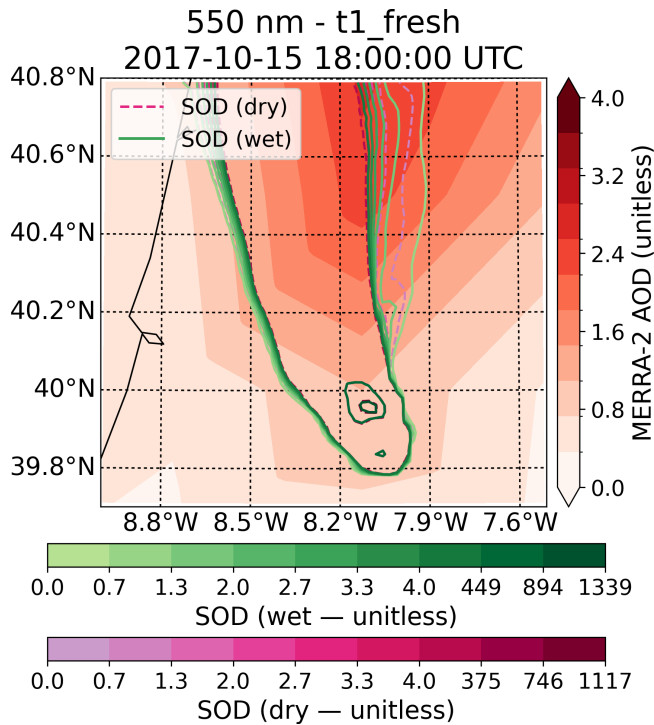


Figure 7. Spatial distribution of smoke optical depth (SOD) and MERRA-2 AOD (550 nm) over the study domain at 18:00 UTC on 15 October 2017, during the intense Sertão wildfire episode. AOD is shown as shaded colours; SOD (dry) and SOD (wet) are overlaid as dashed and solid contours, respectively.

prevents northward dispersion and leads to artificial accumulation. In contrast, MERRA-2 retains a more spatially extensive plume, reflecting long-range transport that the regional simulation cannot capture.

The very high SOD values, arising from the intense fuel burning confined to a subset of SFIRE grid cells, fall within the physical range of extreme wildfire plumes and accentuate the contrast with the smoother and lower AOD structure in MERRA-2. This discrepancy further weakens the SOD–AOD correspondence at this stage of the plume evolution. Part of the discrepancies between SOD and AOD across the domain arise from temporal offsets, differences in plume confinement, and the distinct spatial scales represented by the model and the reanalysis, which collectively limit their correspondence during the plume’s evolution.

Visualisation of the SOD–AOD scatter relationships (Fig. 8a–b) representing the Baseline optical configuration (test 1), provides insight into how the simulated plume evolves relative to the MERRA-2 reanalysis throughout the afternoon. Between 15:00 and 19:00 UTC, the statistical coupling between SOD (wet configuration) and MERRA-2 AOD improves, although substantial differences remain in their absolute magnitudes and spatial structure. At 15:00 UTC, the regression fit derived from the scatterplot (slope = 0.56, $R^2 = 0.03$) shows weak correspondence, primarily because

the AOD field retains a high regional background level (intercept ≈ 2.08) not represented by the localised smoke plume in BRAMS. By 19:00 UTC, the relationship strengthens somewhat (slope = 0.30, $R^2 = 0.36$), but a clear shift becomes apparent: the simulated SOD reaches much higher values than the MERRA-2 AOD across most of the range. This indicates that the model generates a more optically intense core of the plume, whereas MERRA-2 maintains a smoother and less concentrated aerosol structure. Hygroscopic growth in the wet configuration further amplifies the SOD, enhancing the optical depth relative to the reanalysis. The Conservative (test 2) and Lower Envelope (test 3) optical configurations exhibit regression behaviour very similar to the Baseline test, with only minor quantitative differences. At 15:00 UTC, both tests 2 and 3 display weak statistical coupling between SOD (wet) and MERRA-2 AOD, with slopes near 0.55, intercepts around 2.1, and negligible explained variance ($R^2 \approx 0.02$ – 0.03). These metrics indicate that, as in the baseline case, MERRA-2 retains a substantial background AOD contribution that is not represented by the simulated plume, and that early-phase SOD variability accounts for only a small fraction of the observed optical depth. By 19:00 UTC, the coupling strengthens in both configurations: slopes decrease to roughly 0.29–0.30, intercepts fall to ~ 0.65 (as in test 1), and R^2 increases to 0.35–0.36. This convergence across the three tests demonstrates that modifying κ , $r_{g,dry}$, or narrowing σ_g leads to only modest changes in the regression behaviour. The similarity of the results confirms that the optical response is relatively insensitive to plausible microphysical perturbations within the tested parameter space.

Table 4 provides a time-resolved evaluation of the statistical relationship between SOD and AOD during the Sertão wildfire period, highlighting the contrasting behaviour of the fresh and mixed phases. During the fresh phase (13:00–18:00 UTC), both dry and wet SOD differ markedly from the MERRA-2 AOD. Across 13:00–17:00 UTC, AOD remains relatively stable (Mean AOD ≈ 0.9 – 1.7) [TS2](#), whereas SOD increases sharply, especially in the wet configuration, rising from values near zero at 13:00 UTC to about 7 (Mean SOD ≈ 6 – 7) by 17:00 UTC. This produces a transition in the bias defined as SOD – AOD from strongly negative (-1.9 to -0.9) to strongly positive ($+5$ to $+6$). Correspondingly, MAE and RMSE increase substantially, and correlations remain extremely low ($r \approx 0.02$ – 0.06 , $R^2 \approx 0.00$), indicating that SOD explains virtually none of the spatial variability present in the AOD field. Physically, this reflects limited spatial covariance between the developing, highly localised simulated plume and the smoother regional aerosol structure represented by MERRA-2.

From 19:00 UTC onward, the plume enters the mixed phase (19:00–23:00 UTC), during which SOD intensifies dramatically, reaching [TS3](#) Mean SOD values between 35 and 65, while AOD remains nearly constant around 0.8–0.9. This leads to very large positive biases and correspondingly large error metrics. Linear correlations improve modestly (up to

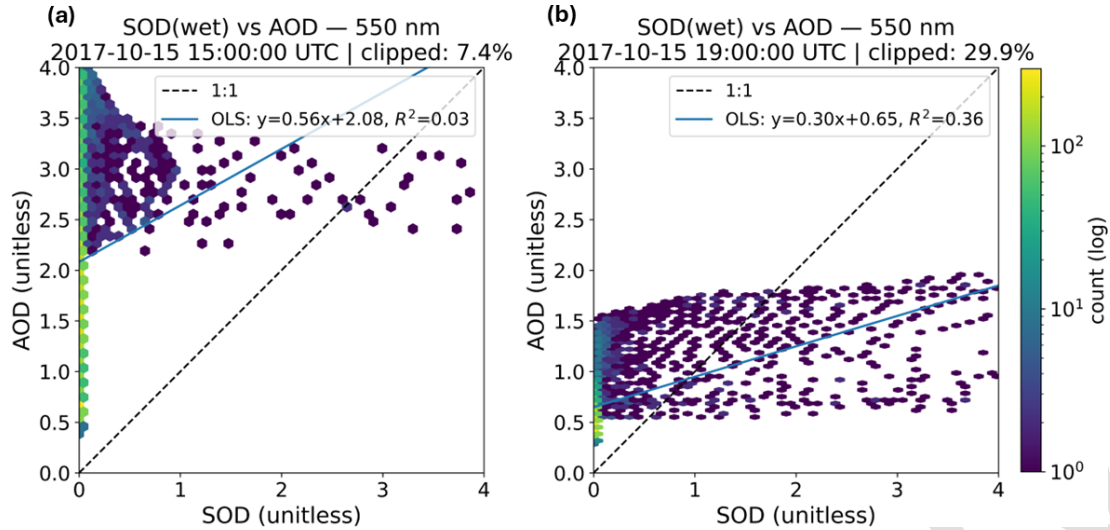


Figure 8. Scatter density plots comparing simulated SOD (wet) and MERRA-2 AOD at 550 nm for 15:00 UTC (a) and 19:00 UTC (b) on 15 October 2017. The dashed line represents the 1 : 1 relationship, and the solid line the ordinary least-squares (OLS) regression. Color shading denotes the logarithmic count of grid-point pairs. The clipped percentage indicates the fraction of points excluded from the plot due to exceeding the displayed SOD/AOD range (≥ 4.0).

$r \approx 0.58$), and R^2 increases to at most 0.34, indicating a partial but still limited recovery of spatial coherence between SOD and AOD. These diagnostics are consistent with progressive plume confinement and accumulation within the regional domain, yielding SOD magnitudes far exceeding the column aerosol load represented in MERRA-2.

Taken together, the hourly statistics confirm that part of the discrepancy between SOD and AOD arises from temporal offsets, plume confinement, and the fundamentally different spatial scales resolved by the model and the reanalysis. These structural differences limit the correspondence between the two datasets throughout the plume evolution.

Supplement Tables S1–S3 extend the SOD–AOD evaluation by quantifying how the Baseline, Conservative, and Lower Envelope microphysical configurations affect the model–reanalysis agreement during the mixed phase. Across all configurations, the results are highly consistent: mean SOD is one to two orders of magnitude larger than the corresponding MERRA-2 AOD (e.g., SOD ≈ 18 –30 for the ALL mask, increasing to 90–200 for the P70–P90 masks, while AOD remains near 1). Consequently, bias values (SOD – AOD) are strongly positive and increase with the percentile mask (e.g., +16 to +30 for ALL, rising to +180–200 for P90). MAE and RMSE follow the same pattern, reaching 80–110 for the ALL mask and 250–345 for P90. These statistics indicate that the simulated smoke column burden greatly exceeds the column optical depth represented by MERRA-2, regardless of the assumed microphysical configuration.

Background subtraction affects only the reanalysis field, reducing AOD by approximately 0.6 (1.17 to 0.57). As a result, bias becomes slightly larger, but MAE and RMSE change only marginally. Correlation coefficients remain ex-

tremely weak for the ALL mask ($r \approx 0.00$ –0.06; $R^2 \approx 0.00$), demonstrating that the discrepancies are not due to a removable background offset but rather reflect fundamental structural mismatches in spatial representativeness between SOD and AOD.

The percentile masks (P70–P90) highlight a systematic deterioration in skill as increasingly high-AOD grid cells are selected. Bias rises to +180–200, RMSE exceeds 300, and correlations become increasingly negative ($r \approx -0.30$ to -0.50), while R^2 remains ≤ 0.24 . This behaviour indicates that the regions of strongest AOD in MERRA-2 correspond to aerosol components and vertical layers not represented by SOD, including smoothed background mass, coarse-mode contributions, and long-range transported aerosol that the regional plume simulation cannot reproduce. The regression slopes remain near zero ($|\text{slope}| < 0.002$), confirming that variations in SOD magnitude have essentially no explanatory power for the spatial variability of AOD.

Differences across the microphysical perturbations (ABSORBING, WIDE_SIGMA, SMALL_RG, LARGE_RG) are minor, typically altering correlation by ≤ 0.05 and MAE/RMSE by ≤ 2 –5 %. Similarly, the near-identical results across the three microphysical frameworks (BASE, CONSERVATIVE, LOWER ENVELOPE) demonstrate that reasonable adjustments to κ , $r_{g,dry}$, and σ_g have only a secondary effect on the SOD–AOD comparison. The dominant source of discrepancy therefore lies not in microphysics, but in the excess plume mass and the spatial confinement of the smoke plume in the model domain relative to the broad, regionally smoothed optical depth represented in MERRA-2.

The statistical findings can be interpreted considering several physical and representativeness factors that fun-

Table 4. Diagnostic statistics for the Sertão wildfire period, including the mean, bias, mean absolute error (MAE), root-mean-square error (RMSE), Pearson correlation coefficient (r) and Spearman’s rank correlation coefficient (ρ), and coefficient of determination (R^2) of SOD and AOD.

Time (UTC)	Phase	Mean SOD	Mean AOD	Bias (SOD-AOD)	MAE	RMSE	r	ρ	R^2
13:00	Fresh–dry	0.00	0.94	−0.94	0.94	0.98	0.03	0.38	0.00
14:00	fresh–dry	0.03	1.73	−1.71	1.72	1.86	0.05	0.72	0.00
15:00	fresh–dry	0.31	2.24	−1.93	2.36	3.17	0.06	0.84	0.00
16:00	fresh–dry	1.83	1.36	0.47	2.77	10.97	0.02	0.84	0.00
17:00	fresh–dry	6.37	1.29	5.08	6.81	30.94	0.05	0.86	0.00
13:00	Fresh–wet	0.00	0.94	−0.94	0.94	0.98	0.02	0.38	0.00
14:00	fresh–wet	0.03	1.73	−1.70	1.72	1.86	0.05	0.72	0.00
15:00	fresh–wet	0.34	2.24	−1.90	2.39	3.35	0.06	0.84	0.00
16:00	fresh–wet	2.10	1.36	0.73	3.02	12.67	0.02	0.84	0.00
17:00	fresh–wet	7.42	1.29	6.13	7.83	36.51	0.05	0.86	0.00
18:00	fresh–wet	17.76	1.09	16.67	17.82	71.19	0.08	0.85	0.01
19:00	mixed–wet	35.35	0.89	34.47	35.23	115.34	0.14	0.83	0.02
20:00	mixed–wet	51.57	0.80	50.77	51.41	143.19	0.32	0.86	0.10
21:00	mixed–wet	62.62	0.83	61.79	62.41	159.82	0.50	0.91	0.25
22:00	mixed–wet	64.58	0.86	63.71	64.36	159.48	0.58	0.93	0.34
23:00	mixed–wet	58.29	0.89	57.39	58.10	142.47	0.58	0.92	0.34

damentally limit the correspondence between SOD and MERRA-2 AOD. Physically, the persistent decoupling between these variables reflects fundamental representativeness differences between the instantaneous fine-mode SOD fields produced at 2 km resolution and the hourly, 50–70 km column-integrated AOD from MERRA-2. SOD primarily reflects the fire-emitted smoke plume resolved by the regional model, whereas AOD also includes coarse-mode background aerosols and vertically extended layers. These structural differences explain the very low covariance and consistently large intercepts. Additional phase shifts arise from temporal mismatch between instantaneous model outputs and the assimilation-centred AOD, as well as plume-scale variability that is difficult for a coarse reanalysis to reproduce. Taken together, Tables S1–S3 show that BRAMS–SFIRE strongly overestimates SOD magnitude relative to MERRA-2 AOD, while underrepresenting the broader, regionally distributed optical-depth structure seen in the reanalysis. This behaviour reflects a plume that is too concentrated and optically intense locally, but less spatially extensive than the smoothed regional aerosol field in MERRA-2. A primary contributor to this mismatch is the contrast in spatial and temporal resolution between the high-resolution model output and the coarse MERRA-2 reanalysis. The BRAMS–SFIRE runs at 2 km horizontal resolution and produces instantaneous outputs, whereas MERRA-2 provides $\sim 0.5^\circ \times 0.625^\circ$ ($\sim 50 \times 70$ km) hourly means centred near hh:30. As a result, sharp smoke gradients and localized peaks captured by the model are heavily smoothed in MERRA-2, attenuating peak AOD values and shifting their apparent timing relative to the simulated plume. The smoothing also blends smoke

with background aerosols, reducing the spatial contrast between plume and non-plume regions.

Differences in aerosol composition further amplify this representativeness gap between the model and the reanalysis. The SOD evaluated here is derived from fine-mode $\text{PM}_{2.5}$ (fresh smoke), while MERRA-2 AOD represents total extinction, integrating coarse-mode dust and sea salt. In regions where coarse-mode aerosols are abundant, total AOD can diverge from, or even anticorrelate with, fine-mode SOD in both space and time. This compositional difference is consistent with elevated regression intercepts, i.e., a background optical load not associated with the fire plume.

Additional discrepancies arise from the way MERRA-2 assimilates observational AOD and represents rapidly evolving wildfire plumes. MERRA-2 assimilates satellite AOD observations (e.g., MODIS, VIIRS), subject to retrieval/sampling constraints; its smoke fields depend on emission inventories and the analysis cycle. Rapid, pyro-convective injections from intense wildfires, characterized by sub-hourly variability and strong vertical transport, are difficult to capture in reanalysis products. This can produce phase shifts in both timing and vertical structure relative to the model, especially during the most active burning period (13:00–17:00 UTC).

Humidity-driven growth constitutes another factor influencing the magnitude and spatial alignment of extinction between the model and MERRA-2. The wet SOD uses modelled RH to allow growth in particle size and extinction efficiency. MERRA-2 may employ coarser meteorology and simplified κ parameterizations. Discrepancies in RH and κ directly affect the scattering enhancement and extinction efficiency, contributing to systematic differences in optical depth

amplitude. The better agreement obtained under wet conditions supports the physical importance of this process.

Temporal pairing between the model and the reanalysis also introduces structural differences, especially during rapid plume evolution. The comparison pairs instantaneous model fields at $H:00$ with MERRA-2 hourly means representing roughly $[H - 30, H + 30 \text{ min}]$. During periods of rapid-fire intensification or plume advection, this temporal mismatch further smooths and delays AOD peaks relative to modelled SOD maxima, manifesting as the apparent decoupling observed in the early afternoon hours.

Some of the discrepancy may also stem from simplifying assumptions in the optical calculations applied to the BRAMS-SFIRE output. The Mie-based SOD assumes spherical, monodisperse particles with fixed effective radius and density. [TS4](#) Under extreme fire conditions, this simplification tends to overrepresent the number of small particles per unit mass, enhancing extinction near the fire front. This effect increases simulated SOD peaks but has a minor influence on broader plume statistics, as confirmed by the microphysical sensitivity tests.

The optical diagnostics quantified shortwave extinction, whereas wildfires emit intense longwave radiation that alters buoyancy and turbulence, promoting lofting and secondary aerosol formation. Such small-scale feedbacks are not explicitly resolved in MERRA-2, yet they modulate plume height and density and thus the spatial alignment of SOD and assimilated AOD.

3.3 Linking Aerosol Mass, Optical Properties, and Radiative Effects in the Smoke Plume

The optical diagnostics presented in Sect. 3.2 revealed substantial differences between simulated SOD and MERRA-2 AOD, particularly during the early stages of plume development. To understand these discrepancies, it is necessary to examine how the mass distribution and composition of the smoke plume relate to its optical properties and radiative behaviour.

This section, therefore, shifts the focus from column-integrated optical depth to the underlying aerosol mass fields, $\text{PM}_{2.5}$, black carbon (BC), and organic carbon (OC), and investigates how their spatial structure governs the extinction properties diagnosed in the previous section. Because wildfire smoke is dominated by carbonaceous aerosols with distinct emission pathways and optical roles, analysing their spatial patterns provides essential physical context for interpreting SOD–AOD differences.

While SOD explicitly quantifies shortwave extinction at 550 nm, the radiative environment of the plume is simultaneously influenced by longwave emission from the fire, which enhances buoyancy, contributes to plume-rise, and facilitates the formation of secondary aerosols. Although longwave processes do not enter the SOD calculation directly, they modify the thermodynamic structure of the plume and

thus affect the dispersion and vertical redistribution of the carbonaceous particles that control shortwave extinction. In this sense, longwave heating indirectly influences the spatial and vertical distribution of scattering and absorbing aerosols.

Figure 9 shows the spatial distribution of column-averaged $\text{PM}_{2.5}$ concentration and the corresponding MERRA-2 surface BC and surface OC mass concentrations at 19:00 UTC, during the mixed phase when the plume becomes more coherent. The clear spatial coherence between $\text{PM}_{2.5}$ and the carbonaceous species is consistent with a dominant carbonaceous contribution to the simulated fine-mode mass associated with biomass burning. As typically observed in wildfire plumes, OC dominates BC by roughly an order of magnitude, consistent with smouldering/mixed-combustion conditions that generate large amounts of semi-volatile organic compounds which rapidly condense into fine-mode particles. BC remains confined to a narrower core associated with flaming combustion, while OC extends farther downwind, forming a broader envelope around the $\text{PM}_{2.5}$ plume. This contrast reflects the two-source nature of carbonaceous smoke: BC forms primarily under high-temperature, oxygen-limited flaming conditions, while OC arises from lower-temperature pyrolysis and subsequent condensation processes that disperse more broadly downwind. This structural contrast, narrow BC ridge, broad OC plume, is clearly captured at 2 km model resolution but becomes smoothed at the MERRA-2 grid spacing ($\sim 50\text{--}70 \text{ km}$). Such smoothing dilutes gradients and contributes to the weaker early-phase agreement between SOD and AOD noted in Sect. 3.2. By 19:00 UTC, however, the plume's organisation improves and the spatial correspondence among $\text{PM}_{2.5}$, BC, and OC becomes more coherent, aligning with the improved SOD–AOD coupling reported for the mixed phase.

To further connect aerosol mass with optical extinction, Fig. 10 compares the simulated SOD with the MERRA-2 BC and OC extinction AOD fields at 550 nm for 18:00 UTC. The spatial patterns reaffirm the behaviour already identified in Fig. 9: BC extinction remains weak and confined to a narrow region near the fire core, whereas OC extinction extends over a much broader downwind area, mirroring the wider $\text{PM}_{2.5}$ and OC mass envelope characteristic of smouldering and mixed-combustion emissions.

The simulated SOD field shows a much stronger spatial correspondence with OC extinction than with BC, confirming that OC is the dominant contributor to shortwave extinction at 550 nm in this plume. This is physically expected, as 550 nm is strongly sensitive to fine-mode scattering aerosols, and OC constitutes the bulk of the fine carbonaceous mass. In contrast, BC, although strongly absorbing, represents only a small fraction of the total aerosol mass and thus contributes minimally to visible-band extinction.

Some spatial mismatches remain, primarily due to the coarse horizontal resolution of MERRA-2 (50–70 km), which smooths gradients that the 2 km BRAMS–SFIRE simulation resolves sharply. This smoothing reduces peak ex-

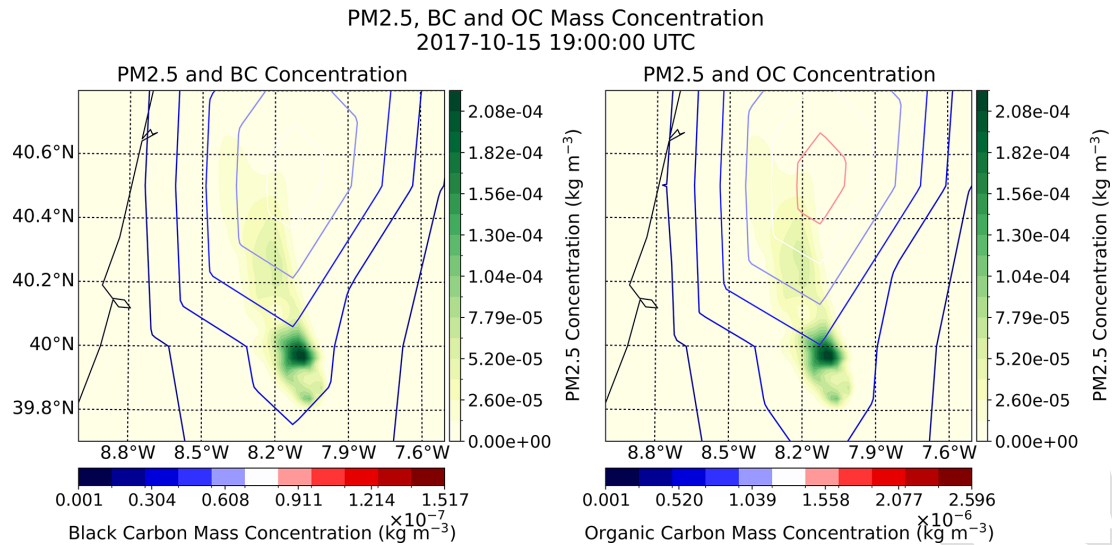


Figure 9. Spatial distribution of column-averaged $\text{PM}_{2.5}$ concentration (kg m^{-3} , contours) on MERRA-2 surface BC (left panel) and OC (right panel) mass concentrations (kg m^{-3} , colour shading) at 19:00 UTC on 15 October 2017.

tion values in the reanalysis and broadens plume boundaries, producing slight offsets between SOD maxima and the corresponding features in the MERRA-2 extinction fields.

Figure 11 provides a quantitative assessment of how SOD relates to the carbonaceous extinction components of MERRA-2 during the mixed phase (19:00 UTC, 550 nm). Approximately 10 % of the data lie outside the plotting limits, but this level of clipping does not affect the statistical interpretation.

In panel (a), which compares SOD with BC extinction AOD, the ordinary-least-squares (OLS) fit shows a very small slope (≈ 0.06), a small positive intercept (≈ 0.03), and a modest coefficient of determination ($R^2 \approx 0.28$). These values indicate that only a limited fraction of the spatial variability in BC extinction is explained by SOD. This weak coupling is physically consistent with BC representing only a minor fraction of the total carbonaceous mass at this stage and with the coarse ~ 50 – 70 km MERRA-2 grid smoothing the sharp BC gradients resolved by the 2 km model. The horizontally elongated scatter distribution relative to the 1 : 1 line further highlights this weak covariance and the strong representativeness differences between the two datasets.

In panel (b), the comparison between SOD and OC extinction AOD yields a substantially stronger statistical relationship. The regression slope (≈ 0.38) is roughly six times larger than for BC, the intercept is higher (≈ 0.16), and the coefficient of determination increases to $R^2 \approx 0.31$. These values reflect the dominant contribution of OC to smoke extinction at 550 nm and the closer correspondence between SOD patterns and the spatial structure of OC in MERRA-2. The slight flattening of the scatter at large SOD values likely results from the coarse resolution of the reanalysis, the limited dynamic range of the OC extinction field, and differences in hu-

midification growth or mixing-state assumptions between the model's κ -Köhler/Mie closure and the GOCART/MERRA-2 framework. Taken together, these results confirm that OC extinction retains a much clearer imprint of the plume diagnosed by SOD than BC extinction, consistent with OC dominating visible-band extinction in biomass-burning smoke. The positive intercepts in both relationships indicate a persistent background extinction component present even where plume–model covariance is strong. No additional attribution (e.g., combustion phase variability or cloud effects) can be inferred from these diagnostics alone without independent observational constraints.

To extend the analysis beyond the scatter relationships in Figs. 10–11, Table 5 provides domain-wide statistical metrics for black carbon (BC) and organic carbon (OC) extinction under all microphysical configurations, quantifying bias, variance explained, and sensitivity to microphysical perturbations. These diagnostics reinforce the contrasting behaviour already identified in the spatial and scatter comparisons: while OC extinction exhibits a coherent and physically interpretable relationship with SOD, BC extinction remains only weakly coupled to the modelled smoke field. For BC, all microphysical configurations (Baseline, Conservative, Lower Envelope) produce nearly identical metrics, demonstrating that the SOD–BC relationship is largely insensitive to perturbations in κ , $r_{g,dry}$, or σ_g . Mean SOD values range from 7.6–8.6, overwhelmingly exceeding the corresponding MERRA-2 BC extinction (≈ 0.06), yielding very large positive biases (7.5–8.5) and RMSE values between 52–58. These large errors are expected: BC represents only a minor fraction of carbonaceous aerosol mass in biomass-burning plumes and contributes weakly to visible-band extinction at 550 nm. Correlation coefficients remain low but

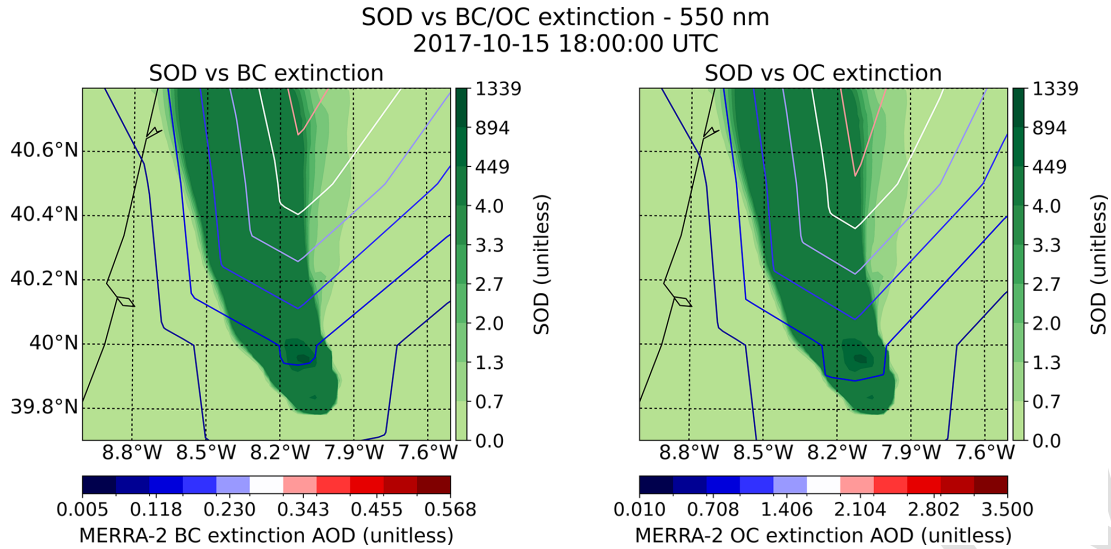


Figure 10. Comparison between simulated SOD (contours) and MERRA-2 extinction AOD at 550 nm for BC (left panel) and OC (right panel), at 18:00 UTC on 15 October 2017.

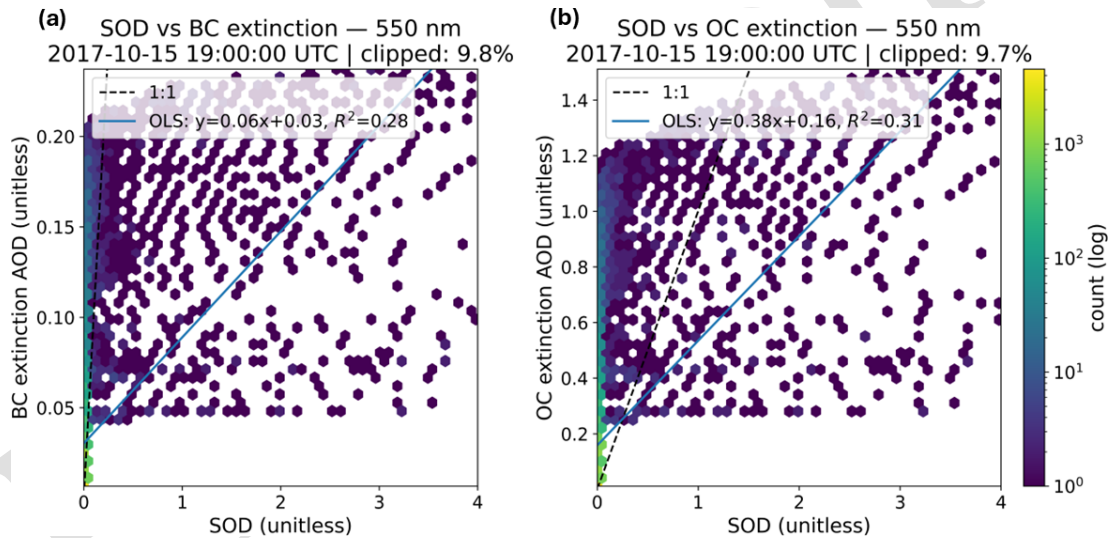


Figure 11. Scatter density plots comparing simulated SOD (wet) with MERRA-2 component extinction AOD for BC (a) and OC (b) at 550 nm, for 19:00 UTC on 15 October 2017. The dashed line represents the 1:1 relationship, and the solid line the ordinary least-squares (OLS) regression. Colour shading denotes the logarithmic density of grid-point pairs. The clipped percentage indicates the fraction of points excluded from the plot because their SOD or AOD values exceeded the displayed range (≥ 4.0).

positive (Pearson $r \approx 0.14$; Spearman $\rho \approx 0.75$), indicating that although BC extinction contains a monotonic spatial ordering relative to SOD, it explains only about 2 % of the SOD variance ($R^2 = 0.02$). The regression slopes for BC (≈ 0.000) confirm that spatial variability in BC extinction barely responds to changes in SOD, while the small intercept (~ 0.058) is consistent with a persistent background BC extinction present in the reanalysis, likely representing non-smoke contributions and the coarse effective resolution of MERRA-2.

In contrast, the OC extinction field shows a stronger and more physically meaningful connection to SOD. Although mean SOD (≈ 7.6 – 8.6) still greatly exceeds mean OC extinction (≈ 0.34), the bias is smaller than for BC, and the correlations are modestly higher ($r \approx 0.16$; $\rho \approx 0.75$). The OC regression slopes (0.001–0.002), while still small in absolute terms, are one order of magnitude larger than those obtained for BC **TSS** mirroring OC's dominant contribution to carbonaceous aerosol mass and its stronger role in visible-band scattering. The regression intercepts (~ 0.325) indicate a substantial baseline OC extinction in MERRA-2, consistent

with the presence of regionally distributed secondary organic aerosols and with the smoothing inherent to the coarse-grid reanalysis. As with BC, the near-identical statistics across the three microphysical experiments reflect that microphysical uncertainties play only a secondary role in controlling the SOD–OC relationship. Overall, the diagnostics confirm that OC dominates the optical signature of the plume at 550 nm, acting as the principal contributor to scattering and thus to the radiative impact of the smoke layer, while BC contributes a much smaller, spatially confined absorbing component.

The weak sensitivity of the statistical metrics to the microphysical perturbations further demonstrates that the observed behaviour is governed primarily by species composition and representativeness differences between BRAMS–SFIRE and MERRA-2, rather than by uncertainties in aerosol size distribution or hygroscopic growth.

Beyond extinction behaviour, the single-scattering albedo (SSA) offers a complementary measure of the radiative character of the smoke plume by expressing the relative contributions of scattering and absorption. Accordingly, SSA fields derived from BRAMS–SFIRE were compared with their MERRA-2 counterparts to assess whether the model correctly captures the scattering–absorption balance within the plume.

Figure 12 contrasts the simulated SSA at 550 nm with two MERRA-2 products at 19:00 UTC: a BC+OC proxy (left panel) and the total-aerosol SSA (right panel). SSA represents the ratio of scattering to total extinction; hence low SSA values correspond to strongly absorbing aerosol (typically BC-rich fresh smoke), while high SSA indicates more scattering-dominated mixtures such as aged organics or background sulphates.

In the BC+OC comparison (Fig. 12, left), BRAMS–SFIRE yields SSA values mostly between 0.88 and 0.90, forming smooth horizontal gradients across the plume. This behaviour is consistent with moderately scattering aerosols and limited absorption. The corresponding MERRA-2 BC+OC proxy, however, exhibits sharper gradients and pockets of markedly lower SSA (< 0.82) near the fire core, reflecting stronger BC absorption in the reanalysis than in the model. These contrasts partly arise from MERRA-2’s coarse grid (~ 50 – 70 km), which simultaneously smooths plume edges and preserves mesoscale absorption signatures.

The right panel compares simulated SSA against total MERRA-2 SSA, which includes additional scattering species (sulphates, dust, sea salt). This total-aerosol SSA is higher and more horizontally uniform than the BC+OC proxy, reflecting the dominant contribution of non-carbonaceous scattering aerosols in the reanalysis. Their inclusion brings MERRA-2 SSA closer to the scattering-dominated regime simulated by BRAMS–SFIRE, though spatial differences remain due to the finer plume structure resolved by the 2 km model.

The discrepancies highlighted in Fig. 12 arise from several structural factors: (i) dilution and enhanced mixing in

BRAMS–SFIRE, which reduce the local BC mass fraction and therefore increase the SSA (i.e., shift the aerosol population toward more scattering-dominated conditions); (ii) coarse spatial averaging in MERRA-2, which smooths sub-grid gradients but retains regional absorption patterns; and (iii) fundamentally different mixing-state assumptions. In this study, SSA is computed offline from $PM_{2.5}$ using a monodisperse, externally mixed Mie scheme, [TS6](#) which does not account for absorption enhancement arising from internally mixed BC encapsulated within organic or sulphate material. By contrast, GOCART/MERRA-2 treats fine-mode aerosols as internally mixed, allowing lensing effects that increase BC absorption.

Consequently, this monodisperse $PM_{2.5}$ aerosol representation [TS7](#) tends to overestimate SSA relative to MERRA-2 in the vicinity of the plume core. Because the $PM_{2.5}$ -based optical calculation adopts fixed microphysical parameters within each phase scenario, the resulting SSA exhibits limited spatial variability, even across regions with strong concentration gradients.

To complement the spatial fields, Fig. 13 presents scatter-density comparisons between simulated SSA and MERRA-2 SSA for BC+OC (panel a) and total aerosols (panel b). In both cases, the relationships exhibit weak covariance and low explanatory power ($R^2 \leq 0.15$). The simulated SSA spans a narrow dynamic range, whereas MERRA-2 displays substantially larger spatial variability, particularly for the BC+OC proxy. This contrast leads to limited point-wise correspondence between datasets. Although the total-aerosol comparison shows slightly closer absolute values, correlations remain weak, reflecting structural differences in aerosol representation and mixing-state assumptions.

Taken together, Figs. 12–13 indicate that BRAMS–SFIRE captures the plume’s spatial extent and its predominantly scattering-dominated character, consistent with the OC-rich composition shown in Figs. 9–11, yet it underrepresents the absorbing component associated with fresh BC. The persistence of SSA biases across all microphysical configurations further demonstrates that these discrepancies are structural, arising from resolution limitations, mixing-state assumptions, and representativeness differences rather than from uncertainties in aerosol microphysics.

Table 6 quantifies the SSA behaviour for both the BC+OC and total-aerosol configurations and confirms the spatial patterns identified in Figs. 12–13. When compared against the MERRA-2 BC+OC SSA proxy, the model exhibits a large positive bias of ~ 0.36 – 0.37 , consistent across the Baseline, Conservative, and Lower Envelope configurations. This bias reflects a systematic overestimation of scattering in the simulated plume: the mean model SSA is ~ 0.90 , whereas the BC+OC SSA in MERRA-2 is only ~ 0.54 (“Mean simu” and “Mean MERRA-2”). These values corroborate Fig. 12, where BRAMS–SFIRE produces a more scattering-dominated (optically brighter, less absorbing) plume than the reanalysis.

Table 5. Diagnostic statistics for the full Sertão wildfire period, including the mean, bias, mean absolute error (MAE), root-mean-square error (RMSE), Pearson correlation coefficient (r) and Spearman’s rank correlation coefficient (ρ), and coefficient of determination (R^2), linear-regression slope and intercepts between SOD and BC, OC MERRA-2 extinction AOD.

Carbonaceous aerosols	Phase	Mean SOD	Mean BC/OC	Bias	MAE	RMSE	r	ρ	R^2	slope	intercept
BC	Baseline	7.92	0.06	7.86	7.95	53.73	0.14	0.75	0.02	0.000	0.058
	Conservative	8.58	0.06	8.52	8.61	58.49	0.14	0.75	0.02	0.000	0.058
	Lower Envelope	7.62	0.06	7.56	7.65	52.00	0.14	0.75	0.02	0.000	0.058
OC	Baseline	7.92	0.34	7.58	8.09	53.62	0.16	0.75	0.03	0.001	0.325
	Conservative	8.58	0.34	8.24	8.75	58.38	0.16	0.75	0.03	0.001	0.325
	Lower Envelope	7.62	0.34	7.29	7.80	51.90	0.16	0.75	0.03	0.002	0.325

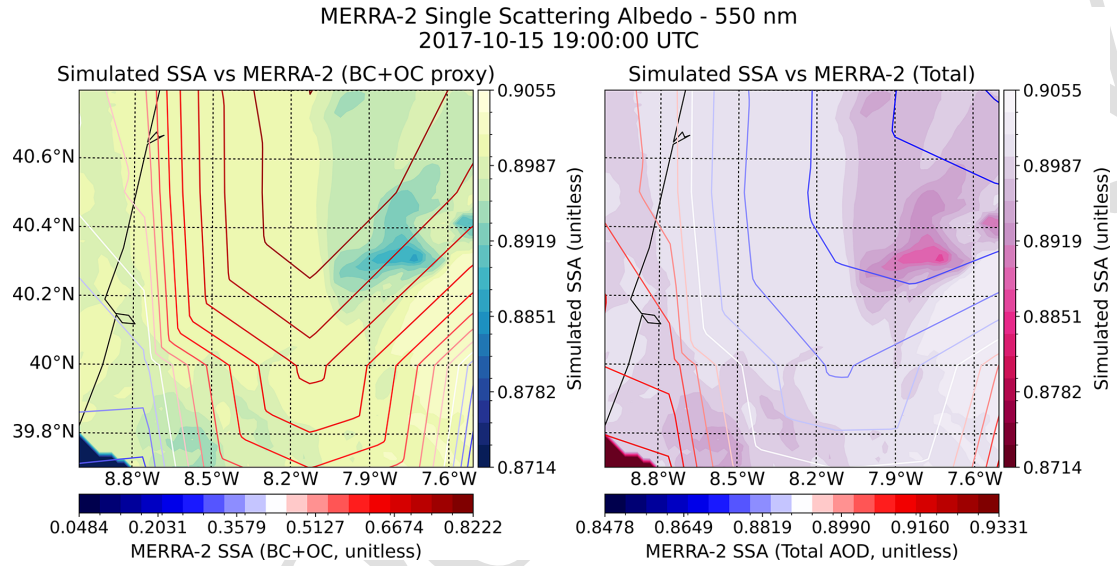


Figure 12. Spatial distribution of SSA at 550 nm derived from BRAMS-SFIRE $\text{PM}_{2.5}$ simulations, overlaid with SSA contours derived from MERRA-2 reanalysis for the wildfire plume on 15 October 2017, at 19:00 UTC. Left panels show MERRA-2 SSA calculated from BC and OC AOD, while right panels represent SSA derived from total AOD (all species).

The correlations remain weak, Pearson r ranges from -0.42 to 0.24 , and Spearman ρ from -0.27 to 0.29 , indicating little pointwise correspondence between model and reanalysis fields. The OLS slopes are extremely small (≈ 0.06 , -0.18 , -0.17 depending on configuration), and the intercepts span large values (from about -12 to $+15$). These unphysical intercepts arise from the narrow dynamic range of SSA and should not be interpreted in mechanistic terms. [TS9](#)

In contrast, the comparison with MERRA-2 total-aerosol SSA yields a markedly better agreement. The bias nearly vanishes ($+0.01$) and both MAE and RMSE reduce to ~ 0.01 – 0.02 . Correlations increase to weak but positive values (Pearson $r \approx 0.35$ – 0.47 , Spearman $\rho \approx 0.32$ – 0.34). [TS10](#) This improvement results from the fact that total-aerosol SSA in MERRA-2 includes additional scattering species, notably sulphates, dust, and secondary organics, which raise the reanalysis SSA to values close to those in the model (0.89 – 0.90 , “Mean MERRA-2”). Thus, although BRAMS-SFIRE

overestimates SSA relative to carbonaceous-only extinction, its bulk radiative behaviour aligns more closely with the full multi-species aerosol environment represented in MERRA-2.

Overall, these results confirm that the simulated plume is dominated by moderately scattering, OC-rich smoke, while the absorbing BC component is underrepresented relative to the reanalysis. The near-identical SSA statistics across all microphysical experiments show that the discrepancies are structural rather than parametric, arising from simplifications in the optical treatment (e.g., monodisperse, externally mixed particles), the model–reanalysis resolution gap, and differences in mixing-state representation, rather than from uncertainties in κ , $r_{g,dry}$, or σ_g .

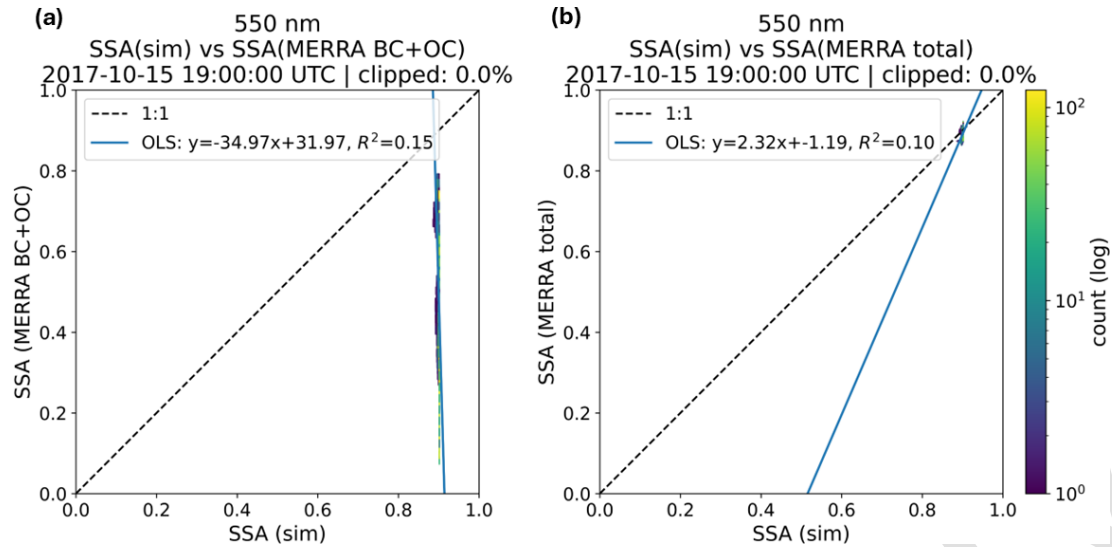


Figure 13. Scatter-density plots comparing single scattering albedo (SSA) derived from BRAMS–SFIRE $\text{PM}_{2.5}$ simulations (x-axis) with MERRA-2 SSA proxies at 550 nm for BC+OC (a) and total aerosols (b) at 19:00 UTC on 15 October 2017. The simulated SSA field is identical in both panels, as it is derived from the same $\text{PM}_{2.5}$ distribution and fixed microphysical assumptions; only the MERRA-2 reference field differs (BC+OC proxy versus total aerosol SSA). The dashed line denotes the 1 : 1 relationship, while the solid line represents the ordinary least-squares (OLS) regression fit. Colour shading indicates the logarithmic density of grid-point pairs. The clipped percentage denotes the fraction of data excluded for visualisation purposes because their SOD or AOD values exceed the displayed range (≥ 4.0). [TS8](#)

Table 6. Diagnostic statistics for all the Sertã wildfire period, including the mean, bias, mean absolute error (MAE), root-mean-square error (RMSE), Pearson correlation coefficient (r) and Spearman’s rank correlation coefficient (ρ), and coefficient of determination (R^2), linear-regression slope and intercepts between SSA derived from $\text{PM}_{2.5}$ simulated by BRAMS–SFIRE and SSA derived from MERRA-2 extinction AODs (BC+OC and total aerosol components).

Carbonaceous aerosols	Phase	Mean simu	Mean MERRA-2	Bias	MAE	RMSE	r	ρ	R^2	slope	intercept
SSA BC+OC	Baseline	0.90	0.54	0.37	0.37	0.42	0.24	0.29	0.06	14.14	−12.21
	Conservative	0.90	0.54	0.37	0.37	0.42	−0.42	−0.26	0.18	−15.63	14.63
	Lower Envelope	0.90	0.54	0.36	0.36	0.41	−0.41	−0.27	0.17	−11.17	10.55
SSA Total	Baseline	0.90	0.89	0.01	0.02	0.02	−0.35	−0.37	0.12	−1.88	2.58
	Conservative	0.90	0.89	0.01	0.02	0.02	0.47	0.34	0.22	1.57	−0.53
	Lower Envelope	0.90	0.89	0.01	0.02	0.02	0.47	0.34	0.22	1.16	−0.15

3.4 Temporal Evolution and Distribution of $\text{PM}_{2.5}$ Concentrations simulated

Figure 14 shows the frequency distributions of domain-wide near-surface $\text{PM}_{2.5}$ concentrations ($\mu\text{g m}^{-3}$) at 13:00, 16:00, 19:00, and 22:00 UTC on 15 October 2017. All panels use identical binning and a logarithmic y-axis to emphasize the occurrence of rare but extremely high concentrations. At every time step, the distributions are highly right-skewed: most grid cells fall within the lowest concentration bins, while a persistent heavy tail extends toward very large $\text{PM}_{2.5}$ values, characteristic of a spatially confined but optically and chemically intense smoke plume.

Between 13:00 and 16:00 UTC, the distributions broaden substantially. Although the mode remains anchored in the

lowest bin, indicating that the majority of the domain experiences only weak smoke influence, the gradual infilling of intermediate bins and the emergence of a long upper tail reflect the onset of plume intensification and expansion during the early afternoon. By 19:00 UTC, the histogram exhibits its widest dynamic range, with sustained occupancy across intermediate and high concentration classes and peak values approaching $107 \mu\text{g m}^{-3}$. This behaviour signals maximum plume loading near the surface, consistent with the period of strongest fire activity and turbulent mixing. By 22:00 UTC, the distribution narrows slightly: the extreme upper tail becomes less populated, suggesting partial dilution and reduced near-surface entrainment following the evening transition. Nevertheless, the heavy tail does not vanish, implying that localized pockets of very high $\text{PM}_{2.5}$ persist despite weaker

turbulence and declining emissions. Intermediate concentration bins retain notable counts, indicating that the plume continues to influence a non-negligible fraction of the domain even as the intensity of near-surface impacts diminishes.

From a physical standpoint, the coexistence of an overwhelmingly low-concentration mode with a pronounced heavy tail underscores the highly intermittent nature of smoke exposure: large portions of the domain remain only weakly affected, while a small number of grid cells experience extreme concentrations that dominate the regional burden. The afternoon broadening of the distributions reflects plume growth, lateral spread, and enhanced turbulent transport, whereas the partial evening contraction corresponds to stabilization and reduced mixing. Such behaviour highlights the operational relevance of intense, spatially localized hotspots, which evolve rapidly through the afternoon and can persist into the evening despite overall decreases in plume activity.

Whereas Fig. 14 documents the evolution of $\text{PM}_{2.5}$ distributions throughout the day, Fig. 15 isolates the histogram corresponding to 19:00 UTC on 15 October 2017, highlighting the structure of the heavy-tailed distribution at the hour of maximum plume loading. Figure 15 shows the domain-wide frequency distribution of simulated $\text{PM}_{2.5}$ concentrations at that time. The histogram reveals a pronouncedly right-skewed distribution, with the vast majority of grid cells occupying the lowest concentration bins, while a progressively smaller number populate the intermediate and upper ranges. The logarithmic vertical axis accentuates this structure: although extremely high $\text{PM}_{2.5}$ values occur infrequently; they form a distinct heavy tail that extends up to nearly $1 \times 10^7 \mu\text{g m}^{-3}$.

This statistical behavior reflects the intrinsic spatial heterogeneity of the plume. Most of the domain remains only weakly affected by smoke at this hour, whereas a limited set of grid cells, associated with the fire core and the most concentrated portions of the near-surface plume, exhibit exceptionally large $\text{PM}_{2.5}$ loadings. These extreme values are physically plausible in the context of intense wildfire activity, where strong pyroconvective injection, limited dilution, and local recirculation can sustain highly elevated concentrations.

The coexistence of a dominant low-concentration mode with a persistent heavy tail indicates a smoke field that is spatially sparse yet extremely intense where present, consistent with the plume morphology seen in the spatial plots. Consequently, domain-wide exposure at 19:00 UTC is governed disproportionately by a small fraction of high- $\text{PM}_{2.5}$ cells, underscoring the presence of sharp gradients and localized hotspots that play a central role in the air-quality and radiative impacts of the event.

While the model captures the broad spatial organisation and the characteristic heavy-tailed distribution of the plume, Figs. 14–15 show that a very small number of grid cells attain $\text{PM}_{2.5}$ and SOD values far exceeding those reported in ob-

servational studies. Surface and aircraft measurements in intense wildfire environments typically report maximum $\text{PM}_{2.5}$ concentrations of 10^3 – $10^4 \mu\text{g m}^{-3}$ (Gili et al., 2025; Landis et al., 2017), and even the highest shortwave AOD values observed by AERONET, FTIR, or aircraft seldom exceed 10–17.5 (Daniels et al., 2024; Eck et al., 2019; Frausto-Vicencio et al., 2023; Kassianov et al., 2025; Paton-Walsh et al., 2005; Shinozuka and Redemann, 2011). Concentrations in the 10^6 – $10^7 \mu\text{g m}^{-3}$ range or SOD magnitudes of several thousand therefore have no documented observational analogue.

Such extremes likely arise from the interaction between very sharp emission gradients near the fire front, unresolved sub-grid variability in fuel consumption, and the behaviour of numerical transport schemes under steep concentration contrasts. Large tracer spikes have been documented in models employing Semi-Lagrangian advection, particularly in some global forecasting systems (e.g., ECMWF-type models or other spectral NWP frameworks), where negative-value clipping and subsequent mass-adjustment procedures can generate artificial local extrema (Aranami et al., 2015; Bermejo and Conde, 2002; Sørensen et al., 2013; Zerroukat and Shipway, 2017). However, BRAMS–SFIRE does not use a classical Semi-Lagrangian transport scheme. The atmospheric dynamics are solved in an Eulerian framework derived from the RAMS core, while fire spread is computed using a level-set formulation. In this context, the extreme $\text{PM}_{2.5}$ values observed here could arise from the interaction between intense near-source emission gradients, grid-scale representation constraints, including the spatial mapping of vegetation and fuel types, and transport–emission coupling under steep concentration contrasts.

Although these outliers occupy only a very small fraction of the domain and do not significantly affect the large-scale optical diagnostics presented earlier, their presence indicates that further refinement is required in the representation of near-source smoke production and its numerical transport. The underlying causes of these extremes, linked to the parameterisation of fuel consumption, emission intensity, and the FRP formulation, are examined in detail in Sect. 3.6.

3.5 Atmospheric Stability and Thermodynamic Modulation by Aerosol–Radiation Interactions in Wildfire Events

This section examines how smoke–radiation interactions modulate atmospheric stability during the wildfire event, linking $\text{PM}_{2.5}$ loading, optical properties, and radiative forcing to changes in CAPE, CIN, and boundary-layer structure.

Atmospheric stability is primarily governed by the vertical temperature gradient or lapse rate. The behaviour of an air parcel depends on how rapidly it cools adiabatically compared to the ambient temperature profile. If a rising parcel cools at a rate lower than the environmental lapse rate, it becomes warmer and less dense than its surroundings, gaining positive buoyancy. Conversely, if it becomes denser than the

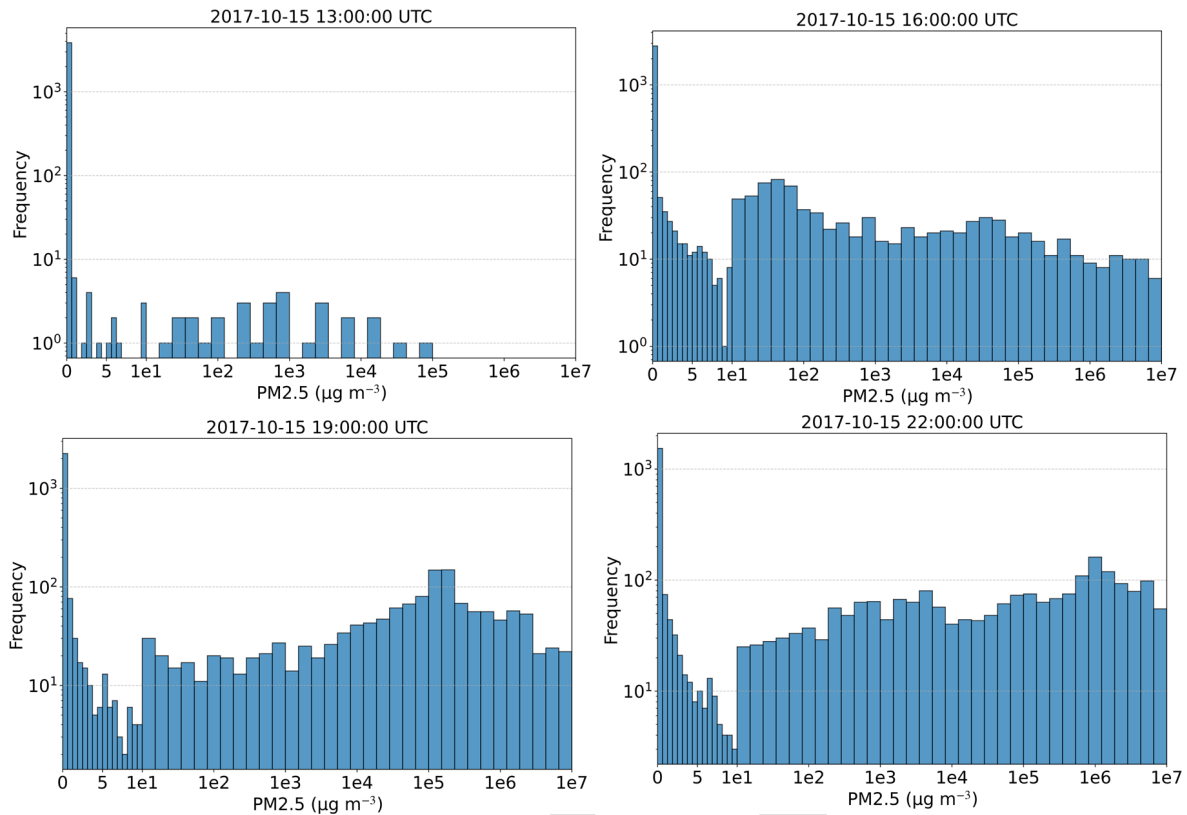


Figure 14. Frequency distribution of $\text{PM}_{2.5}$ concentrations ($\mu\text{g m}^{-3}$) across the simulation domain on 15 October 2017 at different hours (13:00, 16:00, 19:00 and 22:00 UTC). Each histogram shows the number of grid cells registering $\text{PM}_{2.5}$ values within each concentration bin. The vertical axis is plotted on a logarithmic scale to highlight rare but extreme values.

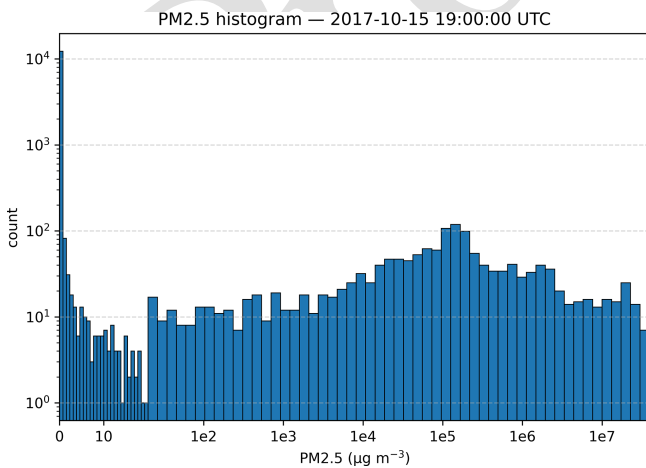


Figure 15. Histogram of $\text{PM}_{2.5}$ concentration ($\mu\text{g m}^{-3}$) across the simulation domain at 19:00 UTC on 15 October 2017.

surrounding air, it will descend. When vertical displacements of air parcels are amplified by buoyancy forces, the atmosphere is considered unstable, favouring convection, cloud formation, and potentially severe weather. In contrast, if the parcel is cooler and denser than its environment, vertical motion is suppressed, indicating a stable atmosphere.

Stability is evaluated by comparing the environmental lapse rate with the theoretical adiabatic lapse rates: the Dry Adiabatic Lapse Rate (DALR $\approx 9.8 \text{ K km}^{-1}$) and the Moist Adiabatic Lapse Rate (MALR, typically $4\text{--}7 \text{ K km}^{-1}$, depending on humidity). Strongly stable conditions occur during temperature inversions, where temperature increases with height. Surface-based inversions commonly form at night within the lowest few hundred metres, while subsidence inversions associated with high-pressure systems often appear between $1\text{--}3 \text{ km}$. Such inversions act as barriers to vertical mixing and are crucial for air pollution accumulation.

When moist air parcels rise, they initially follow the DALR until reaching the Lifting Condensation Level (LCL), where condensation begins. The release of latent heat during condensation (an exothermic process) partially offsets adiabatic cooling, increasing the parcel's buoyancy and shifting it to follow the MALR. If sufficient energy is available, the parcel reaches the Level of Free Convection (LFC) and may

continue to ascend to the Equilibrium Level (EL), near the tropopause.

The atmospheric layer closest to the surface is the Planetary Boundary Layer (PBL), where turbulence and mixing are most pronounced due to surface heating and friction. The structure and height of the PBL vary diurnally and are strongly influenced by radiative forcing and atmospheric stability. During the daytime, especially in wildfire regions, intense surface heating and smoke-induced turbulence may erode stable layers, promoting deep mixing.

These vertical motions have significant implications for aerosol dispersion. In stable conditions, especially under inversions, particulate matter accumulates near the surface due to suppressed mixing. Under unstable, convective conditions, particles are efficiently mixed and vertically transported.

CAPE quantifies the potential energy that a rising air parcel can convert into kinetic energy if lifted adiabatically. Higher CAPE values suggest stronger updrafts and a greater likelihood of convective development, enhancing vertical mixing and pollutant dispersion. CIN, on the other hand, represents the energy barrier that must be overcome for a parcel to initiate free convection. Large CIN values suppress vertical motion and contribute to the accumulation of pollutants and aerosols near the surface.

The regions impacted by these two energy terms are bounded by two key levels: the LFC and the EL. Below the LFC, the parcel is cooler than its environment, requiring energy input to rise – this energy defines the CIN. Above the LFC, the parcel is positively buoyant, contributing to CAPE. These estimates often assume pseudo-adiabatic processes (no entrainment and removal of condensed water), allowing latent heat release to maintain saturation.

In wildfire scenarios, evaluating CAPE and CIN becomes particularly relevant for assessing pyroconvection. Wildfires inject substantial heat and moisture into the atmosphere, potentially reducing local CIN (by warming the PBL) and allowing parcels to reach their LFC. When background CAPE is significant, this can trigger the formation of convective clouds (flammagenitus or pyrocumulus), and in extreme cases, deep convective events such as pyroCb (pyrocumulonimbus). Studies have shown that intense fire heat fluxes increase CAPE and reduce CIN, facilitating the vertical transport of smoke and the development of fire-induced storms.

In addition, turbulent fluxes generated by rising air parcels and plume dynamics influence pollutant dispersion. Parcels moving upward often carry higher aerosol concentrations, resulting in well-defined plume cores. This distribution can often be approximated by Gaussian profiles in horizontal cross-sections, in agreement with Fick's law of diffusion, where the diffusion flux is proportional to the gradient in species concentration.

The interaction of aerosol particles with radiation is governed by two fundamental optical processes: scattering and absorption. Scattering occurs when incident electromagnetic

radiation is redirected by particles. In the case of Mie scattering, relevant when the particle diameter is comparable to the wavelength of the incident radiation, light penetrates the particle, and the internal refractive index gradients cause the redirection of light. OC aerosols act primarily as efficient shortwave scatterers, although certain organic fractions (e.g., brown carbon) can contribute weak absorption in the UV–blue region.

Absorption involves the uptake of photon energy by electrons in the atoms or molecules of the aerosol particle. The absorbed energy excites electrons to higher energy levels, and as they relax to their ground states, the energy is primarily dissipated through non-radiative processes, increasing the internal kinetic energy of the particle. This manifests macroscopically as thermal heating of the particle, i.e., the conversion of radiant energy into thermal energy. BC is a strong absorber in the visible and near-infrared spectra and significantly contributes to atmospheric heating.

While both OC and BC interact with radiation in the UV–visible range (0.3–0.7 μm), for most fine-mode aerosols, LW radiative effects are weaker than SW effects, although dense, absorbing smoke layers can exert measurable LW heating through absorption and thermal re-emission.

The absorption of SW radiation by BC-rich aerosol layers elevates local temperatures, promoting thermal stability. This may lead to or enhance thermal inversions, thereby increasing CIN and inhibiting convection and cloud formation. In contrast, OC scattering reduces incoming SW radiation and cools the surface, reducing the surface–atmosphere temperature contrast and decreasing the lapse rate. This stabilisation of the lower troposphere lowers CAPE and diminishes the buoyant energy available for vertical motion.

To link these thermodynamic mechanisms to the radiative forcing exerted by the plume, Fig. 16a–d present the shortwave (SW) and longwave (LW) surface flux perturbations induced by smoke at 16:00 UTC (fresh phase, t_1) and 19:00 UTC (mixed phase, t_2). In all panels, the fields are expressed as No Fire – Fire, such that positive values denote a reduction in downwelling flux caused by the presence of smoke (i.e., the fire simulation receives less radiative energy at the surface than the no-fire control), while negative values correspond to an increase in downwelling flux in the fire run. This definition allows a direct attribution of radiative effects to smoke processes alone, isolating aerosol scattering, absorption, and thermal re-emission relative to a clean-air background. Figure 16 therefore provides a physically coherent depiction of how the plume modifies the surface radiative energy budget during the late-afternoon transition (16:00–19:00 UTC), linking these perturbations to the aerosol optical characteristics described in Figs. 7–12.

At 16:00 UTC, during the fresh and more concentrated phase of the plume, SW anomalies TS13 reach values below -500 W m^{-2} TS14 within the plume core. These large negative TS15 differences indicate that the fire simulation receives substantially less solar radiation at the surface due to strong

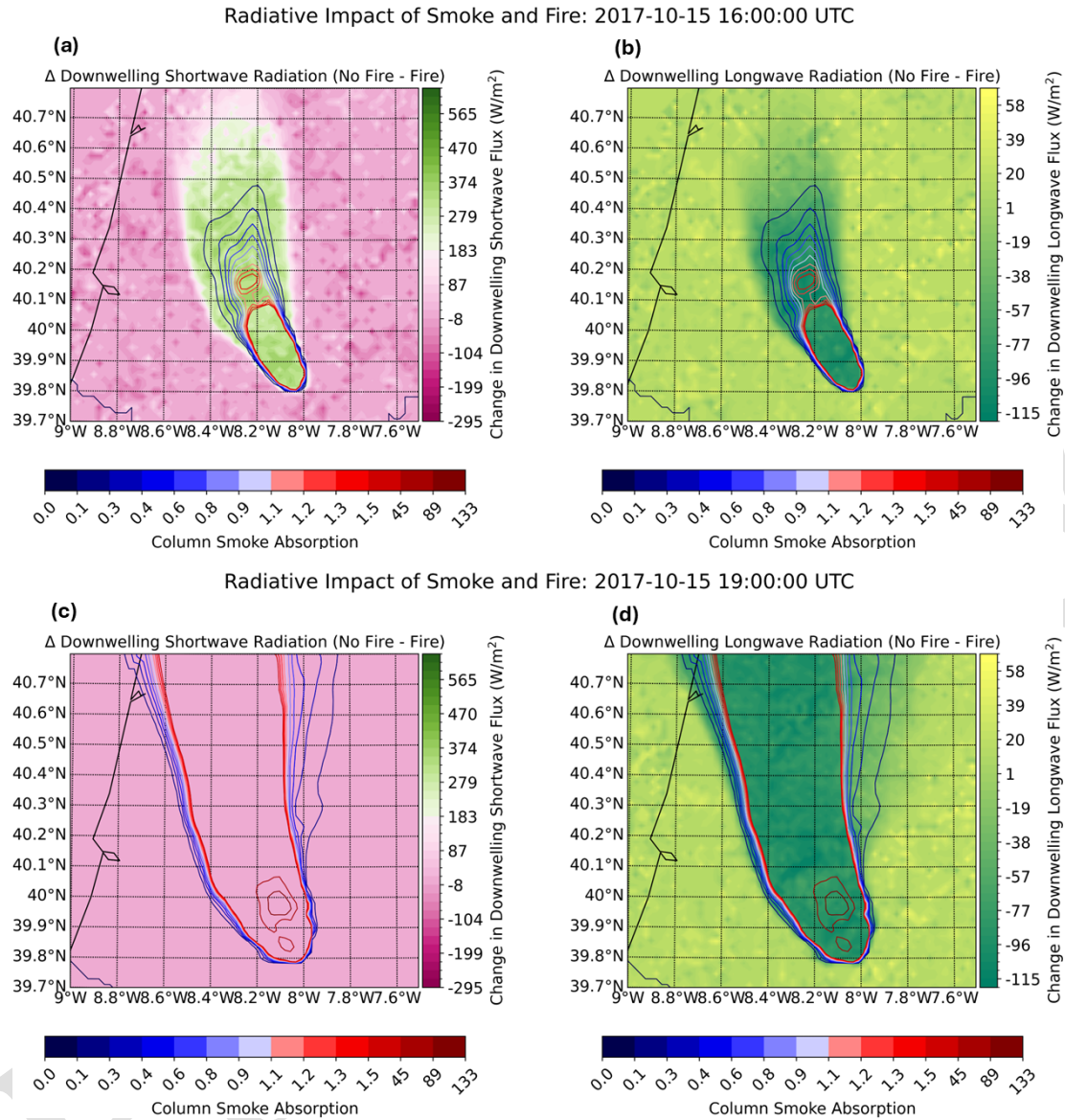


Figure 16. Difference in surface downwelling shortwave (SW) and longwave (LW) radiative fluxes between simulations without fire and with fire (No Fire – Fire) at 16:00 and 19:00 UTC on 15 October 2017. Positive values indicate reduced downwelling radiation in the Fire simulation relative to the no-fire control, while negative values indicate enhanced downwelling radiation at the surface in the Fire case. In the SW panels, negative anomalies [TS11](#) reflect strong attenuation of solar radiation within the plume core. In the LW panels, negative anomalies [TS12](#) indicate increased atmospheric longwave emission in smoke-affected regions. Coloured contour lines denote fire-weighted column smoke absorption.

aerosol extinction. The spatial maxima of SW attenuation are tightly collocated with regions of enhanced column smoke absorption, highlighting the direct radiative impact of high aerosol loading.

In the longwave band, ΔLW values are predominantly negative (approximately -40 to -60 W m^{-2}) within the same regions, indicating enhanced downwelling longwave radiation in the fire simulation relative to the no-fire control. This increase in surface LW flux is consistent with additional

atmospheric emissivity associated with the warm, smoke-laden air mass and fire-induced moisture perturbations.

By 19:00 UTC, the smoke plume becomes more diluted, and its column-absorption contours stretch downwind, indicating transport and dispersion during the transition to the mixed phase. Consistent with this dilution, the shortwave perturbation remains evident but is weaker and more spatially diffuse, with the strongest SW reductions confined to the regions of highest column absorption. In the longwave, the perturbation persists and remains closely collocated with the ab-

Vertical Profiles - 550 nm Ions: -8.1 — 2017-10-15 15:00:00 UTC

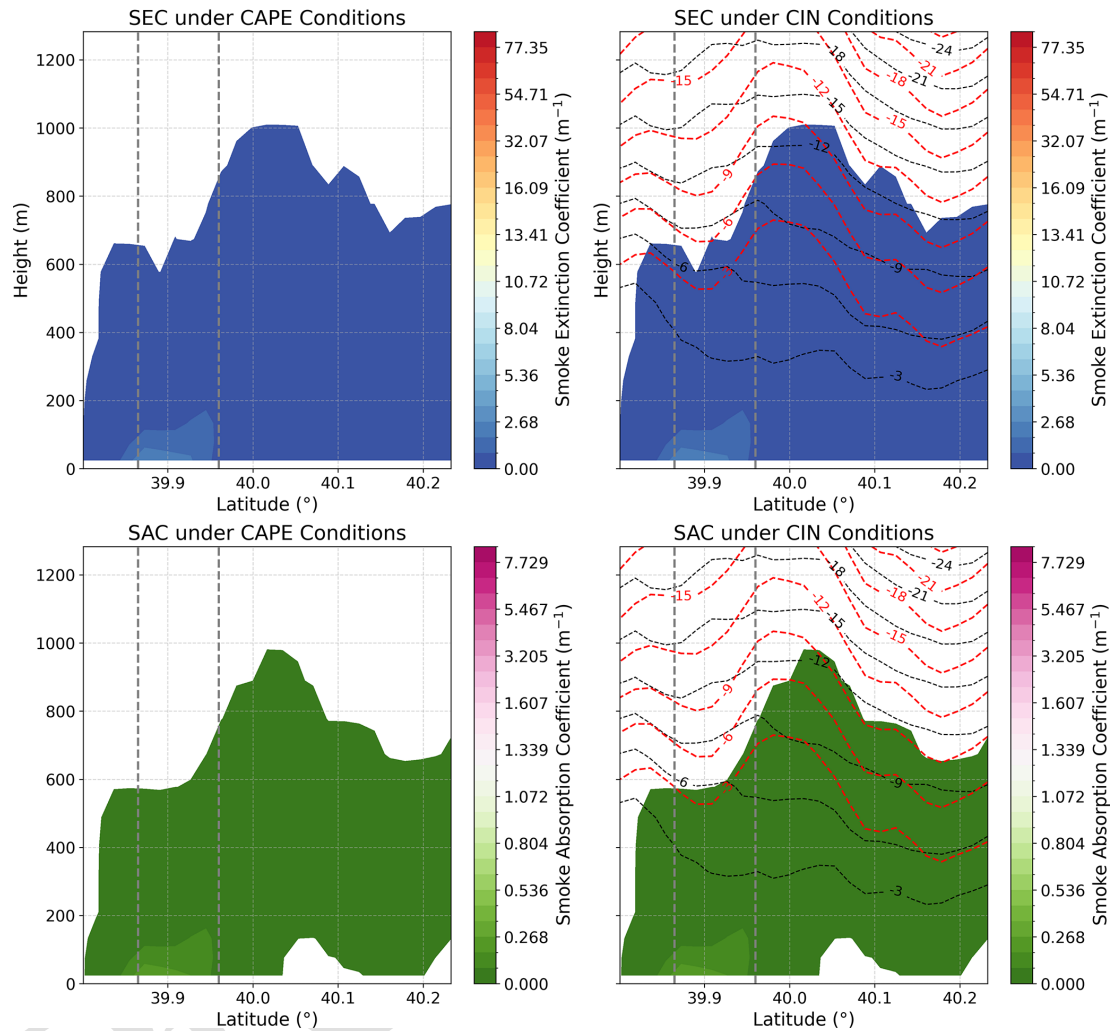


Figure 17. Meridional cross-sections of smoke extinction and absorption coefficients at 550 nm along 8.1° W, under CAPE (J kg^{-1}) and CIN (J kg^{-1}) conditions. Dashed black lines indicate the fire simulation, while dashed red lines represent the no-fire scenario, at 15:00 UTC on 15 October 2017. The region enclosed between the two light gray dashed vertical lines represents the observed area affected by the wildfire.

sorption maxima, indicating enhanced downwelling LW in the fire within the plume core. Together, the SW reduction and LW increase show that the plume continues to modify the surface radiative budget across both phases, while the spatial structure of the signal increasingly reflects plume dilution and advection.

Beyond the instantaneous flux perturbations, the reduction in shortwave irradiance within the plume-affected boundary layer limits surface-driven buoyancy production, while the enhanced longwave emissivity of the smoke layer increases radiative heating aloft. This differential heating between the surface and the lower troposphere favours the development or strengthening of a temperature inversion, effectively acting as a radiative lid over the boundary layer. Such radiatively induced modifications in stability suppress turbulent

mixing and promote boundary-layer stabilisation during periods of peak smoke loading, providing a dynamical pathway through which aerosol optical properties can influence boundary-layer evolution and help explain the persistence of high near-surface $\text{PM}_{2.5}$ concentrations observed in Sect. 3.4. Because the strength of this mechanism depends on aerosol absorption characteristics, the SSA biases identified earlier suggest that the model may underestimate the magnitude of smoke-induced radiative heating within the plume core, implying that the stabilising radiative lid could be even more pronounced under fully absorbing conditions.

Meridional cross-sections of extinction (SEC) and absorption (SAC) along 8.1° W (Figs. 17–19) reveal how spectrally dependent radiative heating interacts with lower-tropospheric stability during the evolution of the smoke

Vertical Profiles - 550 nm Ions: -8.1 — 2017-10-15 19:00:00 UTC

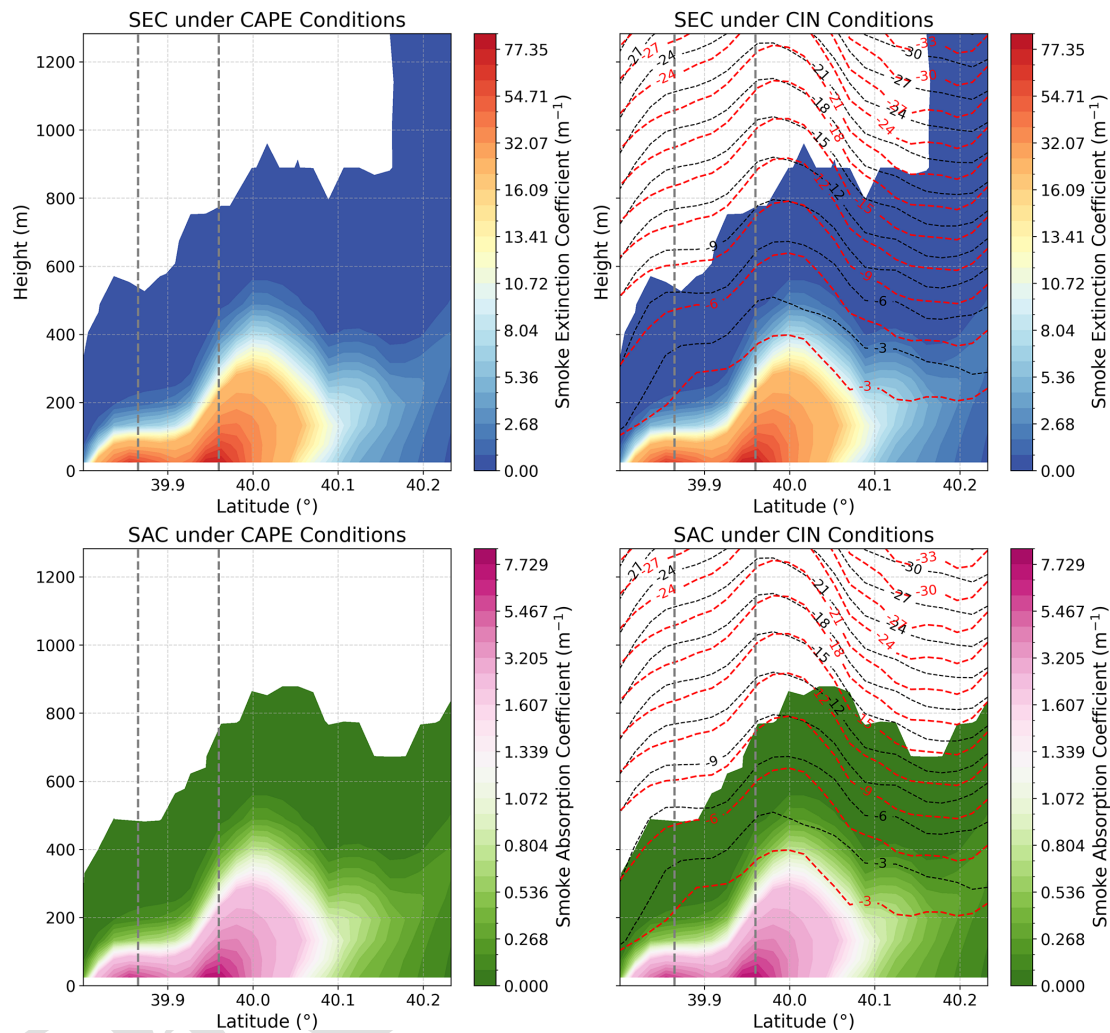


Figure 18. Meridional cross-sections of smoke extinction and absorption coefficients at 550 nm along 8.1° W, under CAPE (J kg^{-1}) and CIN (J kg^{-1}) conditions. Dashed black lines indicate the fire simulation, while dashed red lines represent the no-fire scenario, at 19:00 UTC on 15 October 2017. The region enclosed between the two light gray dashed vertical lines represents the observed area affected by the wildfire.

plume. Colour shading denotes SEC and SAC at the relevant wavelength, while solid black and dashed red isolines represent the Fire and No-Fire CIN and CAPE, respectively. CAPE is absent within the 0–1.2 km layer and is therefore omitted; CIN is shown only where non-zero.

At 15:00 UTC and 550 nm (Fig. 17), extinction and absorption are concentrated within the lowest 300–500 m, forming a compact, optically intense layer centred near 40° N. The near-perfect co-location of SEC and SAC maxima indicates a fresh, BC/OC-rich plume with minimal dilution. CIN isolines in the Fire simulation lie systematically above those of the No-Fire run, evidencing a localized weakening of the low-level inversion. This displacement is consistent with shortwave heating by BC-containing aerosols, which warms the plume and begins to erode static stability,

an early manifestation of the radiative-lid mechanism diagnosed from the surface forcing fields in Fig. 16.

By 19:00 UTC (Fig. 18), the plume has deepened and become more vertically diffuse, with SEC and SAC extending intermittently up to ~ 1 km. CIN perturbations intensify and expand horizontally between 39.9–40.1° N, demonstrating persistent thermodynamic modification by aged, lofted smoke. The joint action of turbulent mixing and continued radiative heating suppresses surface–atmosphere coupling, favouring the accumulation and persistence of smoke near the surface. The spatial coherence between elevated CIN and enhanced SEC/SAC confirms that smoke-driven warming remains dynamically relevant even after the plume has become partially diluted.

Vertical Profiles - 700 nm lons: -8.1 — 2017-10-15 19:00:00 UTC

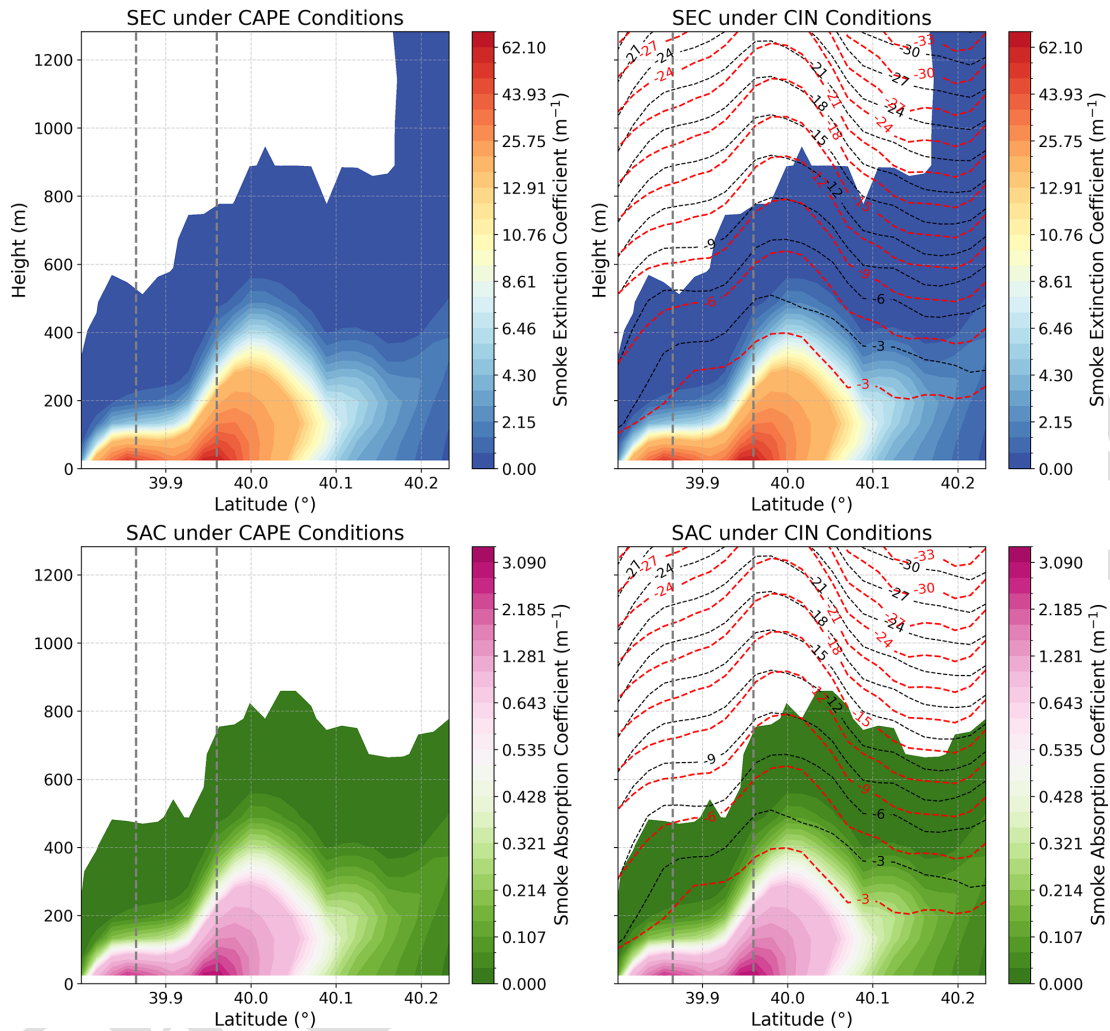


Figure 19. Meridional cross-sections of smoke extinction and absorption coefficients at 700 nm along 8.1° W, under CAPE (J kg^{-1}) and CIN (J kg^{-1}) conditions. Dashed black lines indicate the fire simulation, while dashed red lines represent the no-fire scenario, at 19:00 UTC on 15 October 2017. The region enclosed between the two light gray dashed vertical lines represents the observed area affected by the wildfire.

At 700 nm (Fig. 19), extinction and absorption weaken systematically, SAC decreases by a factor of $\sim 2\text{--}3$ and SEC by 30 %–40 % relative to 550 nm, yet the plume retains its vertical structure, and CIN isolines continue to be elevated in the Fire simulation. This attenuation reflects the wavelength dependence of mixed BC–OC aerosols: as organic chromophores (brown carbon) become optically less active in the red/near-infrared, BC-driven heating increasingly dominates the radiative response.

Conversely, at shorter wavelengths (e.g., 400 nm), SEC and SAC strengthen markedly ($\text{SEC} \approx 3.3 \times 10^{-2} \text{ m}^{-1}$; $\text{SAC} \approx 6 \times 10^{-3} \text{ m}^{-1}$), remaining confined within the lowest 500–800 m, precisely where CIN anomalies TS16 are largest. This pronounced shortwave sensitivity, driven by OC and brown carbon absorption, reinforces the mechanism whereby vis-

ible/UV heating enhances plume buoyancy relative to its surroundings, modifies lower-tropospheric stability, and prolongs near-surface smoke residence.

Together, Figs. 17–19 show that radiative heating by BC and OC governs the vertical thermodynamic imprint of the plume, with 550 nm providing the strongest combined scattering–absorption signal, 700 nm capturing the persistence of BC-induced heating, and 400 nm emphasising the intense shortwave sensitivity of OC-dominated smoke. These spectral responses align with the radiative perturbations diagnosed at the surface (Fig. 16), collectively demonstrating how smoke modifies stability through a vertically structured and wavelength-dependent radiative forcing.

The inversion-layer analysis shown in Figs. 20–21 provides the dynamical counterpart to the radiative and optical

Vertical Profiles - 550 nm lons: -8.1 — 2017-10-15 15:00:00 UTC

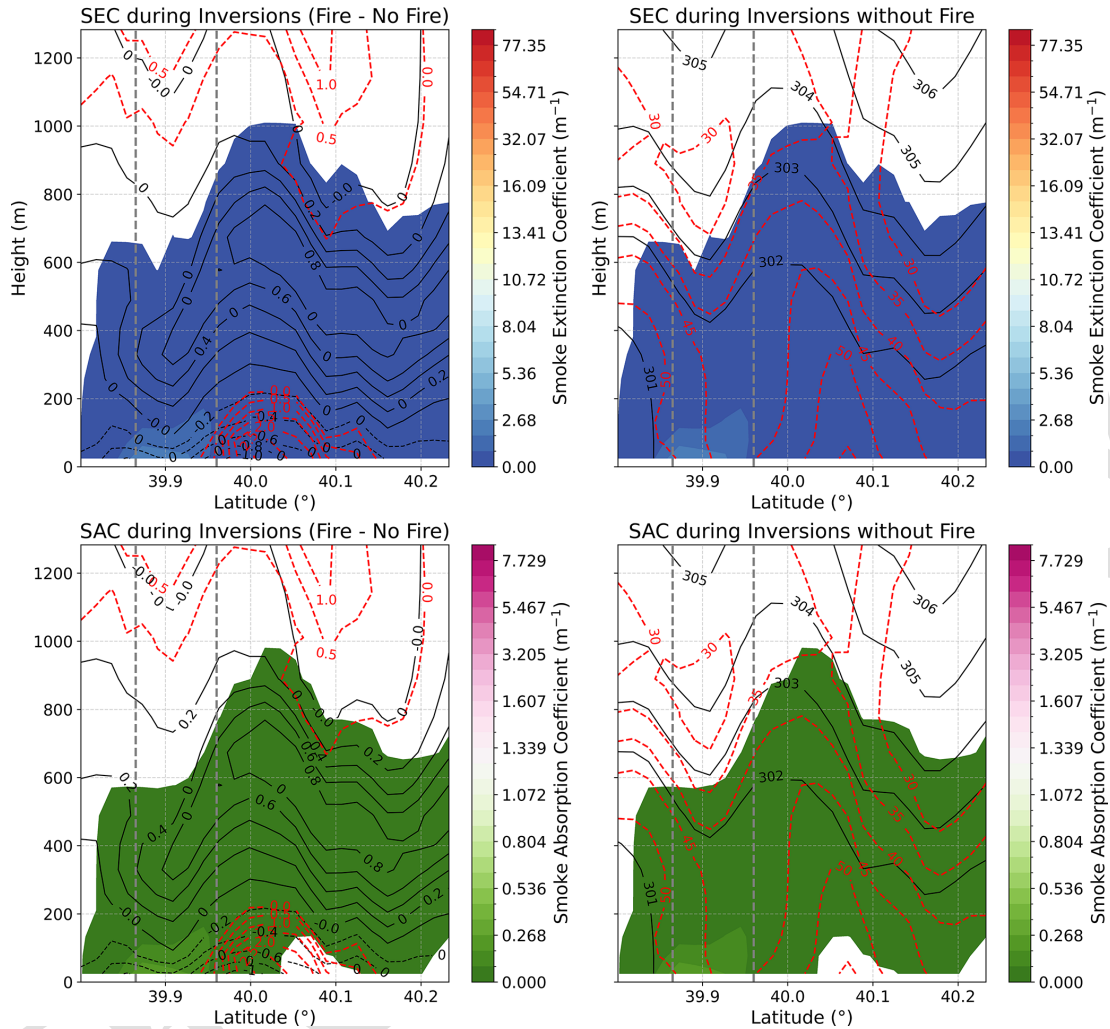


Figure 20. Meridional cross-sections of inversion layers overlaid with smoke extinction and absorption coefficients at 550 nm along 8.1° W. Dashed red lines indicate relative humidity (%), and solid black lines represent potential temperature (K). Simulations correspond to 15:00 UTC on 15 October 2017. The region enclosed between the two light gray dashed vertical lines represents the observed area affected by the wildfire.

diagnostics discussed in Figs. 16–19. Together, these results reveal how smoke functions not merely as a passive tracer but as an active radiative agent capable of reshaping lower-tropospheric stability during the late-afternoon evolution of the plume.

At 15:00 UTC (Fig. 20), a compact near-surface smoke layer, characterised by strong extinction and absorption at 550 nm, coincides with positive potential-temperature anomalies (TS17) ($\theta' \approx 1$ – 1.5 K) and reduced relative humidity ($RH' < 0$) beneath the inversion. These signatures represent the first thermodynamic imprint of radiative heating by the plume: the smoke-induced warming does not physically lift the inversion but erodes it from below, weakening the temperature gradient that sustains its stability. Im-

mediately above the inversion, $RH' > 0$ indicates moisture redistribution by modified turbulent mixing, consistent with a plume that is already altering the thermodynamic environment rather than simply responding to it. This early behaviour aligns with the shortwave-absorption patterns diagnosed in Fig. 16 and with the vertical concentration of extinction and absorption shown at 550 nm in Fig. 17.

By 19:00 UTC (Fig. 21), the perturbations intensify and extend vertically to 300–600 m, mirroring the deepened SEC/SAC fields documented in Figs. 18–19. The θ' anomalies (TS18) strengthen along the plume axis, and the accompanying RH' dipole (dry below, moist above) becomes more pronounced. These changes demonstrate that the inversion is becoming thermodynamically weaker and spatially irregular,

Vertical Profiles - 550 nm Ions: -8.1 — 2017-10-15 19:00:00 UTC

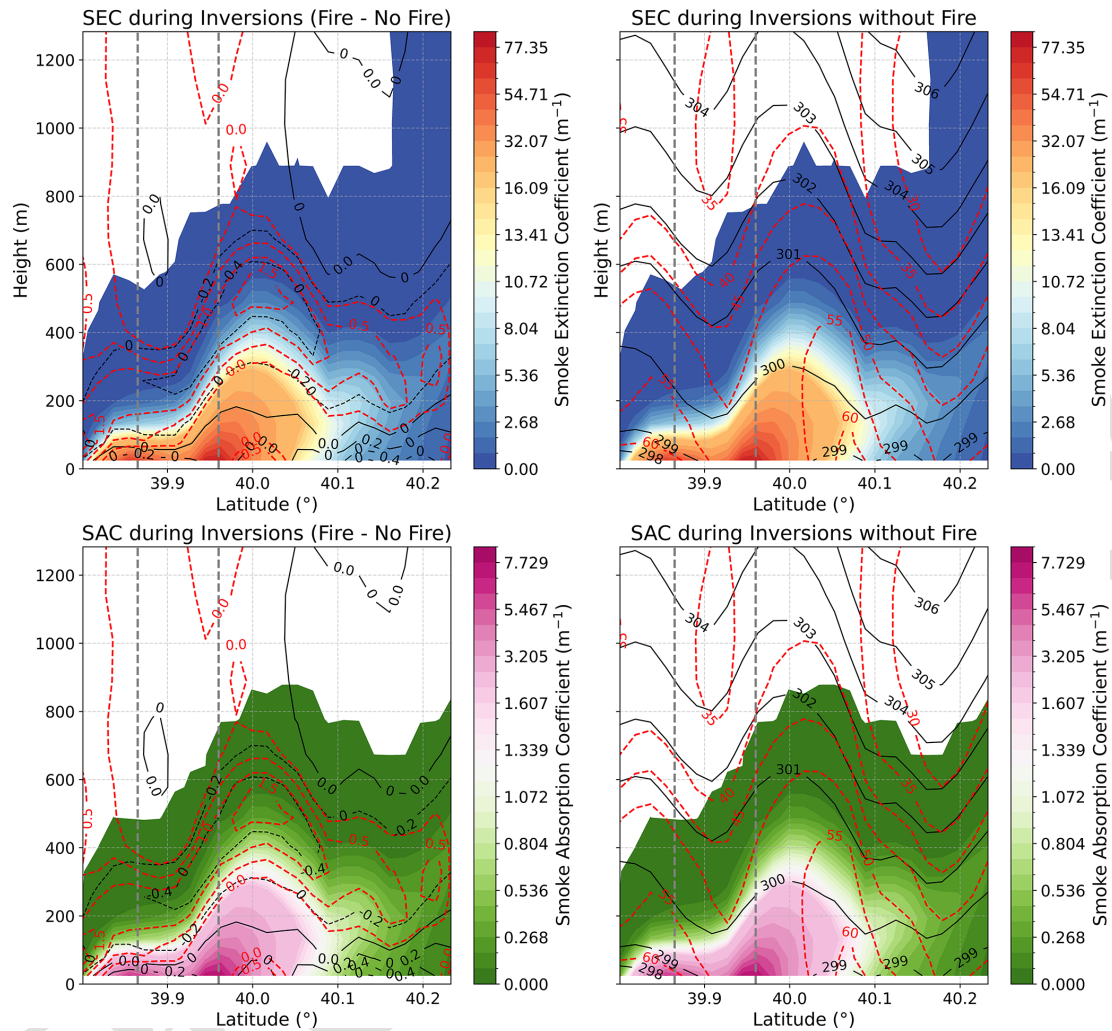


Figure 21. Meridional cross-sections of inversion layers overlaid with smoke extinction and absorption coefficients at 550 nm along 8.1° W. Dashed red lines indicate relative humidity (%), and solid black lines represent potential temperature (K). Simulations correspond to 19:00 UTC on 15 October 2017. The region enclosed between the two light gray dashed vertical lines represents the observed area affected by the wildfire.

not through geometric uplift, but through sustained modification of temperature and moisture stratification driven by radiative heating and plume-induced turbulence. This evolution is fully consistent with the radiative-lid mechanism inferred from SW/LW flux perturbations in Fig. 16: strong shortwave attenuation reduces surface heating, while long-wave trapping and BC/OC absorption warm the lower troposphere, suppressing boundary-layer deepening and enabling the continued presence of lofted aerosol layers.

The co-location of FIRE–No Fire anomalies (TS19) with regions of enhanced SEC and SAC further confirms that inversion modification is directly coupled to the plume’s wavelength-dependent radiative forcing. Heating by dense smoke is particularly efficient at short wavelengths (400–

550 nm), reinforcing the thermodynamic anomalies (TS20) at low levels and supporting persistent vertical redistribution of smoke. In this way, the inversion cross-sections provide a dynamical validation of the radiative pathways previously identified, demonstrating how smoke alters both the strength and structure of stability regimes that ultimately govern plume dispersion and residence time.

3.6 Origin and Interpretation of Extreme PM_{2.5} and SOD Values

Because the BRAMS–SFIRE simulations were performed over a limited regional domain that does not cover all of continental Portugal, a natural concern is that artificial aerosol

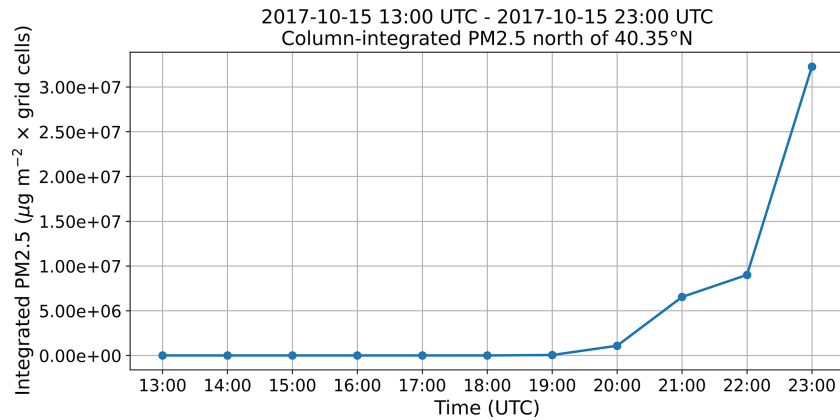


Figure 22. Time series of the domain-integrated column PM_{2.5} of BRAMS domain north of 40.35° N on 15 October 2017. The values represent the spatial sum of column-integrated PM_{2.5} over all grid cells located north of the latitude threshold.

accumulation might arise through numerical trapping near the downwind boundary. To assess this, we analysed the domain-integrated column PM_{2.5} north of 40.35° N (Fig. 22). The resulting time series shows no spurious monotonic increase or retention unrelated to plume evolution; instead, column mass increases and declines in phase with the fire activity and plume advection. This confirms that boundary conditions do not dominate the simulated aerosol budget.

To diagnose the physical origin of the sharp local maxima inside the domain, we examined the joint evolution of vertically integrated PM_{2.5} and surface sensible heat flux at three representative locations along the plume pathway (Source, Midpoint, Endpoint; Fig. 23). In all cases, abrupt increases in PM_{2.5} coincide with intense pulses of sensible heat flux, a signature of vigorous combustion and rapid vertical injection. These maxima are confined to limited regions near the active fire front or within the nascent plume core, reflecting steep near-source gradients characteristic of high-intensity crown–surface fire propagation. Such behaviour differs fundamentally from prescribed burns or low-intensity wildfires (Adetona et al., 2016; Miranda et al., 2010), which exhibit broader plume cross-sections and more gradual dilution.

The alignment of the PM_{2.5} spikes with heat-flux pulses strongly suggests that the extreme column PM_{2.5} values originate from physically plausible, highly localised fire–atmosphere interactions. However, the sensitivity of these peaks to the local sensible heat flux also indicates that uncertainties in fuel load, vegetation composition, and canopy structure can amplify near-source emissions and confine the initial aerosol distribution more strongly than observed. In mixed Mediterranean forest systems, where fuel heterogeneity is pronounced, misrepresentation of understory and crown biomass can substantially bias the heat release rate and, consequently, the vertical and horizontal gradients of PM_{2.5}. Improved fuel mapping and characterisation would therefore likely reduce the magnitude of these extremes in future simulations.

This interpretation is consistent with the behaviour observed in SOD and extinction fields. Earlier sections showed that SOD exhibits a heavy-tailed distribution and extremely sharp local maxima, some of which exceed values supported by field and remote-sensing observations. These peaks align spatially with the PM_{2.5} spikes identified here, suggesting a shared origin in over-intensified near-source injection rather than in domain-scale numerical artefacts. While numerical transport under very steep concentration gradients can modulate local extremes, the evidence from Figs. 22–23 indicates that the dominant contribution originates upstream, during the emission and injection stage, rather than during plume advection.

This conclusion is consistent with the discrepancies previously noted between BRAMS–SFIRE SOD and MERRA-2 extinction, SSA, and BC/OC partitioning. The strongest disagreements occurred in regions where BRAMS–SFIRE produced exceptionally concentrated plume cores. These differences likely stem not from the radiative or microphysical parametrisations themselves but from the fire source term, which controls the thermal and mass fluxes injected into the atmosphere. In particular, uncertainties in the formulation of the radiative power-to-mass conversion (Sect. “Implementation of FRP in SFIRE”) and its dependency on fuel type and combustion phase can introduce biases in the magnitude and vertical placement of smoke emissions. A systematic reassessment of these parameters, together with refined fuel maps for Iberian vegetation types, would help reduce the sharpness of near-source gradients and improve agreement with regional-scale observations.

Finally, consistent with previous observational and modelling studies (Carroll et al., 2025; Huff et al., 2021; Lareau and Clements, 2015; Reid et al., 2005), the extreme values occupy only a negligible fraction of the domain and do not characterise the broader plume. The large-scale structure agrees well with MERRA-2 AOD, indicating that the SOD, extinction, and SSA diagnostics analysed in earlier

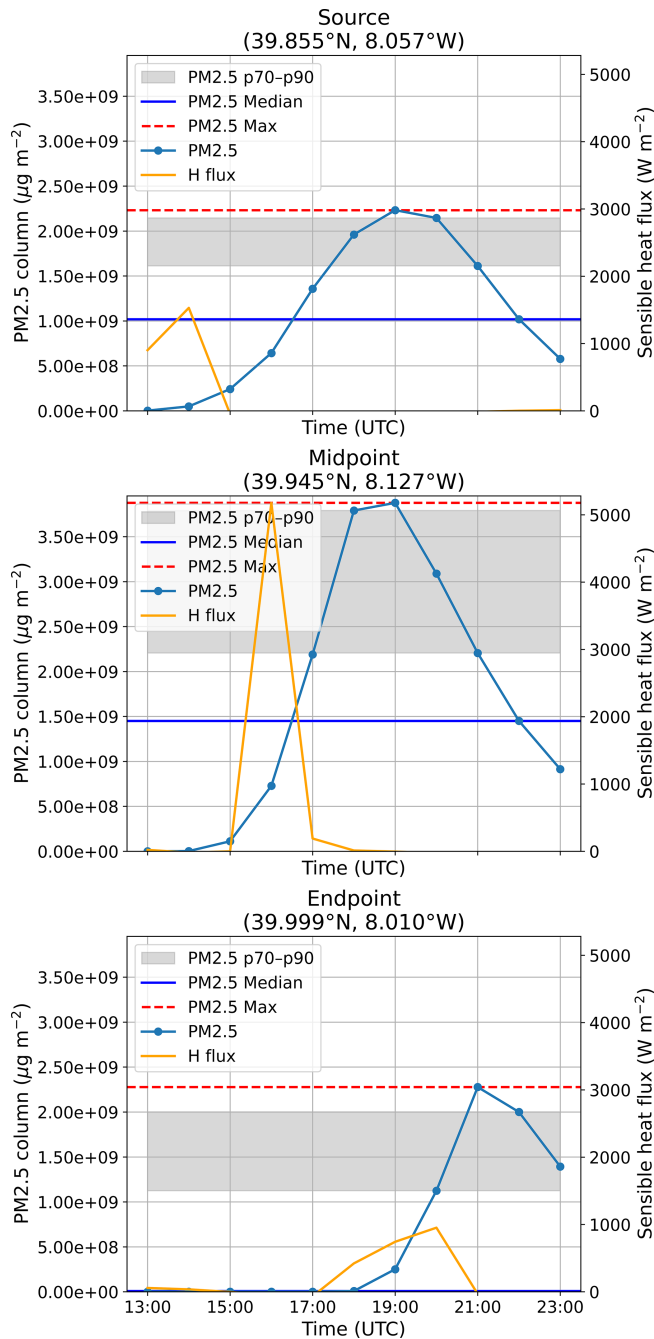


Figure 23. Time series of column-integrated $\text{PM}_{2.5}$ mass ($\mu\text{g m}^{-2}$) and surface sensible heat flux (W m^{-2}) at three representative grid locations along the plume pathway: Source, Midpoint, and Endpoint. For each location, the shaded band denotes the $\text{PM}_{2.5}$ p70–p90 percentile range, while solid and dashed lines indicate the $\text{PM}_{2.5}$ median and maximum, respectively. The orange curve shows the corresponding sensible heat flux extracted from the same grid cell.

sections predominantly reflect the regional plume evolution rather than isolated near-source spikes. Taken together, the evidence in Figs. 22–23 demonstrates that the extreme $\text{PM}_{2.5}$ and SOD values arise from physically consistent but highly localised fire–atmosphere processes, intensified by uncertainties in fuel representation and emission parameterisation, rather than from numerical accumulation or domain-boundary artefacts.

4 Conclusions

The combined results demonstrate that the BRAMS–SFIRE modelling system, with explicit two-way smoke–radiation coupling, successfully reproduces the key optical, radiative, and thermodynamic responses associated with an intense wildfire event. For the 15 October 2017 episode, the simulations capture both the spectral dependence of smoke extinction and absorption and the resulting restructuring of lower-tropospheric stability. Enhanced shortwave absorption across 400–700 nm, together with localized longwave re-emission, generated radiative caps that inhibited nocturnal cooling (TS21) and displaced CIN layers upward by approximately 100–200 m. Simultaneously, localized increases in CAPE signal the onset of radiative–convective feedbacks. These features are consistent with the observed diurnal evolution of stability and confirm the central role of smoke-induced heating in modifying boundary-layer dynamics and inversion strength.

The comparison between simulated Smoke Optical Depth (SOD) and MERRA-2 Aerosol Optical Depth (AOD) shows that the apparent amplitude and phase differences primarily reflect the distinct spatial scales, temporal averaging, and compositional assumptions inherent to each dataset. BRAMS–SFIRE resolves fine-scale, freshly emitted plume structures, while MERRA-2 provides a smoothed, multi-species column that integrates regional background aerosols. Despite these inherent differences, the simulations reproduce the main spatial organisation and timing of the observed plume (TS22), with the wet microphysical configuration providing the closest match, particularly during the mixed phase (19:00–20:00 UTC), when hygroscopic growth, carbonaceous dominance, and stabilized plume geometry align most favourably.

Diagnostic statistics (Tables S1–S3) confirm that upwind-based background subtraction systematically improves agreement, reducing biases and modestly increasing correlation. (TS23) Percentile masks (P70–P90) isolate the plume core and reveal that microphysical perturbations, including ABSORBING-like, WIDE SIGMA, and scaled $r_{g,dry}$, introduce only small differences in the diagnostics, underscoring the robustness of the implemented optical parameterizations. These results highlight that discrepancies with MERRA-2 arise mainly from representativeness and resolution constraints rather than from deficiencies in the microphysical closure.

Table 7. Symbols and variables used in the text.

Symbol	Definition	Unities
R_{surface}	Surface fire spread rate	m s^{-1}
$R_{\text{initialization}}$	Equivalent rate of spread used for model initialization	m s^{-1}
R_{active}	Active crown fire spread, set to 40 % of the observed 6.1 m windspeed at midflame height	m s^{-1}
R_{10}	Surface fire spread rate for fuel behavior model 10	m s^{-1}
$R_{\text{back}10}$	Backing spread rate for fuel behavior model 10	m s^{-1}
$R_{\text{wind}10}$	Spread rate due to wind factor for fuel behavior model 10	m s^{-1}
$R_{\text{slope}10}$	Spread rate due to slope factor for fuel behavior model 10	m s^{-1}
R_{final}	Total fire spread rate	m s^{-1}
$I_{\text{initialization}}$	Fireline intensity of the surface fire	W m^{-1}
I_{r10}	Reaction intensity for NFFL fuel behavior model 10	W m^{-1}
I_{final}	Final fire intensity, accounting for the interaction between surface and canopy fuels	W m^{-1}
ϕ	Fire energy flux	W m^{-2}
H	Heat yield of the fuel; mass of fuel consumed in the flaming front	kJ m^{-2}
H_{Low}	Lower heat content of the fue	kJ kg^{-1}
t_r	Residence time for the fuel model	s
σ_{10}	Surface-area-to-volume ratio for fuel behavior model 10	m^{-1}
w_{surface}	Initial total mass of surface fuel	kg m^{-2}
FMC	Foliar moisture content	%
FME	Foliar moisture effect	–
FME ₀	Reference foliar moisture effect for FMC = 100 %	–
CFB	Crown fraction burned	–
P	Radiative power	MW
ϵ	Emissivity	–
σ	Stefan–Boltzmann constant	$\text{W m}^{-2} \text{K}^{-4}$
A	Burnt area	m^2
T	Temperature	K
Q_s	Sensible heat flux	W m^{-2}
c	Specific heat capacity of dry wood	$\text{J kg}^{-1} \text{K}^{-1}$
m	Mass of burned material	kg

At 19:00 UTC, the model–reanalysis correspondence reaches its maximum: composition fields and extinction profiles confirm that OC-dominated fine-mode aerosols govern optical depth at 550 nm, while BC, though optically less dominant, exerts a disproportionate influence on local heating and inversion modification. The interplay between hygroscopic growth, carbonaceous composition and longwave radiative trapping explains why this period exhibits the most realistic coupling between optical and thermodynamic structure.

A further conclusion emerging from this study concerns the sensitivity of near-source $\text{PM}_{2.5}$ and SOD to uncertainties in fuel characterisation. The additional diagnostics performed here demonstrate that the extreme $\text{PM}_{2.5}$ values occur in a very small number of grid cells co-located with peaks in sensible heat flux, indicating that they originate from the intense heat release imposed by the prescribed surface–crown fire regime. While such values are physically plausible for high-intensity crown fire conditions, their magnitude also suggests that part of the local overestimation likely stems from uncertainties in the specification of vegetation

type, fuel load and canopy structure over the burned area. Because these parameters directly control fireline intensity and emission density, improved fuel mapping for Mediterranean mixed-forest understories is expected to reduce the amplitude of these near-source extremes in future simulations. Importantly, these local maxima do not affect the plume-scale optical diagnostics, which remain consistent with MERRA-2 constraints.

Overall, the BRAMS–SFIRE system reproduces the characteristic feedback loop of large fire plumes: enhanced short-wave absorption, inversion reinforcement, CIN displacement, CAPE modulation, and the persistence of near-surface smoke under radiative stabilization. The consistency of these behaviours across multiple configurations demonstrates that the combined microphysical–radiative schemes are physically sound, and that remaining mismatches with reanalysis datasets stem chiefly from unavoidable scale discrepancies.

Furthermore, the explicit representation of crown fire processes in BRAMS enhances the realism in forested and mountainous terrain, where canopy combustion substantially increases heat release, plume buoyancy and aerosol injection

heights. This capability is essential for accurately resolving smoke evolution in Mediterranean-type fire regimes.

Future work will extend this framework to multi-event climatological analyses, improved aerosol-ageing representations, refined fuel–vegetation datasets, and enhanced observational constraints. These developments will strengthen the model's capacity to quantify fire-induced radiative perturbations and to diagnose fire–atmosphere interactions under a rapidly changing climate.

Code and data availability. The version of the BRAMS model used to produce the results presented in this paper is available under the Creative Commons Attribution 4.0 International License on <https://doi.org/10.5281/zenodo.19392038> (Menezes et al., 2025), along with compilation and simulation instructions.

Supplement. The supplement related to this article is available online at [the link will be implemented upon publication].

Author contributions. ICM and LFR developed the coupling within the BRAMS model. ICM also designed the presented experiments, performed the validation, produced the figures and analysis, and wrote the original manuscript. KML and SRF guided the conceptualisation of the coupling implementation in BRAMS. MFF supported the development by correcting conceptual coding errors and assisting with model compilation. RB, VFO, and SC created supporting files for the simulations. In addition, SC contributed to the manuscript review. AIM reviewed the manuscript and supervised the conceptualisation of the model's application.

Competing interests. The contact author has declared that none of the authors has any competing interests.

Disclaimer. Publisher's note: Copernicus Publications remains neutral with regard to jurisdictional claims made in the text, published maps, institutional affiliations, or any other geographical representation in this paper. The authors bear the ultimate responsibility for providing appropriate place names. Views expressed in the text are those of the authors and do not necessarily reflect the views of the publisher.

Acknowledgements. The developments presented in this study were carried out within the FIRESMOKE project, a collaborative effort between the National Institute for Space Research (INPE), in Brazil, and the University of Aveiro, in Portugal, and the Portuguese LARGEFIRES project. They include the integration of crown fire dynamics and the coupling of fire-emitted aerosols with the Coupled Chemistry Aerosol-Tracer Transport model (CCATT) (Longo et al., 2013), allowing for detailed simulation of smoke composition and transport. These developments are being incorporated into the forthcoming BRAMS v6.0.

Financial support. The authors acknowledge the financial support of FCT – Science and Technology Portuguese Foundation I.P., which funded the projects FIRESMOKE (<https://doi.org/10.54499/PTDC/CTA-MET/3392/2020>) and LARGEFIRES (<https://doi.org/10.54499/2023.17415.ICDT>), through national funds. This work was also funded by national funds through FCT, under the project CESAM-Centro de Estudos do Ambiente e do Mar, references UID/50017/2025 (<https://doi.org/10.54499/UID/50017/2025>) and LA/P/0094/2020 (<https://doi.org/10.54499/LA/P/0094/2020>).

Review statement. This paper was edited by Cynthia Whaley and reviewed by two anonymous referees.

References

- Adetona, O., Reinhardt, T. E., Domitrovich, J., Broyles, G., Adetona, A. M., Kleinman, M. T., Ottmar, R. D., and Naeher, L. P.: Review of the health effects of wildland fire smoke on wildland firefighters and the public, *Inhal. Toxicol.*, 28, 95–139, <https://doi.org/10.3109/08958378.2016.1145771>, 2016.
- Àgueda, A., Pastor, E., Pérez, Y., and Planas, E.: Experimental study of the emissivity of flames resulting from the combustion of forest fuels, *Int. J. Therm. Sci.*, 49, 543–554, <https://doi.org/10.1016/j.ijthermalsci.2009.09.006>, 2010.
- Ahmadvov, R., Grell, G., James, E., Csiszar, I., Tsidulko, M., Pierce, B., McKeen, S., Benjamin, S., Alexander, C., Pereira, G., Freitas, S., and Goldberg, M.: Using VIIRS fire radiative power data to simulate biomass burning emissions, plume rise and smoke transport in a real-time air quality modeling system, *Int. Geosci. Remote Se.*, 2017–July, 2806–2808, <https://doi.org/10.1109/IGARSS.2017.8127581>, 2017.
- Albini, F. A.: Estimating Wildfire Behavior and Effects, USDA Forest Service, Intermountain Research Station, General Technical Report, 30, 1976.
- Alexander, M. E.: Help with making crown fire hazard assessments, Gen. Tech. Rep. INT-251. Ogden, UT: U.S. Department of Agriculture, Forest Service, Intermountain Forest and Range Experiment Station, 147–156, 1988.
- Anderson, H. E.: Aids to determining fuel models for estimating fire behavior, US Department of Agriculture, Forest Service, Intermountain Forest and Range Experiment Station, 122, 1982.
- Anderson, K., Chen, J., Englefield, P., Griffin, D., Makar, P. A., and Thompson, D.: The Global Forest Fire Emissions Prediction System version 1.0, *Geosci. Model Dev.*, 17, 7713–7749, <https://doi.org/10.5194/gmd-17-7713-2024>, 2024.
- Andreae, M. O. and Gelencsér, A.: Black carbon or brown carbon? The nature of light-absorbing carbonaceous aerosols, *Atmos. Chem. Phys.*, 6, 3131–3148, <https://doi.org/10.5194/acp-6-3131-2006>, 2006.
- Andreae, M. O. and Merlet, P.: Emission of trace gases and aerosols from biomass burning, *Global Biogeochem. Cy.*, 15, 955–966, 2001.
- Andreae, M. O. and Rosenfeld, D.: Aerosol-cloud-precipitation interactions. Part 1. The nature and sources of cloud-active aerosols, *Earth-Sci. Rev.*, 89, 13–41, <https://doi.org/10.1016/j.earscirev.2008.03.001>, 2008.

- Andrews, P. L. and Rothermel, R. C.: Charts for interpreting wildland fire behavior characteristics, U.S. Department of Agriculture, Forest Service, Intermountain Forest and Range Experiment Station, Ogden, General Technical Report, INT-GTR-13, 21 pp., 1982.
- Apte, J. S., Brauer, M., Cohen, A. J., Ezzati, M., and Pope, C. A.: Ambient PM_{2.5} Reduces Global and Regional Life Expectancy, *Environ. Sci. Tech. Lett.*, 5, 546–551, <https://doi.org/10.1021/acs.estlett.8b00360>, 2018.
- Aranami, K., Davies, T., and Wood, N.: A mass restoration scheme for limited-area models with semi-Lagrangian advection, *Q. J. Roy. Meteor. Soc.*, 141, 1795–1803, <https://doi.org/10.1002/qj.2482>, 2015.
- Baughman, R. G. and Albini, F. A.: Estimating Midflame Windspeeds, in: Proceedings Sixth Conference on Fire and Forest Meteorology, Sixth Conference on Fire and Forest Meteorology, Society of American Foresters, Washington, DC., 88–92, 1980.
- Bermejo, R. and Conde, J.: A Conservative Quasi-Monotone Semi-Lagrangian Scheme, *Am. Meteorol. Soc.*, 423–430, [https://doi.org/10.1175/1520-0493\(2002\)130<0423:ACQMSL>2.0.CO;2](https://doi.org/10.1175/1520-0493(2002)130<0423:ACQMSL>2.0.CO;2), 2002.
- Biscoe, J. and Warren, B. E.: An X-Ray Study of Carbon Black, *J. Appl. Phys.*, 13, 364–371, 1942.
- Bohren, C. F. and Huffman, D. R.: Absorption and scattering of light by small particles, John Wiley & Sons, Ltd., 2008.
- Bond, T. C. and Bergstrom, R. W.: Light absorption by carbonaceous particles: An investigative review, *Aerosol Sci. Tech.*, 40, 27–67, <https://doi.org/10.1080/02786820500421521>, 2006.
- Bond, T. C., Streets, D. G., Yarber, K. F., Nelson, S. M., Woo, J. H., and Klimont, Z.: A technology-based global inventory of black and organic carbon emissions from combustion, *J. Geophys. Res.-Atmos.*, 109, 1–43, <https://doi.org/10.1029/2003JD003697>, 2004.
- Bond, T. C., Doherty, S. J., Fahey, D. W., Forster, P. M., Berntsen, T., DeAngelo, B. J., Flanner, M. G., Ghan, S., Kärcher, B., Koch, D., Kinne, S., Kondo, Y., Quinn, P. K., Sarofim, M. C., Schultz, M. G., Schulz, M., Venkataraman, C., and Zhang, H.: Bounding the role of black carbon in the climate system: A scientific assessment, *J. Geophys. Res.-Atmos.*, 118, 5380–5552, <https://doi.org/10.1002/jgrd.50171>, 2013.
- Buchard, V., da Silva, A. M., Colarco, P. R., Darmenov, A., Randles, C. A., Govindaraju, R., Torres, O., Campbell, J., and Spurr, R.: Using the OMI aerosol index and absorption aerosol optical depth to evaluate the NASA MERRA Aerosol Reanalysis, *Atmos. Chem. Phys.*, 15, 5743–5760, <https://doi.org/10.5194/acp-15-5743-2015>, 2015.
- Buchard, V., da Silva, A. M., Randles, C. A., Colarco, P., Ferrare, R., Hair, J., Hostetler, C., Tackett, J., and Winker, D.: Evaluation of the surface PM_{2.5} in Version 1 of the NASA MERRA Aerosol Reanalysis over the United States, *Atmos. Environ.*, 125, 100–111, <https://doi.org/10.1016/j.atmosenv.2015.11.004>, 2016.
- CAMS: Copernicus Atmosphere Monitoring Service, <https://atmosphere.copernicus.eu/> (last access: 1 November 2024), 2015.
- Carrico, C. M., Petters, M. D., Kreidenweiss, S. M., Collett, J. L., Guenter, E., and Malm, W. C.: Aerosol hygroscopicity and cloud droplet activation of extracts of filters from biomass burning experiments, *J. Geophys. Res.-Atmos.*, 113, 1–9, <https://doi.org/10.1029/2007JD009274>, 2008.
- Carroll, B. J., Strobach, E., Baidar, S., Holloway, M. W., McCarty, B., Marchbanks, R., and Brewer, W. A.: Wildfire Smoke Shading Observations: Impacts on Boundary Layer Mixing and Thermally Driven Smoke Transport, *J. Geophys. Res.-Atmos.*, 130, <https://doi.org/10.1029/2024JD043303>, 2025.
- Chakrabarty, R. K., Gyawali, M., Yatavelli, R. L. N., Pandey, A., Watts, A. C., Knue, J., Chen, L.-W. A., Pattison, R. R., Tsibart, A., Samburova, V., and Moosmüller, H.: Brown carbon aerosols from burning of boreal peatlands: microphysical properties, emission factors, and implications for direct radiative forcing, *Atmos. Chem. Phys.*, 16, 3033–3040, <https://doi.org/10.5194/acp-16-3033-2016>, 2016.
- Clark, T. L., Jenkins, M. A., Coen, J. L., and Packham, D. R.: A coupled atmosphere-fire model: Role of the convective froude number and dynamic fingering at the fireline, *Int. J. Wildland Fire*, 6, 177–190, <https://doi.org/10.1071/WF9960177>, 1996.
- Clark, T. L., Coen, J., and Latham, D.: Description of a coupled atmosphere-fire model, *Int. J. Wildland Fire*, 13, 49–63, <https://doi.org/10.1071/WF03043>, 2004.
- Clinton, N. E., Gong, P., and Scott, K.: Quantification of pollutants emitted from very large wildland fires in Southern California, USA, *Atmos. Environ.*, 40, 3686–3695, <https://doi.org/10.1016/j.atmosenv.2006.02.016>, 2006.
- Coen, J. L.: Simulation of the Big Elk Fire using coupled atmosphere-fire modeling, *Int. J. Wildland Fire*, 14, 49–59, <https://doi.org/10.1071/WF04047>, 2005.
- Curci, G., Hogrefe, C., Bianconi, R., Im, U., Balzarini, A., Baró, R., Brunner, D., Forkel, R., Giordano, L., Hirtl, M., Honzak, L., Jiménez-Guerrero, P., Knote, C., Langer, M., Makar, P. A., Pirovano, G., Pérez, J. L., San José, R., and Syrakov, D.: Uncertainties of simulated aerosol optical properties induced by assumptions on aerosol physical and chemical properties: An AQMEII-2 perspective, *Atmos. Environ.*, 115, 541–552, <https://doi.org/10.1016/j.atmosenv.2014.09.009>, 2015.
- Daniels, J., Liang, L., Benedict, K. B., Brahney, J., Rangel, R., Weathers, K. C., and Ponette-González, A. G.: Satellite-based aerosol optical depth estimates over the continental U.S. during the 2020 wildfire season: Roles of smoke and land cover, *Sci. Total Environ.*, 921, 171122, <https://doi.org/10.1016/j.scitotenv.2024.171122>, 2024.
- Darmenov, A. S., and da Silva, A.: The Quick Fire Emissions Dataset (QFED) – Documentation of versions 2.1, 2.2 and 2.4., NASA/TM-2015-104606, NASA Global Modeling and Assimilation Office, 38, 183 pp., 2015.
- do Rosário, N. É., Longo, K. M., Toso, P. H., Freitas, S. R., Yamasoe, M. A., Rodrigues, L. F., Medeiros, O., Velho, H. C., Menezes, I. D. C., and Miranda, A. I.: Machine learning-driven characterization and prescription of aerosol optical properties for atmospheric models, *Geosci. Model Dev.*, 19, 2691–2716, <https://doi.org/10.5194/gmd-19-2691-2026>, 2026.
- Eck, T. F., Holben, B. N., Giles, D. M., Slutsky, I., Sinyuk, A., Schafer, J. S., Smirnov, A., Sorokin, M., Reid, J. S., Sayer, A. M., Hsu, N. C., Shi, Y. R., Levy, R. C., Lyapustin, A., Arif Rahman, M., Liew, S.-C., Salinas Cortijo, S. V., and Li, T.: AERONET Remotely Sensed Measurements and Retrievals of Biomass Burning Aerosol Optical Properties During the 2015 Indonesian Burning Season, *J. Geophys. Res.-Atmos.*, 124, 4722–4740, <https://doi.org/10.1029/2018JD030182>, 2019.

- Engelhart, G. J., Hennigan, C. J., Miracolo, M. A., Robinson, A. L., and Pandis, S. N.: Cloud condensation nuclei activity of fresh primary and aged biomass burning aerosol, *Atmos. Chem. Phys.*, 12, 7285–7293, <https://doi.org/10.5194/acp-12-7285-2012>, 2012.
- ERA5: Fifth generation ECMWF reanalysis for the global climate and weather, <https://www.ecmwf.int/en/forecasts/dataset/ecmwf-reanalysis-v5> (last access: 5 March 2025), 2019.
- Fernandes, A. P., Lopes, D., Sorte, S., Monteiro, A., Gama, C., Reis, J., Menezes, I., Osswald, T., Borrego, C., Almeida, M., Ribeiro, L. M., Viegas, D. X., and Miranda, A. I.: Smoke emissions from the extreme wildfire events in central Portugal in October 2017, *Int. J. Wildland Fire*, 1–13, <https://doi.org/10.1071/WF21097>, 2022.
- Ferrare, R. A., Fraser, R. S., and Kaufman, Y. J.: Satellite measurements of large-scale air pollution: Measurements of forest fire smoke, *J. Geophys. Res.-Atmos.*, 95, 9911–9925, 1990.
- Filippi, J. B., Pialat, X., and Clements, C. B.: Assessment of FireFire/Meso-NH for wildland fire/atmosphere coupled simulation of the FireFlux experiment, *P. Combust. Inst.*, 34, 2633–2640, <https://doi.org/10.1016/j.proci.2012.07.022>, 2013.
- Forestry Canada Fire Danger Group: Development and structure of the Canadian Forest Fire Behavior Prediction System, *Inf. Rep. ST-X-3*, 63 pp., 1992.
- Frausto-Vicencio, I., Heerah, S., Meyer, A. G., Parker, H. A., Dubey, M., and Hopkins, F. M.: Ground solar absorption observations of total column CO, CO₂, CH₄, and aerosol optical depth from California's Sequoia Lightning Complex Fire: emission factors and modified combustion efficiency at regional scales, *Atmos. Chem. Phys.*, 23, 4521–4543, <https://doi.org/10.5194/acp-23-4521-2023>, 2023.
- Freitas, S. R., Longo, K. M., and Andreae, M. O.: Impact of including the plume rise of vegetation fires in numerical simulations of associated atmospheric pollutants, *Geophys. Res. Lett.*, 33, L17808, <https://doi.org/10.1029/2006GL026608>, 2006.
- Freitas, S. R., Longo, K. M., Chatfield, R., Latham, D., Silva Dias, M. A. F., Andreae, M. O., Prins, E., Santos, J. C., Gielow, R., and Carvalho Jr., J. A.: Including the sub-grid scale plume rise of vegetation fires in low resolution atmospheric transport models, *Atmos. Chem. Phys.*, 7, 3385–3398, <https://doi.org/10.5194/acp-7-3385-2007>, 2007.
- Freitas, S. R., Longo, K. M., Silva Dias, M. A. F., Chatfield, R., Silva Dias, P., Artaxo, P., Andreae, M. O., Grell, G., Rodrigues, L. F., Fazenda, A., and Panetta, J.: The Coupled Aerosol and Tracer Transport model to the Brazilian developments on the Regional Atmospheric Modeling System (CATT-BRAMS) – Part 1: Model description and evaluation, *Atmos. Chem. Phys.*, 9, 2843–2861, <https://doi.org/10.5194/acp-9-2843-2009>, 2009.
- Freitas, S. R., Longo, K. M., Trentmann, J., and Latham, D.: Technical Note: Sensitivity of 1-D smoke plume rise models to the inclusion of environmental wind drag, *Atmos. Chem. Phys.*, 10, 585–594, <https://doi.org/10.5194/acp-10-585-2010>, 2010.
- Freitas, S. R., Panetta, J., Longo, K. M., Rodrigues, L. F., Moreira, D. S., Rosário, N. E., Silva Dias, P. L., Silva Dias, M. A. F., Souza, E. P., Freitas, E. D., Longo, M., Frassoni, A., Fazenda, A. L., Santos e Silva, C. M., Pavani, C. A. B., Eiras, D., França, D. A., Massaru, D., Silva, F. B., Santos, F. C., Pereira, G., Camponogara, G., Ferrada, G. A., Campos Velho, H. F., Menezes, I., Freire, J. L., Alonso, M. F., Gácita, M. S., Zarzur, M., Fonseca, R. M., Lima, R. S., Siqueira, R. A., Braz, R., Tomita, S., Oliveira, V., and Martins, L. D.: The Brazilian developments on the Regional Atmospheric Modeling System (BRAMS 5.2): an integrated environmental model tuned for tropical areas, *Geosci. Model Dev.*, 10, 189–222, <https://doi.org/10.5194/gmd-10-189-2017>, 2017.
- Gelaro, R., McCarty, W., Suárez, M. J., Todling, R., Molod, A., Takacs, L., Randles, C. A., Darmenov, A., Bosilovich, M. G., Reichle, R., Wargan, K., Coy, L., Cullather, R., Draper, C., Akella, S., Buchard, V., Conaty, A., da Silva, A. M., Gu, W., and Kim, B.: The modern-era retrospective analysis for research and applications, version 2 (MERRA-2), *J. Climate*, 30, 5419–5454, <https://doi.org/10.1175/JCLI-D-16-0758.1>, 2017.
- Gesch, D. B., Verdin, K. L., and Greenlee, S. K.: New land surface digital elevation model covers the earth, *EOS Trans. Am. Geophys. Un.*, 80, 69–70, <https://doi.org/10.1029/99EO00050>, 1999.
- Gevaerd, R. and Freitas, S.: Estimativa operacional da umidade do solo para iniciação de modelos de previsão numérica da atmosfera Parte I: Descrição da metodologia e validação, *Revista Brasileira de Meteorologia*, 21, 59–73, 2006.
- Gili, J., Maín, A., van Drooge, B. L., and Viana, M.: Source-resolved black carbon and PM_{2.5} exposures during wildfires and prescribed burns, *Environ. Pollut.*, 368, 125660, <https://doi.org/10.1016/j.envpol.2025.125660>, 2025.
- Hinds, W. C.: *Aerosol Technology: Properties, Behavior, and Measurement of Airborne Particles*, Wiley-Interscience, New York, 1999.
- Huff, A. K., Kondragunta, S., Zhang, H., Laszlo, I., Zhou, M., Caicedo, V., Delgado, R., and Levy, R.: Tracking smoke from a prescribed fire and its impacts on local air quality using temporally resolved GOES-16 ABI aerosol optical depth (AOD), *J. Atmos. Ocean. Tech.*, 38, 963–976, <https://doi.org/10.1175/JTECH-D-20-0162.1>, 2021.
- ICNF: Portuguese National Forest Inventory 6, Statistics and Cartography, Abundance, State and Condition of National Forest Resources, <http://www.icnf.pt/portal/florestas/ifn> (last access: 1 November 2024), 2015.
- Jaffe, D., Chand, D., Hafner, W., Westerling, A., and Spracklen, D.: Influence of fires on O₃ concentrations in the western U.S., *Environ. Sci. Technol.*, 42, 5885–5891, <https://doi.org/10.1021/es800084k>, 2008.
- Kassianov, E., Flynn, C. J., Barnard, J. C., Berg, L. K., Beus, S. J., Chen, X., China, S., Comstock, J. M., Ermold, B. D., Fakoya, A. A., Kulkarni, G., Lata, N. N., McDowell, N. G., Morris, V. R., Pekour, M. S., Rasmussen, H. J., and Riihimäki, L. D.: Radiative impact of record-breaking wildfires from integrated ground-based data, *Sci. Rep.*, 15, 1–12, <https://doi.org/10.1038/s41598-025-85103-1>, 2025.
- Kirchstetter, T. W. and Novakov, T.: Evidence that the spectral dependence of light absorption by aerosols is affected by organic carbon, *J. Geophys. Res.-Atmos.*, 109, 1–12, <https://doi.org/10.1029/2004JD004999>, 2004.
- Kochanski, A. K., Jenkins, M. A., Yedinak, K., Mandel, J., Beezley, J., and Lamb, B.: Toward an integrated system for fire, smoke and air quality simulations, *Int. J. Wildland Fire*, 25, 534–546, 2015.
- Kochanski, A. K., Herron-Thorpe, F., Mallia, D. V., Mandel, J., and Vaughan, J. K.: Integration of a Coupled Fire-Atmosphere Model Into a Regional Air Quality Forecasting Sys-

- tem for Wildfire Events, *Front. Forest. Glob. Change*, 4, 1–14, <https://doi.org/10.3389/ffgc.2021.728726>, 2021.
- Lack, D. A. and Cappa, C. D.: Impact of brown and clear carbon on light absorption enhancement, single scatter albedo and absorption wavelength dependence of black carbon, *Atmos. Chem. Phys.*, 10, 4207–4220, <https://doi.org/10.5194/acp-10-4207-2010>, 2010.
- Landis, M. S., Pancras, P. J., Graney, J. R., White, E. M., Edger-ton, E. S., Legge, A., and Percy, K. E.: Source apportionment of ambient fine and coarse particulate matter at the Fort McKay community site, in the Athabasca Oil Sands Region, Alberta, Canada, *Sci. Total Environ.*, 584–585, 105–117, <https://doi.org/10.1016/j.scitotenv.2017.01.110>, 2017.
- Lareau, N. P. and Clements, C. B.: Cold Smoke: smoke-induced density currents cause unexpected smoke transport near large wildfires, *Atmos. Chem. Phys.*, 15, 11513–11520, <https://doi.org/10.5194/acp-15-11513-2015>, 2015.
- Longo, K. M., Freitas, S. R., Andreae, M. O., Setzer, A., Prins, E., and Artaxo, P.: The Coupled Aerosol and Tracer Transport model to the Brazilian developments on the Regional Atmospheric Modeling System (CATT-BRAMS) – Part 2: Model sensitivity to the biomass burning inventories, *Atmos. Chem. Phys.*, 10, 5785–5795, <https://doi.org/10.5194/acp-10-5785-2010>, 2010.
- Longo, K. M., Freitas, S. R., Pirre, M., Marécal, V., Rodrigues, L. F., Panetta, J., Alonso, M. F., Rosário, N. E., Moreira, D. S., Gácita, M. S., Arteta, J., Fonseca, R., Stockler, R., Katsurayama, D. M., Fazenda, A., and Bela, M.: The Chemistry CATT-BRAMS model (CCATT-BRAMS 4.5): a regional atmospheric model system for integrated air quality and weather forecasting and research, *Geosci. Model Dev.*, 6, 1389–1405, <https://doi.org/10.5194/gmd-6-1389-2013>, 2013.
- Lopes, D., Menezes, I. C., Reis, J., Coelho, S., Almeida, M., Viegas, D. X., Borrego, C., and Miranda, A. I.: The Short-Term Impacts of the 2017 Portuguese Wildfires on Human Health and Visibility: A Case Study, *Fire*, 7, <https://doi.org/10.3390/fire7100342>, 2024.
- Makar, P. A., Akingunola, A., Chen, J., Pabla, B., Gong, W., Stroud, C., Sioris, C., Anderson, K., Cheung, P., Zhang, J., and Milbrandt, J.: Forest-fire aerosol–weather feedbacks over western North America using a high-resolution, online coupled air-quality model, *Atmos. Chem. Phys.*, 21, 10557–10587, <https://doi.org/10.5194/acp-21-10557-2021>, 2021.
- Mandel, J., Beezley, J. D., Coen, J. L., and Kim, M.: Data assimilation for wildland fires: Ensemble Kalman filters in coupled atmosphere-surface models, *IEEE Contr. Syst. Mag.*, 47–65, <https://doi.org/10.1109/MCS.2009.932224>, 2009.
- Mandel, J., Beezley, J. D., and Kochanski, A. K.: Coupled atmosphere-wildland fire modeling with WRF 3.3 and SFIRE 2011, *Geosci. Model Dev.*, 4, 591–610, <https://doi.org/10.5194/gmd-4-591-2011>, 2011.
- McArthur, A. G.: Weather and grassland fire behaviour, Leaflet, Forestry Timber Bureau Australia, 100, 23 pp., 1966.
- McArthur, A. G.: Fire behaviour in Eucalypt forests, Leaflet, Forestry Timber Bureau Australia, 9th Commonw. For. Conf., New Delhi, 107, 25 pp., 1967.
- Menezes, I. C.: Construção de um Modelo de Interação Atmosfera/fogo Aplicado à Gestão Florestal e Avaliação de Risco de fogos Florestais no Alentejo, Doctoral Thesis from University of Évora, 2015.
- Menezes, I. C., Freitas, S. R., Lima, R. S., Fonseca, R. M., Oliveira, V., Braz, R., Dias, S., Surový, P., and Ribeiro, N. A.: Application of the coupled brams-sfire atmospheric and fire interactions models to the south of Portugal, *Revista Brasileira de Meteorologia*, 36, 423–440, <https://doi.org/10.1590/0102-77863630101>, 2021.
- Menezes, I. C., Lopes, D., Fernandes, A. P., Borrego, C., Viegas, D. X., and Miranda, A. I.: Atmospheric dynamics and fire-induced phenomena: Insights from a comprehensive analysis of the Sertão wildfire event, *Atmos. Res.*, 310, <https://doi.org/10.1016/j.atmosres.2024.107649>, 2024.
- Menezes, I. C., Rodrigues, L. F., Longo, K. M., Ferreira e Freitas, M., Freitas, S. R., and Miranda, A. I.: Brazilian Developments of the Regional Atmospheric Modeling System, Zenodo [data set], <https://doi.org/10.5281/zenodo.19392038>, 2025.
- MERRA-2: Global Modeling and Assimilation Office (GMAO): MERRA-2 inst3_3d_asm_Cp3D: IAU State, Meteorology Instantaneous 3-hourly (p-coord, 0.625x0.5L42), version 5.12.4, Goddard Space Flight Center Distributed Active Archive Center (GSFC DAAC) [data set], <https://doi.org/10.5067/VJAFPL1CSIV>, 2015.
- Miranda, A. I.: An integrated numerical system to estimate air quality effects of forest fires, *Int. J. Wildland Fire*, 13, 217–226, 2004.
- Miranda, A. I., Martins, V., Cascão, P., Amorim, J. H., Valente, J., Tavares, R., Borrego, C., Tchepel, O., Ferreira, A. J., Cordeiro, C. R., Viegas, D. X., Ribeiro, L. M., and Pita, L. P.: Monitoring of firefighters exposure to smoke during fire experiments in Portugal, *Environ. Int.*, 36, 736–745, <https://doi.org/10.1016/j.envint.2010.05.009>, 2010.
- Monks, S. A., Arnold, S. R., and Chipperfield, M. P.: Evidence for El Niño–Southern Oscillation (ENSO) influence on Arctic CO interannual variability through biomass burning emissions, *Geophys. Res. Lett.*, 39, 1–6, <https://doi.org/10.1029/2012GL052512>, 2012.
- Moreira, D. S., Freitas, S. R., Bonatti, J. P., Mercado, L. M., Rosário, N. M. É., Longo, K. M., Miller, J. B., Gloor, M., and Gatti, L. V.: Coupling between the JULES land-surface scheme and the CCATT-BRAMS atmospheric chemistry model (JULES-CCATT-BRAMS1.0): applications to numerical weather forecasting and the CO₂ budget in South America, *Geosci. Model Dev.*, 6, 1243–1259, <https://doi.org/10.5194/gmd-6-1243-2013>, 2013.
- Oliveira, E. R., Silva, B. T., Lopes, D., Corticeiro, S., Alves, F. L., Disperati, L., and Gama, C.: The Detection of Small-Scale Open-Burning Agriculture Fires Through Remote Sensing, *Remote Sens.*, 17, 1–21, <https://doi.org/10.3390/rs17010051>, 2025.
- Osswald, T., Gama, C., Fernandes, A. P., Lopes, D., and Miranda, A. I.: Effects of the wildfires in August 2021 on the air quality of Athens through a numerical simulation, *Int. J. Wildland Fire*, 1633–1645, <https://doi.org/10.1071/WF22148>, 2023.
- Paton-Walsh, C., Jones, N. B., Wilson, S. R., Haverd, V., Meier, A., Griffith, D. W. T., and Rinsland, C. P.: Measurements of trace gas emissions from Australian forest fires and correlations with coincident measurements of aerosol optical depth, *J. Geophys. Res.-Atmos.*, 110, 1–6, <https://doi.org/10.1029/2005JD006202>, 2005.
- Pereira, G.: Estimativa e assimilação das emissões de gases traços e aerossóis de queimadas em modelos de química atmosférica, Tese de Doutorado Instituto Nacional de Pesquisas Espaciais (INPE), 2013.

- Pereira, G., Longo, K. M., Freitas, S. R., Mataveli, G., Oliveira, V. J., Santos, P. R., Rodrigues, L. F., and Cardozo, F. S.: Improving the south America wildfires smoke estimates: Integration of polar-orbiting and geostationary satellite fire products in the Brazilian biomass burning emission model (3BEM), *Atmos. Environ.*, 273, 118954, <https://doi.org/10.1016/j.atmosenv.2022.118954>, 2022.
- Petters, M. D. and Kreidenweis, S. M.: A single parameter representation of hygroscopic growth and cloud condensation nucleus activity, *Atmos. Chem. Phys.*, 7, 1961–1971, <https://doi.org/10.5194/acp-7-1961-2007>, 2007.
- Procopio, A. S., Remer, L. A., Artaxo, P., Kaufman, Y. J., and Holben, B. N.: Modeled spectral optical properties for smoke aerosols in Amazonia, *Geophys. Res. Lett.*, 30, 1–5, <https://doi.org/10.1029/2003GL018063>, 2003.
- Pueschel, R. F., Livingston, J. M., Russell, P. B., Colburn, D. A., Ackerman, T. P., Allen, D. A., and Einfield, W.: Smoke optical depths: Magnitude, variability, and wavelength dependence, *J. Geophys. Res.-Atmos.*, 93, 8388–8402, 1988.
- Radmanović, K., Dukić, I., and Pervan, S.: Specifični toplinski kapacitet drva, *Drvena Industrija*, 65, 151–157, <https://doi.org/10.5552/drind.2014.1333>, 2014.
- Randles, C. A., da Silva, A. M., Buchard, V., Colarco, P. R., Darmenov, A., Govindaraju, R., Smirnov, A., Holben, B., Ferrare, R., Hair, J., Shinozuka, Y., and Flynn, C. J.: The MERRA-2 aerosol reanalysis, 1980 onward. Part I: System description and data assimilation evaluation, *J. Climate*, 30, 6823–6850, <https://doi.org/10.1175/JCLI-D-16-0609.1>, 2017.
- Reid, J. S. and Hobbs, P. V.: Physical and optical properties of young smoke from individual biomass fires in Brazil, *J. Geophys. Res.-Atmos.*, 103, 32013–32030, 1998.
- Reid, J. S., Eck, T. F., Christopher, S. A., Hobbs, P. V., and Holben, B.: Use of the Ångström exponent to estimate the variability of optical and physical properties of aging smoke particles in Brazil, *J. Geophys. Res.-Atmos.*, 104, 27473–27489, <https://doi.org/10.1029/1999JD900833>, 1999.
- Reid, J. S., Eck, T. F., Christopher, S. A., Koppmann, R., Dubovik, O., Eleuterio, D. P., Holben, B. N., Reid, E. A., and Zhang, J.: A review of biomass burning emissions part III: intensive optical properties of biomass burning particles, *Atmos. Chem. Phys.*, 5, 827–849, <https://doi.org/10.5194/acp-5-827-2005>, 2005.
- Relvas, H., Lopes, D., and Armengol, J. M.: Empowering communities: Advancements in air quality monitoring and citizen engagement, *Urban Climate*, 60, <https://doi.org/10.1016/j.uclim.2025.102344>, 2025.
- Reynolds, R. W., Rayner, N. A., Smith, T. M., Stokes, D. C., and Wang, W.: An improved in situ and satellite SST analysis for climate, *J. Climate*, 15, 1609–1625, [https://doi.org/10.1175/1520-0442\(2002\)015<1609:AIISAS>2.0.CO;2](https://doi.org/10.1175/1520-0442(2002)015<1609:AIISAS>2.0.CO;2), 2002.
- Riggan, P. J., Tissell, R. G., Lockwood, R. N., Brass, J. A., Pereira, J. A. R., Miranda, H. S., Miranda, A. C., Campos, T., and Higgins, R.: Remote measurement of energy and carbon flux from wildfires in Brazil, *Ecol. Appl.*, 14, 855–872, <https://doi.org/10.1890/02-5162>, 2004.
- Rothermel, R. C.: A Mathematical Model for Predicting Fire Spread in Wildland Fuels, US Department of Agriculture, Forest Service, Intermountain Research Station, 115, 1972.
- Rothermel, R. C.: Predicting behavior and size of crown fires in the northern Rocky Mountains, USDA Forest Service, Intermountain Research Station, Research Paper, INT-438, 46, 1991.
- Scott, J. H. and Burgan, R. E.: Comprehensive set of standard fire behavior fuel models for use with Rothermel's surface fire spread model, Gen. Tech. Rep. RMRS-GTR-153. Fort Collins, CO: US Department of Agriculture, Forest Service, Rocky Mountain Research Station, 2004.
- Scott, J. H. and Reinhardt, E. D.: Assessing crown fire potential by linking models of surface and crown fire behavior, Forest Service, Rocky Mountain Research Station, September, <https://doi.org/10.2737/RMRS-RP-29>, 2001.
- Seinfeld, J. H. and Pandis, S. N.: Atmospheric chemistry and physics: from air pollution to climate change, John Wiley & Sons, Ltd., 2016.
- Shinozuka, Y. and Redemann, J.: Horizontal variability of aerosol optical depth observed during the ARCTAS airborne experiment, *Atmos. Chem. Phys.*, 11, 8489–8495, <https://doi.org/10.5194/acp-11-8489-2011>, 2011.
- Sørensen, B., Kaas, E., and Korsholm, U. S.: A mass-conserving and multi-tracer efficient transport scheme in the online integrated Enviro-HIRLAM model, *Geosci. Model Dev.*, 6, 1029–1042, <https://doi.org/10.5194/gmd-6-1029-2013>, 2013.
- Tripoli, G. J. and Cotton, W. R.: The Colorado State University three-dimensional cloud/mesoscale model. Part I: General theoretical framework and sensitivity experiments, *Journal de Recherches Atmospheriques*, 16, 185–220, 1982.
- Valente, J., Miranda, A. I., Lopes, A. G., Borrego, C., Viegas, D. X., and Lopes, M.: Local-scale modelling system to simulate smoke dispersion, *Int. J. Wildland Fire*, 16, 196–203, 2007.
- Van Wagner, C. E.: A spread index for crown fires in spring, Canadian Forest Service, Petawawa Nat. For. Inst. Inf. Rep., 1974.
- Van Wagner, C. E.: Conditions for the start and spread of crown fire, *Can. J. Forest Res.*, 7, 23–34, 1977.
- Van Wagner, C. E.: Prediction of crown fire behavior in conifer stands, in: *Proceedings of the 10th Conference on Fire and Forest Meteorology*, edited by: MacIver, D. C., Auld, H., and Whitehead, R., 207–212, 1989.
- Van Wagner, C. E.: Prediction of crown fire behavior in two stands of jack pine, *Can. J. Forest Res.*, 23, 442–449, 1993.
- Yamasoe, M. A., von Randow, C., Manzi, A. O., Schafer, J. S., Eck, T. F., and Holben, B. N.: Effect of smoke and clouds on the transmissivity of photosynthetically active radiation inside the canopy, *Atmos. Chem. Phys.*, 6, 1645–1656, <https://doi.org/10.5194/acp-6-1645-2006>, 2006.
- Ye, X., Arab, P., Ahmadov, R., James, E., Grell, G. A., Pierce, B., Kumar, A., Makar, P., Chen, J., Davignon, D., Carmichael, G. R., Ferrada, G., McQueen, J., Huang, J., Kumar, R., Emmons, L., Herron-Thorpe, F. L., Parrington, M., Engelen, R., Peuch, V.-H., da Silva, A., Soja, A., Gargulinski, E., Wiggins, E., Hair, J. W., Fenn, M., Shingler, T., Kondragunta, S., Lyapustin, A., Wang, Y., Holben, B., Giles, D. M., and Saide, P. E.: Evaluation and intercomparison of wildfire smoke forecasts from multiple modeling systems for the 2019 Williams Flats fire, *Atmos. Chem. Phys.*, 21, 14427–14469, <https://doi.org/10.5194/acp-21-14427-2021>, 2021.

- Yumimoto, K., Tanaka, T. Y., Yoshida, M., Kikuchi, M., Nagao, T. M., Murakami, H., and Maki, T.: Assimilation and forecasting experiment for heavy Siberian wildfire smoke in May 2016 with Himawari-8 aerosol optical thickness, *J. Meteorol. Soc. Jpn. II*, <https://doi.org/10.2151/jmsj.2018-035>, 2018.
- Zerroukat, M. and Shipway, B. J.: ZLF (Zero Lateral Flux): a simple mass conservation method for semi-Lagrangian-based limited-area models, *Q. J. Roy. Meteor. Soc.*, 143, 2578–2584, <https://doi.org/10.1002/qj.3108>, 2017.

Proof only

Remarks from the typesetter

- TS1** Correction 1.
- TS2** Correction 2.
- TS3** Correction 3.
- TS4** Correction 4.
- TS5** Correction 5.
- TS6** Correction 6.
- TS7** Correction 7.
- TS8** Correction 8.
- TS9** Correction 9.
- TS10** Correction 10.
- TS11** Correction 11.
- TS12** Correction 12.
- TS13** Correction 13.
- TS14** Correction 14.
- TS15** Correction 15.
- TS16** Correction 16.
- TS17** Correction 17.
- TS18** Correction 18.
- TS19** Correction 19.
- TS20** Correction 20.
- TS21** Correction 21.
- TS22** Correction 22.
- TS23** Correction 23.